

# UC Irvine

## UC Irvine Electronic Theses and Dissertations

### Title

Experimental and Numerical Studies of Shear Demands of Rock-socketed Drilled Shafts

### Permalink

<https://escholarship.org/uc/item/7cg5c0td>

### Author

Farrag, Rabie

### Publication Date

2021

Peer reviewed|Thesis/dissertation

UNIVERSITY OF CALIFORNIA,  
IRVINE

Experimental and Numerical Studies of Shear Demands of Rock-socketed Drilled Shafts.

DISSERTATION

submitted in partial satisfaction of the requirements  
for the degree of

DOCTOR OF PHILOSOPHY

in civil and environmental engineering

by

Rabie Farrag

Dissertation Committee:  
Associate Professor Anne Lemnitzer, Chair  
Associate Professor Mo Li  
Assistant Professor Mohammad Javad Abdolhosseini Qomi  
Professor Pedro Arduino  
Dr. Benjamin Turner

2021



# **DEDICATION**

To

my wife, parents, and friends

# Table of Contents

Table of Contents .....	ii
List of Figures .....	vii
List of Tables .....	xiv
Acknowledgement .....	xv
Curriculum Vitae .....	xvi
Abstract of the Dissertation .....	xvii
Disclaimer .....	xix
Chapter 1 .....	1
1.1. Introduction.....	1
1.2. Literature Review.....	5
1.3. Research Objectives.....	7
Chapter 2 .....	9
Design of Research Program .....	9
2.1. Analysis Example to support the research design.....	9
2.2. Specimen design for the proposed research.....	12
Chapter 3 .....	17
Experimental Studies .....	17
3.1. Introduction.....	17

3.2.	General specimen layout in the soil pit.....	17
3.3.	Specimen configuration .....	21
3.4.	Material characterization .....	24
3.4.1.	Concrete.....	24
3.4.2.	Soil Material .....	28
3.5.	Specimen Construction .....	36
3.6.	Load Application.....	40
3.6.1.	Testing without fill soil.....	40
3.6.2.	Testing with the fill sand.....	42
3.6.3.	Retesting with the added soil.....	44
3.7.	Visual observations.....	46
Chapter 4.....		48
Instrumentation .....		48
4.1.	Introduction.....	48
4.2.	Internal instrumentation.....	49
4.2.1.	Strain Gages.....	49
4.2.2.	Inclinometer .....	49
4.2.3.	Tetrahedra.....	50
4.3.	External Instrumentation.....	53
4.3.1.	Strain Gages.....	53

4.3.2.	String potentiometers (SP) .....	55
4.3.3.	AC Linear Variable Differential Transducers (LVDTs).....	57
Chapter 5.....		60
Development and Calibration of Novel Sensors.....		60
5.1.	Introduction.....	60
5.2.	Theoretical background.....	62
5.3.	Tetrahedron prototype assembly .....	63
5.4.	Strain transformation .....	66
5.5.	Stress tensor components.....	67
5.6.	Proof of Concept Testing.....	69
5.7.	Load application.....	72
5.8.	Numerical simulation.....	73
5.9.	Tetrahedron performance .....	74
Chapter 6.....		79
Experimental Results and Data Analysis .....		79
6.1.	Shaft Testing without Fill Soil.....	79
6.2.	Shaft Testing with Fill Soil.....	81
6.3.	Post Test Failure Documentation.....	85
6.3.1.	Experimental shear measurements.....	89
6.4.	Results from retest of failed specimens.....	93

6.5. Conclusion .....	98
6.5.1. Testing of the shaft specimens .....	98
6.5.2. Retesting of the shaft specimens .....	98
Chapter 7 .....	100
3D Numerical Analyses of Shear Demand Within the Rock-Socket of Drilled Shafts Subject to Lateral Loading.....	100
7.1. Introduction.....	100
7.2. Numerical simulation.....	100
7.3. Modeling reinforced concrete drilled shafts.....	101
7.4. Modeling the simulated rock.....	107
7.5. Modeling the sand .....	109
7.6. Modeling soil-structure interface.....	110
7.7. Finite element mesh and boundary condition .....	111
7.8. Model calibration and validation.....	113
7.9. Shear stresses and forces extraction from the numerical model.....	123
7.10. Shaft internal shear stresses investigation.....	125
7.10.1. Shaft-rock interface cohesion influence on the shaft response .....	126
7.10.2. Shaft-rock interface friction coefficient influence on the shaft response .....	129
7.10.3. Rock-shaft relative elastic modulus influence on the shaft response .....	131



7.10.4. Experimental shear demands in comparison to numerically generated demands.....	132
7.11. Conclusion.....	135
Chapter 8.....	139
Summary and Conclusions.....	139
8.1. Experimental study findings.....	140
8.1.1. Testing of the shaft specimens.....	140
8.1.2. Retesting of the shaft specimens.....	141
8.2. The implementation of the newly developed sensor summary.....	142
8.3. The numerical study summary.....	142
Chapter 9.....	145
9.1. References.....	145

## List of Figures

Figure 1-1 Model representations of shaft embedment .....	2
Figure 1-2 Air pockets in drilled shafts (Photo copyright: Dan Brown).....	4
Figure 2-1 Moment and shear force profiles in a rock-socketed shaft due to applied lateral loading $F$ at the shaft head.....	10
Figure 2-2 Schematic specimen configuration and variation of transverse reinforcement for all specimens.....	16
Figure 2-3 Load-displacement relationship (right), prediction of shaft moment (middle) and shear (right) due to a lateral load of 58 kN (13 kips) applied at the shaft head.....	16
Figure 3-1 The “soil pit” at the Structural Engineering Testing Hall of the University of California, Irvine .....	19
Figure 3-2 Failure mode for shallow depths (Reese et al., 1974) .....	19
Figure 3-3 Overlapping shear wedges of shafts in the same row (i.e., side to side) (Brown et al., 1988) .....	20
Figure 3-4 Specimen layout in the soil pit and their predicted wedge of failure at shallow depth.....	20
Figure 3-5 Simulated rock-socket blocks configuration .....	23
Figure 3-6 Schematic specimen configuration and variation of transverse reinforcement for all specimens.....	24

Figure 3-7 (a) Instrumented cylinder sample, (b) Capping of concrete cylinders with sulfur mortar, (c) Slump test (d) Concrete cylinder after test.....	25
Figure 3-8 shaft and rock-block concrete strength over time .....	26
Figure 3-9 Compressive stress-strain relationship of shaft concrete at the day of testing ..	27
Figure 3-10 Compressive stress-strain relationship of rock-block concrete at the day of testing.....	27
Figure 3-11. Sieve analysis .....	29
Figure 3-12. Direct shear test data.....	29
Figure 3-13 Relationship between relative density and pluviation drop height .....	30
Figure 3-14 In-situ relative density profile measured during pluviation .....	31
Figure 3-15. Flat dilatometer DMT test results at boreholes A, B, C, D, and E inside the soil pit .....	33
Figure 3-16 CPT test results at boreholes I, II, III, IV, and V inside the soil pit.....	35
Figure 3-17 Sand friction angle correlated to the CPT measured data.....	36
Figure 3-18. Shear wave velocity generated from the Seismic CPT collected data at the northeast of specimen 2 .....	36
Figure 3-19 (a) Instrumented specimens prior to concrete pouring, (b) Shafts braced to the wall prior to concrete pouring, (c) Concrete shafts placed in rock-socket formwork, (d) Specimens with rock-sockets anchored into the floor (e) Geofoam blocks in place .....	38
Figure 3-20 Sand pluviation process.....	39

Figure 3-21 Specimen layout in the soil pit.....	40
Figure 3-22 Shaft head displacement history and loading cycles for Specimen 1 testing without the sand.....	41
Figure 3-23 Completed test setup for specimen 1 testing without the sand.....	41
Figure 3-24 Shaft head displacement history and loading cycles for Specimen 1 .....	43
Figure 3-25 Completed test setup of specimen 1 .....	43
Figure 3-26 Shaft head displacement history and loading cycles for Phase 1 and 2.....	44
Figure 3-27 Schematic specimens' configuration and soil stratigraphy .....	45
Figure 3-28 Completed test setup of Specimen 2 after adding the sand layer and prior to retesting.....	46
Figure 4-1 Instrumentation layout for Specimen 1: (a) External sensors; and (b) Internal sensors (tetrahedral sensors not shown).....	48
Figure 4-2 Inclinator setup .....	50
Figure 4-3 Tetrahedron strain gages carrier device with the six strain gages attached.....	51
Figure 4-4 Tetrahedra layout for Specimen 1.....	52
Figure 4-5 Tetrahedra layout for Specimen 2.....	53
Figure 4-6 Tetrahedra layout for Specimen 3.....	53
Figure 4-7 External strain gages rosettes for Specimen 1 .....	54
Figure 4-8 External strain gages rosettes for Specimen 2 .....	55
Figure 4-9 String pots SP1, SP2, and SP3 layout;(a) schematically; (b) as built .....	57

Figure 4-10 LVDTs locations, (a) schematically; (b) as built.....	59
Figure 5-1 Tetrahedra carriers.....	64
Figure 5-2 Schematic tetrahedron configuration.....	65
Figure 5-3 Tetrahedron strain gages carrier device with the six strain gages attached.....	65
Figure 5-4 Components of stress in three dimensions.....	68
Figure 5-5 Locations of the tetrahedra and moment and shear diagram of the tested beam .....	70
Figure 5-6 (a) affixed tetrahedra inside the beam formwork; (b) concrete pouring; and (c) cured completed beam.....	71
Figure 5-7 Concrete stress-strain relationship of the concrete at the day of beam testing..	72
Figure 5-8 Completed test setup.....	73
Figure 5-9 (a) Model setup; (b) Deformed shape at applied load of 10 kip; (c) Shear stress at an internal point extraction; and (d) Shear stress at selected yz plane.....	74
Figure 5-10 Tetrahedron T3 response history.....	76
Figure 5-11 Measured and numerically generated shear strain, stress, and force histories	77
Figure 5-12 Measured shear versus numerically generated shear comparison at the beam mid-span.....	78
Figure 5-13 Agreement of the numerically generated, and measured shear for loading and unloading cases.....	78
Figure 6-1 Specimen one lateral load test without backfill soil.....	80

Figure 6-2 Comparison of analytically and experimentally derived moment-curvature data of SP 1 in the linear deformation range.....	80
Figure 6-3 Comparison of analytically and experimentally derived load-displacement data of specimen one without backfill soil.....	81
Figure 6-4 Experimental load-displacement relationships with backbone curves .....	83
Figure 6-5 Deformed shape of Specimen 1 (left), Specimen 2 (middle) and Specimen 3 (right) at each applied displacement level (inclinometer readings) .....	84
Figure 6-6 Comparison of analytically and experimentally derived moment-profile of specimen one .....	85
Figure 6-7 Specimen 3 crater formation at different levels of shaft head applied displacement.....	87
Figure 6-8 Summary of major cracks along the shaft depth and around the surface soil at test completion .....	88
Figure 6-9 Crack pattern observation upon excavation of specimens 1 and 3.....	89
Figure 6-10 Global axis versus the tetrahedron local axis.....	90
Figure 6-11 Shear distribution of circular cross section .....	91
Figure 6-12 Tetrahedra located at the maximum shear inside the rock-socket of Specimen 2 measured data.....	93
Figure 6-13 Measured shear profile versus the LPILE generated shear profile inside the rock socket.....	93

Figure 6-14 Load-displacement relationship of specimen 2 and 3 before and after retesting .....	96
Figure 6-15 Specimen 2 deformed shapes before and after adding sand and retesting.....	97
Figure 7-1 Normalized stress-strain curve in compression (Reproduced after Schutz et al. 2011).....	103
Figure 7-2 Concrete model performance versus tested uniaxial concrete cylinders.....	105
Figure 7-3 (a) Local numbering and positioning of nodes (•) and the integration points (x) of a 10-node tetrahedral element; (b) The 12-node interface element; (c) the 3-node beam element .....	112
Figure 7-4 Deformation of the soil layer surrounding the shaft (failure zone) at shaft head maximum displacement of 25.4 cm [10 in] .....	113
Figure 7-5 Layout of the calibration and validation process .....	114
Figure 7-6 Moment – curvature extraction from the numerical model and experimental data.....	117
Figure 7-7 Experimental versus numerical moment – curvature relationship comparisons of Specimen 1 without sand.....	118
Figure 7-8 Load-displacement curve comparisons between the experimental data .....	118
Figure 7-9 Average sand modulus profile correlated to the CPTs profiles versus the linear best fit with depth.....	122
Figure 7-10 Load- displacement relationship at different sand modulus inputs .....	122

Figure 7-11 Calculation of shear force.....	124
Figure 7-12 Distribution of shaft-rock interface stresses .....	124
Figure 7-13 Shear stress distribution of the shaft cross-section inside the socket assuming rigid interface connection versus outside the socket .....	125
Figure 7-14 Moment and shear profile of the shaft at different shaft-rock relative linear moduli, and the corresponding cross-sectional axial deformation .....	131
Figure 7-15 Embedded tetrahedra locations and orientation to the shaft global axis .....	133
Figure 7-16 Experimental shaft cross-sectional shear stresses versus shear stresses found numerically.....	134
Figure 7-17 Moment and shear profile comparisons between experimental, LPILE (p-y method), and numerical simulation of Specimen 1 with and without the sand layer .....	135



## List of Tables

Table 2-1 Predictions of shaft demands using LPLIE, selected reinforcement, and calculated resistances .....	15
Table 3-1 Properties of the sand layer .....	28
Table 4-1 elesco string potentiometers specification model SP1-25 .....	56
Table 4-2 Trans.Tek AC LVDT model 0222-00000 Specifications.....	58
Table 5-1 Sensors angles [°] $\alpha$ , $\beta$ , $\gamma$ with respect to x, y, z axis respectively.....	67
Table 7-1 Embedded beam element versus volume element to simulate the reinforced concrete shaft in PLAXIS .....	102
Table 7-2 Model parameters .....	104
Table 7-3 Proposed values for socket concrete modeling based on the parametric optimization and the stress-strain curve of the tested uniaxial concrete cylinders.....	108
Table 7-4 Field and laboratory testing collected data summery.....	110
Table 7-5 Model inputs for the shaft structural calibration without the sand layer .....	116
Table 7-6 Model staged construction phases sequences.....	121
Table 7-7 Shaft internal shear stresses response to different interface cohesion input .....	128
Table 7-8 Shaft internal shear stresses response to different friction coefficient input.....	130

## **Acknowledgement**

I would like to express my sincere gratitude and appreciation to my supervisor, Professor Anne Lemnitzer, whose expertise was invaluable throughout the course of my studies at University of California Irvine. Her continuous support and insightful feedback have enlightened my critical thinking and brought my research ability to a higher level. It has been an honor to work under her supervision.

I would also like to thank my committee members, Professor Mo Li, Professor Mohamed Qomi, Professor Perdro Arduino, and Dr. Benjamin Turner for their invested time and contribution.

I would particularly like to thank Carter Cox for his help and our endless days and nights at the lab. We indeed have developed a very special friendship that will last longer than a lifetime.

Furthermore, I would like to thank my colleagues, Dr. Lohrasb Keykhosropour, Dr. Sergio Carnalla, Dr. Eric Ahlberg, and Dr. Amr Morsy. Also, I would like to thank the undergraduate research team, Alexandra Wu, Jimmy Fute Chung, Amber Ganapathy, Jordan Taylor Lu, Ani Rita Sarkissian, Justin Whitney Liu, Binyun Gao, Kenny Linares, Bryan Orozco, Loay Bahadur, Christopher Cox, Marcus Juarez, Crystel Maloof, Octavio Martin, Dennis Tuyen Nguyen, and Peng Xia for their collaborative effort during construction and testing.

Finally, I would like to thank my loving wife, Yana, for her patience and support. Most importantly I would like to thank my parents for their continuous and wise guidance and their invaluable moral support.

## Curriculum Vitae

- 2011            B.Sc. in Civil Engineering, Cairo University, Egypt
- 2014            M.Sc. in Civil Engineering, Cairo University, Egypt
- 2014-21        Research and Teaching Assistant, University of California, Irvine, CA
- 2021            Ph.D. in Civil and Environmental Engineering, University of California, Irvine, CA. Dissertation: “Experimental and Numerical Studies of Shear Demands of Rock-socketed Drilled Shafts.”

### PUBLICATIONS

- Farrag, R., Cox, C., Turner, B., and Lemnitzer, A. (2020). “Shear Demands of Rock-Socketed Shafts Subject to Cyclic Lateral Loading”. *Deep Foundations Journal*, Volume 14, Issue 2, DFI Student Paper Award 2020, <https://doi.org/10.37308/DFIJnl.20200526.223>.
- Lemnitzer, A., Farrag, R., and Slowik, V. (2020). „ Experimental derivation of shear stresses in shafts – performance evaluation of a novel instrumentation technique, *Geotechnique Letters*, (*in revision*)
- Lemnitzer, A., Cox, C., Farrag, R., Turner, B. (2019). “Laterally loaded shaft behavior at soil-rock impedance contrast”, XVI Panamerican Conference on Soil Mechanics and geotechnical Engineering, Cancun, Mexico, November 17-20<sup>th</sup>, 2019. (Keynote paper)
- Farrag, R., Turner, B., Cox, C., and Lemnitzer, A. (2021). “Experimental studies of rock socketed shafts with different transverse reinforcement ratios”. International Foundations Congress and Equipment Expo (IFCEE), Dallas, Texas, May 10-14<sup>th</sup>, 2021.
- Farrag, R., Cox, C., and Lemnitzer, A. (2021). “Is this shaft still useful? A case study on laterally loaded large scale shafts after failure”. 20<sup>th</sup> International Conference on Soil Mechanics and Geotechnical Engineering (ICSMGE), Sydney, Australia, November 12-17<sup>th</sup>, 2021. (Paper Submitted)

## **Abstract of the Dissertation**

Experimental and Numerical Studies of Shear Demands of Rock-socketed Drilled Shafts.

by

Rabie Farrag

Doctor of Philosophy in Civil and Environmental Engineering

University of California, Irvine, 2021

Professor Anne Lemnitzer, Chair

The determination of internal shaft reactions is critical to designing and assessing the structural performance of deep foundations. At zones of strong geomaterial stiffness contrast, Winkler-spring-type analyses predict pronounced changes in the shear and moment profiles for laterally-loaded foundation elements. In particular, the sudden deamplification of internal moments when transitioning from a soft to stiff layer is accompanied by amplification of shaft shear. This “shear spike” results in dense transverse reinforcement designs and poses severe constructability challenges due to reinforcement congestion, increasing the risk of defective concrete on the outside of the cage. This study presents an experimental research program of three large-scale, instrumented, drilled shafts placed in simulated rock. Each shaft had a different transverse reinforcement design, intended to bound the amplitude of the predicted amplified shear demand. State-of-the-art instrumentation and monitoring was performed to capture the behavior of the test shafts during loading. As part of the instrumentation program, a new sensor was constructed that

aimed at measuring concrete internal strains in three dimensions. The instrumentation is novel in that it represents the first attempt to determine experimentally the 3D strain field through embedded sensors with immediate application to a broad array of shaft foundation engineering problems. The three large-scale pile specimens were tested to structural failure and subsequently retested after additional soil was placed to raise the fill height above the rock socket. The originally predicted shear failure did not occur; rather, a flexure-triggered failure through the formation of a plastic hinge above the rock-socket was observed. Test results suggested that the shafts experienced a flexure-dominated failure irrespective of the transverse reinforcement detailing. Retesting with 64% more soil compared to the original soil thickness provided an additional 80% capacity compared to  $P_{ult}$  of the damaged specimen.

Results obtained from the experimental study were used to calibrate a three-dimensional finite element model in PLAXIS 3D to better understand the load-transfer mechanism within the rock socket. Good agreement was observed between the numerically generated results and experimental data. A selected set of parametric studies was performed to investigate the effects of the interface input parameters (i.e., cohesion, and friction angle) and the influence of shaft/rock relative stiffness on the shaft shear response.

## Disclaimer

The contents of this PhD thesis have been in part or in full, published or are currently in review with the following Journals and Conferences:

Farrag, R., Cox, C., Turner, B., and Lemnitzer, A. (2020). "Shear Demands of Rock-Socketed Shafts Subject to Cyclic Lateral Loading". *Deep Foundations Journal*, Volume 14, Issue 2, DFI Student Paper Award 2020, <https://doi.org/10.37308/DFIJnl.20200526.223>.

Lemnitzer, A., Farrag, R., and Slowik, V. (2020). „ Experimental derivation of shear stresses in shafts – performance evaluation of a novel instrumentation technique, *Geotechnique Letters*, (in revision)

Lemnitzer, A., Cox, C., Farrag, R., Turner, B. (2019). "Laterally loaded shaft behavior at soil-rock impedance contrast", XVI Panamerican Conference on Soil Mechanics and geotechnical Engineering, Cancun, Mexico, November 17-20<sup>th</sup>, 2019. (Keynote paper)

Farrag, R., Turner, B., Cox, C., and Lemnitzer, A. (2021). "Experimental studies of rock socketed shafts with different transverse reinforcement ratios". International Foundations Congress and Equipment Expo (IFCEE), Dallas, Texas, May 10-14<sup>th</sup>, 2021.

Farrag, R., Cox, C., and Lemnitzer, A. (2021). "Is this shaft still useful? A case study on laterally loaded large scale shafts after failure". 20<sup>th</sup> International Conference on Soil Mechanics and Geotechnical Engineering (ICSMGE), Sydney, Australia, November 12-17<sup>th</sup>, 2021. (Paper submitted)

Lemnitzer, A., Farrag, R., Turner, B. (2019) "Lateral Loading of Rock-Socketed Piles" <http://dfi.dcatalog.com/v/September-October-2019> (Magazine featured article)

Lemnitzer, A., and Farrag, R. (202x). "Large-Scale lateral load testing of rock-socketed piles in sand", *Earthquake Spectra* (in submission)

# Chapter 1

## 1.1. Introduction

Deep foundation systems are an integral albeit costly component of our urban living and infrastructure system. In areas where soft soils dominate subsurface conditions, shafts are extensively used to transfer vertical and lateral superstructure loading originating from tall buildings, bridges, or offshore structures into stronger ground. Tip embedment into a strong geomaterial layer, such as a drilled shaft rock socket, offers an attractive solution for achieving maximum tip resistance and improving the load transfer behavior of the foundation element.

Good understanding has been gained and published for axially loaded shafts; however, uncertainties exist for laterally loaded shafts in rock sockets when designed using Winkler based analysis models. Currently no experimental data exist to verify the shaft behavior and the development of internal moment and shear forces of rock-socketed shafts under lateral loading. Simultaneously only very few numerical studies exist that investigate this particular problem. Figure 1-1a shows a simple shaft with a free rotational boundary condition at the shaft head and a fixed boundary condition provided by the rock embedment at the shaft toe. Given that rock commonly contains a weathered zone at the rock-soil interface, the analytical representation of the structural support provided by the embedment varies widely among foundation engineers. The depth at which full rotational and frictional resistance can be provided is often estimated, particularly when project budgets do not allow for extensive rock drilling, sampling and laboratory testing. Figures 1-1b-d display structural support

options to model the rock socketed shaft in analytical or numerical approaches. Figure 1-1b assumes complete structural fixity in displacement and rotation starting at the soil-rock interface over the entire embedment depth. This assumption creates a significant impedance contrast between the two foundation materials which influences the shaft response at the respective shaft depth. Figure 1-1c depicts the opposite extreme, assigning pinned supports that enable a lateral displacement restraint but do not provide rotational resistance or fixity. A more advanced model is displayed in Figure 1-1d, in which soil-shaft interaction and rock-shaft interaction is considered and represented through a series of non-linear springs corresponding to the respective material properties.

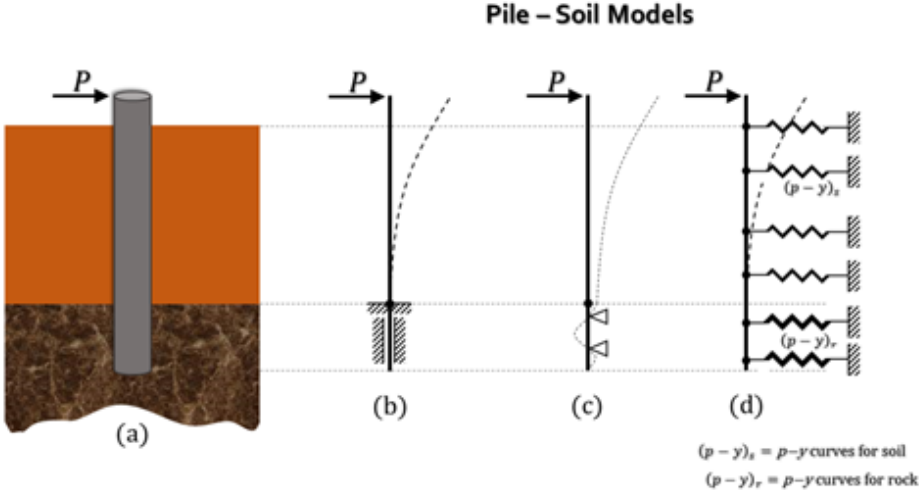


Figure 1-1 Model representations of shaft embedment

Previous studies (e.g., Turner, 2006) have shown that the  $p-y$  type analyses of laterally loaded shafts embedded in rock yield unexpectedly high values of shear forces, which translate into unreasonably high structural design demands. A supporting example is provided in chapter 2. Given the stiffness contrast between the rock layer and a soft overburden soil, a shaft subject to lateral forces and moments at the shaft head, develops



shear forces in the vicinity of the rock –soil interface with much higher magnitudes than the applied lateral load at the shaft head. This phenomenon stems from the back-calculation of shear forces along the shaft through differentiation of the moment profile and the change in curvatures along the shaft depth following the traditional 4<sup>th</sup> order differential beam equation.

National design recommendations such as the Caltrans “Bridge Design Practice” manual published in February 2015, recognize the uncertainty [Section 16.4.4 : “*When CIDH shafts tipped in rock are analyzed for lateral loads, the p-y method reports shear demand forces that exceed the seismic overstrength shear,  $V_o$  calculated demand in the column. **The abrupt change to high-stiffness p-y springs may amplify shear force to more than  $5V_o$  within the rock socket.**”..... “*However, there is ongoing debate over whether the design force is “real” and whether the discretization of distributed soil reaction to nodal springs is appropriate at the rock interface.*”] (Caltrans, 2015). To be conservative, Caltrans recommends the enlargement of the shaft cross-section or the provision of additional transverse reinforcement to resist the amplified shear demand. The high demands yield expensive designs that carry a multitude of intrinsic construction issues as listed in Table 1. Whether it is the increase of shaft diameters (which consequently increases the foundation cost in terms of construction and materials) or if it's the increase in shear reinforcement (which in turn reduces the workability, with the extreme case of air pockets forming in the rebar cage due to lack of proper placement and vibration space inside the shaft (see Figure 1-2)), the uncertainty of the existence and magnitude of the shear force amplification at the rock-soil interface is in desperate need of experimental clarification.*

**Table 1. Solutions and difficulties associated with increased shear demands**

Options to satisfy increased shear demand	Drawbacks
Increasing the shaft diameter (increase of concrete shearing area)	<ul style="list-style-type: none"> <li>▪ high construction cost,</li> <li>▪ larger diameter drill equipment,</li> <li>▪ material costs</li> </ul>
Utilization of high strength concrete	<ul style="list-style-type: none"> <li>▪ material cost concrete increases</li> </ul>
Increasing the amount of transverse reinforcement	<ul style="list-style-type: none"> <li>▪ material cost steel</li> <li>▪ reduction of spacing to accommodate increased amounts of steel will cause construction difficulties, e.g. concrete/air voids or pockets (see Figure 2).</li> </ul>
Increasing the diameter of transverse reinforcement	<ul style="list-style-type: none"> <li>▪ large rebar sizes are not fabricate-able as spirals, individual hoops needed → installation and labor intense.</li> <li>▪ higher steel material costs.</li> </ul>



Figure 1-2 Air pockets in drilled shafts (Photo copyright: Dan Brown)

Much controversy exists in the geotechnical community whether the large resulting shear demands are real, or if high shear forces are an artifact of the analysis method.

On many projects, the structural designer will proportion the transverse reinforcement to satisfy the amplified shear demand, often without adequate consideration of the constructability concerns that this may cause. In a prescriptive design setting, an unintended

consequence of this approach is that the designer may be exposed to liability for resulting defects if the contractor claims that the congested cage design is what led to defective concrete, not their own means and methods. In contrast, some designers attempt to mitigate this issue through various approaches that fall into the category of “engineering judgment”. For example, by artificially redistributing the shear profile over a larger depth interval while maintaining the same total magnitude of shear resistance (i.e., area under the shear curve), effectively disregarding the predicted local shear spike. A related approach is to simulate a gradual increase in stiffness of the rock layer with depth, thereby reducing the magnitude of stiffness contrast at the soil-rock boundary and consequently forcing the moment to distribute over a larger depth interval, resulting in reduced shear amplification. In cases where there is a gradual increase in rock stiffness, for example because of intense weathering at the rock surface that gradually diminishes with depth, this approach is appropriate because it reflects the real ground conditions. But to artificially simulate the rock in this manner if such a transition is not supported by rock core data cannot be scientifically justified. While the author is not aware of any instances in which these approaches have been associated with a foundation failure, it has not yet been demonstrated that the underlying concepts can be supported by valid, rigorous analyses.

## **1.2. Literature Review**

The validation of shear amplification (or the lack thereof) predicted with the  $p$ - $y$  method against instrumented load tests or validated numerical models is scarce in existing literature. However, the correct evaluation of shear demands at soil-rock interfaces is vital since the shear demand may govern the drilled shaft structural design. Current literature provides

limited amounts of well-documented and sufficiently instrumented experimental research data on rock-socketed shafts under lateral loading. Full scale lateral load testing of rock-socketed shafts dates to pioneering tests in the 1970s and 1980s (e.g., Horvath and Kenney (1979), Frantzen and Stratton (1987), Carter and Kulhawy (1988)) and was expanded in the 1990s and 2000s. However, most of the documented experiments predominantly focused on the geotechnical aspects of rock-socketed shafts and the derivation of  $p$ - $y$  relationships for rock materials. For instance, Rojas-Gonzales *et al.*, 1993, Yang and Liang, 2006; Guo and Lehane, 2016 studied the overall lateral load behavior. Brown and Shie, 1990; Carter and Kulhawy, 1992; Dykeman and Valsangkar, 1996; Leung and Chow, 2000; Ashour and Norris, 2001; Ramakrishna *et al.*, 2004, Yuan *et al.*, 2014 conducted analytical and numerical studies of shaft performance in various rock-types, embedment lengths, and investigated the suitability of modeling techniques. Others have focused on the derivation of soil resistance formulations for shafts in rock (i.e.,  $p$ - $y$  curves) (e.g., Frantzen and Stratton, 1987; Reese, 1997; Gabr *et al.*, 2002; Liang *et al.*, 2009; Kim *et al.*, 2015; Koshravifar and Zafir, 2019). Less attention has been directed towards the response behavior of foundation systems in soil strata with strong stiffness contrasts such as present near the interface between stiff rock and soft soils.

Arduino *et al.* (2018) is the only study attending to this matter by numerically investigating the interface behavior at the soil-rock boundary through FEM studies in OPENSEES. Arduino *et al.*'s comparison between results from  $p$ - $y$  based models and 3DFEM shows 3DFEM produces less magnitude of the shear force and bending moment demands in the shaft. In addition, the research team observed numerically that friction along the socket shaft, as well as the length of the rock socket shaft in comparison to the overlaying soil tends to reduce

shear demands. Arduino *et al.* also notices that results have a strong numerical variation and that the level of magnification depends more on the type of rock model used (Reese (1997) vs. Liang et al. (2009), J2 (or Von Mises) vs. Drucker- Prager (1952)) than on the type of analysis conducted (BNWF vs. 3D). Unfortunately, no comparison with any experimental results was performed within the framework of Arduino *et al.*'s study as no suitable data was available to the authors of that study.

### **1.3. Research Objectives**

To alleviate the lack of experimental data and to provide empirical results to support the industry-wide hypothesis that highly amplified rock-socket shear does not develop in the large magnitude predicted analytically, a large-scale test program was developed to study the lateral load behavior of rock-socketed reinforced concrete shafts under lateral loading. The experimental studies will provide new data for deep foundations with geo-structurally complex boundary conditions, (i.e., various levels of fixity at the shaft base) through coordinated experimental and numerical studies on large-scale test specimens. This will remedy the current shortage of experimental data and develop a complete set of pilot interaction data which, to date, have not been measured experimentally in a similar manner. Another key objective of this study is to advance the development of new instrumentation concepts to measure strains within the shaft and around the circumference at the shaft surface. The new instrumentation, an intelligent tetrahedron, is constructed with a stiffness adaptable skeleton and is composed of four equilateral triangles that serve as a 3D gauge carrier. The proposed instrumentation is groundbreaking in that it will be the first attempt to measure 3D strains experimentally in foundation engineering using embedded sensor

technology. Successful completion will eliminate uncertainties, by facilitating direct measurements superior to inverse data analyses.

Upon completing the proposed experimental studies, this research seeks to develop validated nonlinear models to verify the overall response behavior and parametrically study the demand and response relationship by strategically varying critical model input parameters to provide a complete physical understanding of deep foundation behavior and a more accurate (and safer while more economical) foundation design framework for a broad range of applications.

Finally, findings of this research are critical for engineering design and construction as high magnitude shear amplifications can result in overly bulky transverse reinforcement designs that pose serious constructability challenges due to reinforcement congestion, increasing the risk of defective concrete on the outside of the cage. The broader application of these findings is applicable to any soil stratigraphy with strong stiffness contrasts as modeling such would yield similar results when using  $p$ - $y$  type soil resistance formulations.

## Chapter 2

### Design of Research Program

#### 2.1. Analysis Example to support the research design

Prior to proposing a future study to gain insight into the controversy of shear force amplification, a short analytical supporting study was performed to demonstrate the shear spike effect near the rock-soil interface for laterally loaded shafts. In this example, a reinforced concrete shaft with circular cross-section ( $d=0.91\text{m}$  [3ft]), a compressive strength of  $f_c=27.6\text{MPa}$  [4ksi] and an E-modulus of  $E = 248211\text{MPa}$  [36000ksi] [is installed in a soil profile consisting of  $12.2\text{m}$  [40ft] of soft clay underlain by  $7.6\text{m}$  [25ft] of weak rock (see Figure 2-1a). The total shaft length  $L$  is  $18.3\text{m}$  [60ft] and the shaft head is modeled as a free head boundary condition (i.e., no rotation restraint). The soft clay has a unit weight  $\gamma$  of  $640.7\text{ kg/m}^3 - 688.8\text{ kg/m}^3$  [40 pcf - 43 pcf], and undrained shear strength  $c_u$  of  $2.4\text{ kPa} - 57.5\text{ kPa}$  [50 psf - 1200 psf], varying linearly from the top to the bottom of the layer, respectively.

The rock layer extends  $1.5\text{m}$  [5ft] below the shaft toe. The rock unit weight is taken as  $\gamma = 1233.4\text{ kg/m}^3$  [77 pcf], and the uniaxial compressive strength varies between  $4137\text{kPa} - 5516\text{kPa}$  [600 psi -800 psi]. The initial modulus of rock is varied between  $689 \cdot 10^6\text{ kPa}$  [ $100 \cdot 10^6\text{ psi}$ ] at the top of the rock layer to  $3447 \cdot 10^6\text{ kPa}$  [ $500 \cdot 10^6\text{ psi}$ ] at the bottom of the layer. The rock RQD is taken as 80%. Both layers are modeled with traditional  $p$ - $y$  springs for the respective layer. Studies were executed using the commercially available program LPILE.

Lateral loading is applied at the shaft head with magnitudes of  $F=222, 445, 667\text{ kN}$  [50, 100, and 150 kips]. The shaft's moment and shear force profile are shown in Figure 2-1. Figure 2-

1c demonstrates the amplification of shear forces between one and two shaft diameters below the soil-rock interface when reaching larger lateral load levels  $F$  at the shaft head. A head load of  $F = 445 \text{ kN}$  [100 kips] generates an internal shear force of  $667 \text{ kN}$  [150 kips] within the rock socket (blue line), indicating a 50% increase in shear demand for the concrete shaft. A lateral force of  $667 \text{ kN}$  [150 kips] applied at the shaft head, is amplified in the analysis to yield an internal shear force of  $1410 \text{ kN}$  [317 kips] (red line), which indicates an **increase of 211%**. According to the Caltrans bridge design manual, this magnification can be up to 500 % ( $5V_0$ ).

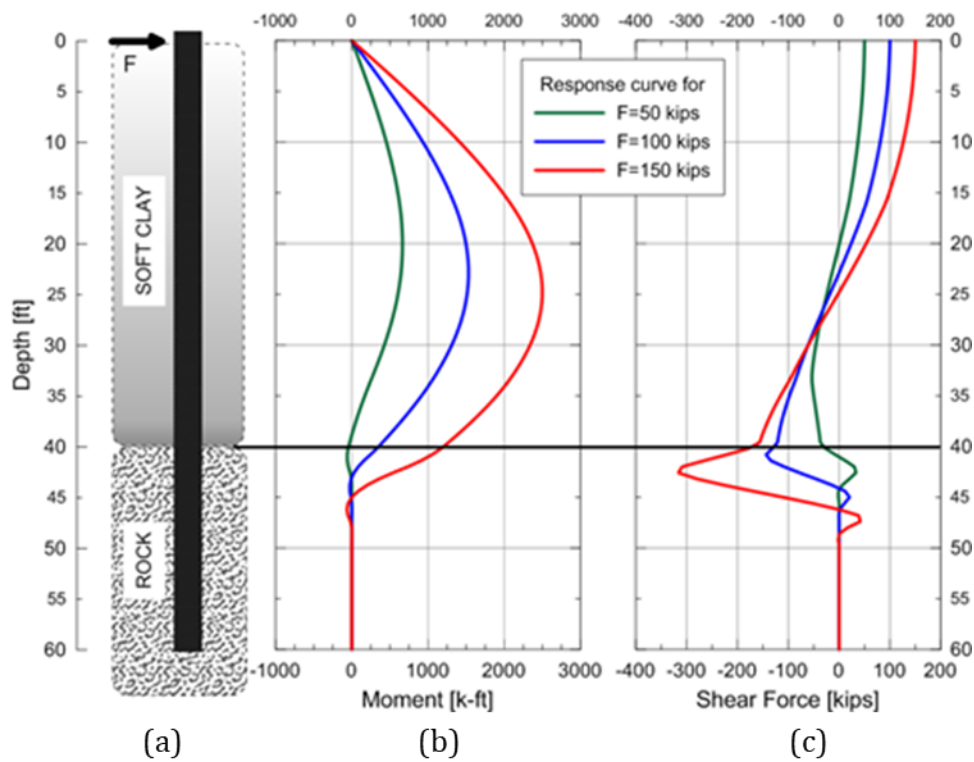


Figure 2-1 Moment and shear force profiles in a rock-socketed shaft due to applied lateral loading  $F$  at the shaft head



The transverse reinforcement design for the two extreme cases explained above is conducted as follows: The maximum shaft shear will first be assumed to equal the applied lateral force  $F$  at the shaft head (i.e. no shear amplification). A second design scenario is carried out in which the transverse reinforcement is designed for the amplified shear demand observed in the rock-socketed portion of the shaft (Figure 2-1c). The min transverse reinforcement requirements per ACI 318-14 Section 10.6.2.2. and per AASHTO Section 5.8.2.5 are  $0.77 \text{ cm}^2$  [ $0.12 \text{ in}^2$ ] and  $0.96 \text{ cm}^2$  [ $0.15 \text{ in}^2$ ], respectively, and are satisfied for either design scenario below.

The total shear capacity  $V_u$  must be provided through:  $V_u = \phi(V_c + V_s) = 667 \text{ kN}$  [150kips] /1410 kN [317kips] (red line).

The available concrete capacity  $V_c$  is:  $V_c = 2\sqrt{f'_c}bd = 627 \text{ kN}$  [141 kips].

Shear reinforcement is therefore needed for a shear force  $V_s = \frac{V_u}{\phi} - V_c$

**Required spacing,  $s$ , for Scenario 1:  $F=667 \text{ kN}$  [150 kips],  $V_u = 667 \text{ kN}$  [150 kips], # 4 spirals, 7.6 cm [3"] concrete cover**

$$s = \frac{A_v f_y d}{\frac{V_u}{\phi} - V_c} = \frac{0.4 \text{ in}^2 * 60 \text{ ksi} * 30"}{\frac{150 \text{ kips}}{0.75} - 141 \text{ kips}} = 31 \text{ cm} [12.2"]$$

This spacing allows for easy construction and can be reduced further if better confinement is desired.

**Required spacing,  $s$ , for Scenario 2:  $F=667 \text{ kN}$  [150 kips],  $V_u = 1410 \text{ kN}$  [317 kips], #4 spirals, 7.6 cm [3"] concrete cover**

$$s = \frac{A_v f_y d}{\frac{V_u}{\phi} - V_c} = \frac{0.4 \text{ inch}^2 * 60 \text{ ksi} * 30"}{\frac{317 \text{ kips}}{0.75} - 141 \text{ kips}} = 6.5 \text{ cm} [2.55"]$$

The amplified shear force of 1410 kN [317 kips] requires a spiral/hoop spacing of 6.5 cm [2.55"], which is nearly impossible to accommodate in the field and falls short of the min recommended transverse spacing of 10 cm [4"]. An increase in reinforcement diameter to

#5 spirals would lighten the min required spacing to 9.9 cm [3.9"], but still falls short the ACI recommendations of  $s \geq 10$  cm [4"]. Spiral reinforcement using #6 bars is not constructible in the rebar plant, leaving the designer with the option of either requesting individual hoop installation with adequate transverse steel diameters, or increasing the shaft diameter to increase the shear capacity of the concrete area. Either solution however trails labor intensity or elevated material costs to satisfy the amplified shear demand. If expected loads are even larger than the assumed lateral loading (i.e. in seismic regions), the estimated shear spike could approach a magnification factor of 5, as indicated in the Caltrans bridge manual, leaving the design engineer with no other solution than significantly increasing the shaft diameter and transverse reinforcement diameter simultaneously.

## **2.2. Specimen design for the proposed research**

The specimen design and configuration were determined partly on the basis of analytical pre-test predictions using the commercially available software platform LPILE (Ensoft, 2018). Geomaterial layer properties and geometry were specified such that the stiffness contrast creates a significant shear amplification relative to the applied lateral load at the shaft head as predicted using the  $p$ - $y$  method. Initial estimates of the sand properties were based on information provided by the material supplier. Concrete strengths were taken as 28-day design compressive strengths. Within LPILE, the rock layer was analytically represented using  $p$ - $y$  springs for weak rock (Reese 1997) and the sand was modeled using the O'Neill and Murchison (1983)  $p$ - $y$  model. The Reese  $p$ - $y$  curves were adopted here to be consistent with the state-of-practice as per Turner (2006) these curves are mostly used by practitioners for rock. The input parameters for the simulated rock layer consisted of initial

rock mass modulus, uniaxial compressive strength, strain factor, and rock quality designation (RQD), taken as 32,888 MPa [4770 ksi] , 48 MPa [7 ksi], 0.0005, and 100%, respectively. Model parameters for the sand layer consisted of effective unit weight and friction angle taken as 14.5kN/m<sup>3</sup> [92 pcf] and 35 degrees. The planned tests were simulated up to a maximum applied lateral load at the shaft head of 58 kN 13 kips [13 kips], where the lateral load is applied approximately 175 cm [6 ft] above the sand surface to amplify flexural demands and maximize the lateral demands reaching the rock socket. For the final selected stratigraphic configuration, the amplified shear calculated with LPLIE is 471 kN [106 kips] , which corresponds to a shear amplification ratio of 8.1 (i.e., the applied shear normalized by calculated amplified shear).

The three 45.7 cm [18.0-in] diameter shaft specimens were designed as follows: Specimen 1 was designed to resist maximum values of shear and moment predicted using LPILE, which required significant shear reinforcement – a No. 4 spiral at 11.4 cm [4.5-in] pitch ( $\rho_s = 1.27\%$ ). Specimen 2 ( $\rho_s = 0.96\%$ ) was designed to only satisfy the code minimum volumetric transverse reinforcement requirements (ACI 318, 2019, AASHTO, 2017) associated with the applied lateral load, and did not provide adequate calculated nominal shear strength to resist the predicted amplified shear demand. Specimen 3 only contained a minimal amount of transverse reinforcement ( $\rho_s = 0.26\%$ ), which provided adequate calculated nominal shear resistance to exceed the applied lateral load 58 kN [13 kips] but did not satisfy code minimum requirements for transverse reinforcement spacing and did not provide adequate calculated nominal shear strength to resist the predicted amplified shear demand. Figure 2-2 shows schematically the specimens' configuration and variation of transverse reinforcement. If the actual shear amplification at the soil-rock interface is consistent with

the value predicted using the  $p$ - $y$  method, and the nominal shear strength of the structural sections are reasonably close to the calculated values, Specimens 2 and 3 would be expected to fail due to insufficient shear strength in the upper rock socket region where the analytically predicted shear spike occurs. A structural design summary for all specimens is presented in Table 1.

Figure 2-3 shows the predicted shaft moment and shear profiles for the three shaft specimens at the point when the calculated maximum moment reaches the nominal flexural strength of the section. (It is noted that nominal flexural strength is not assumed to depend on the variable transverse reinforcement details of each specimen for this purpose.) Figure 2-3 (right) illustrates shear amplification at the soil-rock boundary. The significant predicted shear amplification ratio was intentionally created to exaggerate the analytically predicted shear spike effect, although this amount of shear amplification is not uncommon in practice for real project geometries and stratigraphies. Furthermore, it is hypothesized that structural shear failure would not occur despite the significant discrepancy between calculated nominal shear strength and amplified shear demand, and that the shafts would form a flexural mechanism when loaded to failure; the significant shear amplification was intended to test this hypothesis. Likewise, the thickness of the sand layer was minimized, and it was placed in a relatively loose condition to maximum lateral demands reaching the socket while still representing the commonly encountered soil-over-rock stratigraphy. The dashed lines in Figure 2-3 indicate the nominal shear strength ( $V_n$ ) of each specimen. These shear strengths (also shown in Table 2-1) are predicted to be reached when the shafts experience lateral shaft head loads of 13kN, 11.6kN, and 7.8 kN [58kips, 52kips, and 35 kips

] for Specimens 1, 2, and 3, respectively (presented as “predicted shaft head load at failure” in Table 2-1).

Table 2-1 Predictions of shaft demands using LPLIE, selected reinforcement, and calculated resistances

	Specimen 1 (SP1)	Specimen 2 (SP2)	Specimen 3 (SP3)
Designed to satisfy:	Amplified shear	Code minimum	Applied shear
Max applied load @ shaft head, kN [kips]	58 [13]	58 [13]	58 [13]
Max. flexure demands $M_u$ , kN-m [kip-ft]	149 [110]	149 [110]	149 [110]
Nominal moment strength $M_n$ , kN-m [kip-ft]	150 [111]	150 [111]	150 [111]
Maximum shear demand $V_u$ , kN [kips]	471 [106]	471 [106]	471 [106]
Concrete shear strength $V_c$ , kN [kips]	155 [34.8]	155 [34.8]	155 [34.8]
Steel shear strength (required) $V_s$ , kN [kips]	320 [72]	Not needed/Use min.	Not needed
Selected transverse reinforcement, bar # @ pitch, mm [in]	Spiral #4 @ 114 [4.5]	Spiral #4 @ 152 [6]	Ties #3 @ 305[12]
Transverse reinf. volumetric ratio, $\rho_s$ [%]	1.27%	0.95%	0.26%
Nominal shear strength $V_n$ , kN [kips]	477 [107]	396 [89]	222 [50]
Predicted failure mode based on $p$ - $y$ analysis	Flexural failure	Shear failure	Shear failure
Predicted shaft head load at failure based on $p$ - $y$ analysis, kN [kip]	58 [13]	52 [11.6]	35 [7.8]

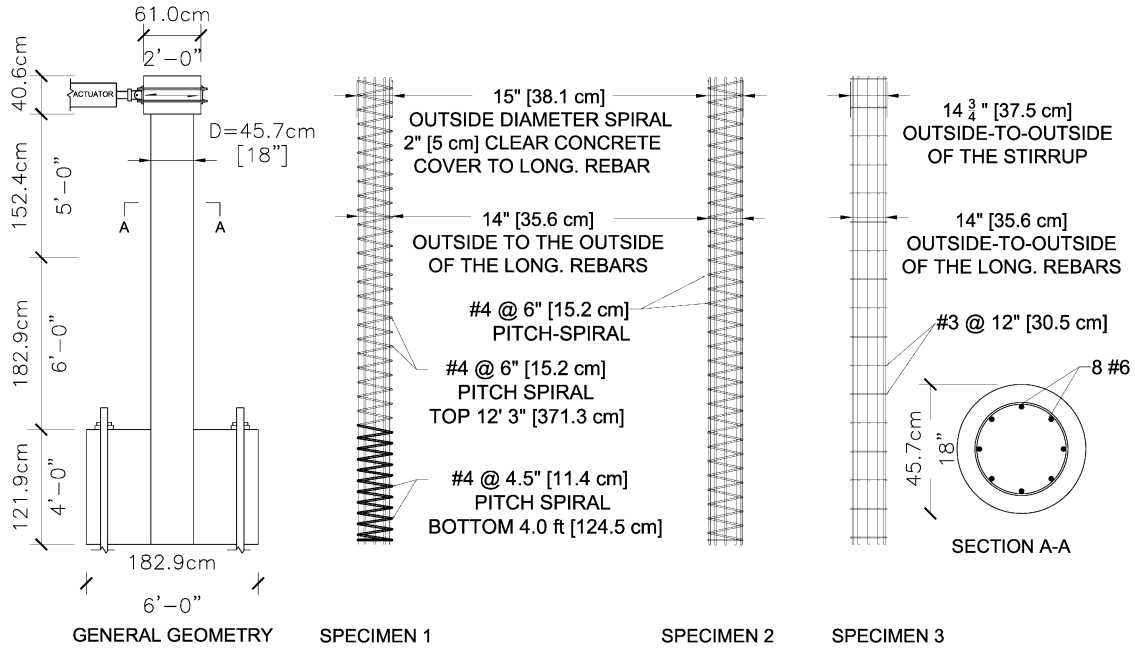


Figure 2-2 Schematic specimen configuration and variation of transverse reinforcement for all specimens

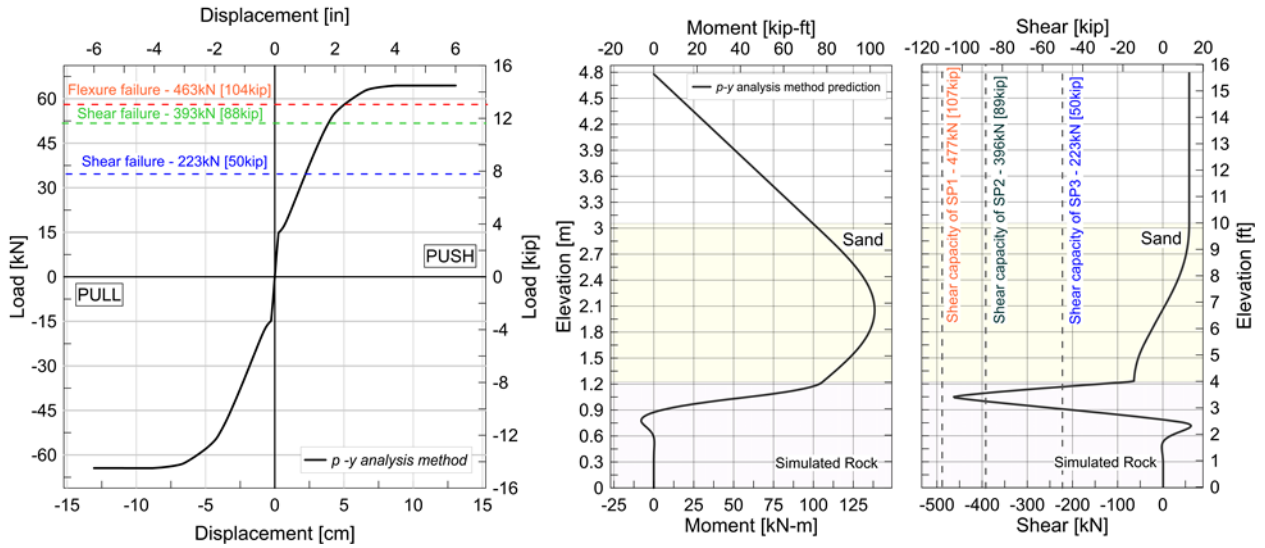


Figure 2-3 Load-displacement relationship (left), prediction of shaft moment (middle) and shear (right) due to a lateral load of 58 kN (13 kips) applied at the shaft head.

## Chapter 3

### Experimental Studies

#### 3.1. Introduction

The experimental studies were executed in the “soil pit” at the Structural Engineering Testing Hall of the University of California, Irvine. Three test shafts were embedded in a constructed sand-over-rock stratigraphy and subjected to reverse cyclic lateral loading until complete structural failure was reached. The experimentally simulated “rock” was replicated through cast-in-place concrete blocks that were post-tensioned to the base of the test pit to provide translational and rotational restraint. This restraint was necessary to simulate a continuous mass of strong nondeformable rock. The specimen design and configurations were determined based on the analytical pre-test predictions discussed in Chapter 2.

#### 3.2. General specimen layout in the soil pit

The experimental test bed was a large rectangular soil pit with dimensions of 9.1m [30ft] in length, 6.1m [20ft] in width, and 4.26m [14 ft] in depth as shown in Figure 3-1. Potential wall-boundary and pile-soil-pile interaction effects were limited through carefully selected specimen alignment following Brown et al. (1988) research on pile-to-pile shadowing. In addition, a wedge type failure (at shallow depths) following Reese et al (1974) (Figure 3-2) was assumed and taken into consideration when spacing both rows of pile specimens. The shear wedge model geometry shown in Figure 3-3 is a function in the shaft diameter  $D$  and the soil internal friction angle  $\phi$ . Factors  $\alpha$  and  $\beta$  are measured in degrees and can be estimated by the following relations:  $\alpha = \phi/2$ , and  $\beta = 45 + \phi/2$  (Reese 1974). Angle  $\beta$  is estimated according to Rankine's theory, which is valid if the shaft surface is assumed

smooth. Side-to-side interaction can be avoided or minimized by minimizing the overlapping of the shear wedges between the shafts within the soil pit (see Figure 3-2). The fill sand used for this experimental program was chosen based upon a parametric study of different types of fill sand available locally. Sand optimizations and characteristics have been established and discussed in detail in Section 3-4. The sand friction angle  $\phi$ , obtained via direct shear testing, was 38.4 degrees. Using the Reese (1974) correlations shown above,  $\alpha$  and  $\beta$  factors were found to be 19.2 degrees and 64.2 degrees respectively. According to Gwizdala and Jacobsen (1992), a lower bound solution assumes  $\alpha = 0$ , whereas an upper bound solution assumes  $\alpha = \phi$ . Therefore, when using the value of  $\alpha$  as given in the Reese (1974) equation, the developed wedge would fall between a lower bound and an upper bound solution for a smooth shaft. An angle  $\alpha = 30$  degrees was conservatively chosen as a reference to lay out the shafts in the soil pit in order to achieve the minimum possible overlapping of the shear wedges as shown in Figure 3-4.

Three shaft specimens were part of this research study, named Specimen 1 (SP1), Specimen 2 (SP2), and specimen 3 (SP3), as well as an additional four shafts that were part of another ongoing experimental research project under the supervision of the same PI as this study.



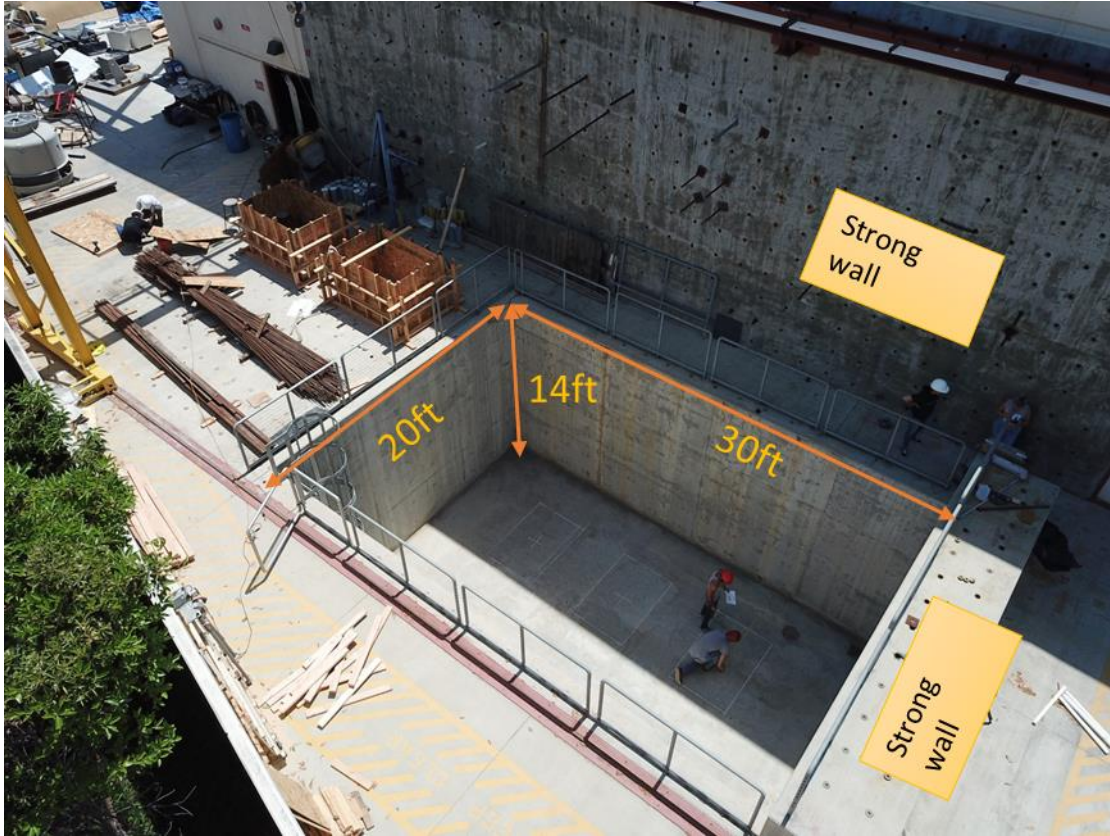


Figure 3-1 The “soil pit” at the Structural Engineering Testing Hall of the University of California, Irvine

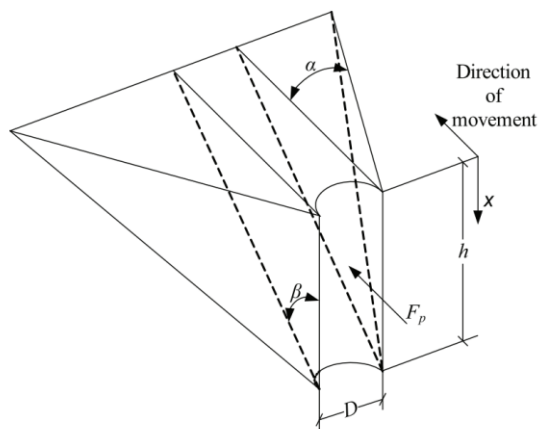


Figure 3-2 Failure mode for shallow depths (Reese et al., 1974)

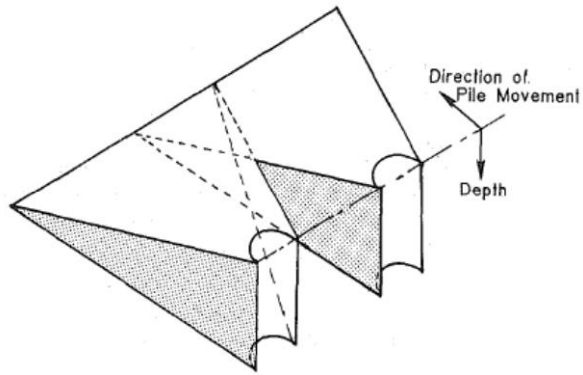


Figure 3-3 Overlapping shear wedges of shafts in the same row (i.e., side to side) (Brown et al., 1988)

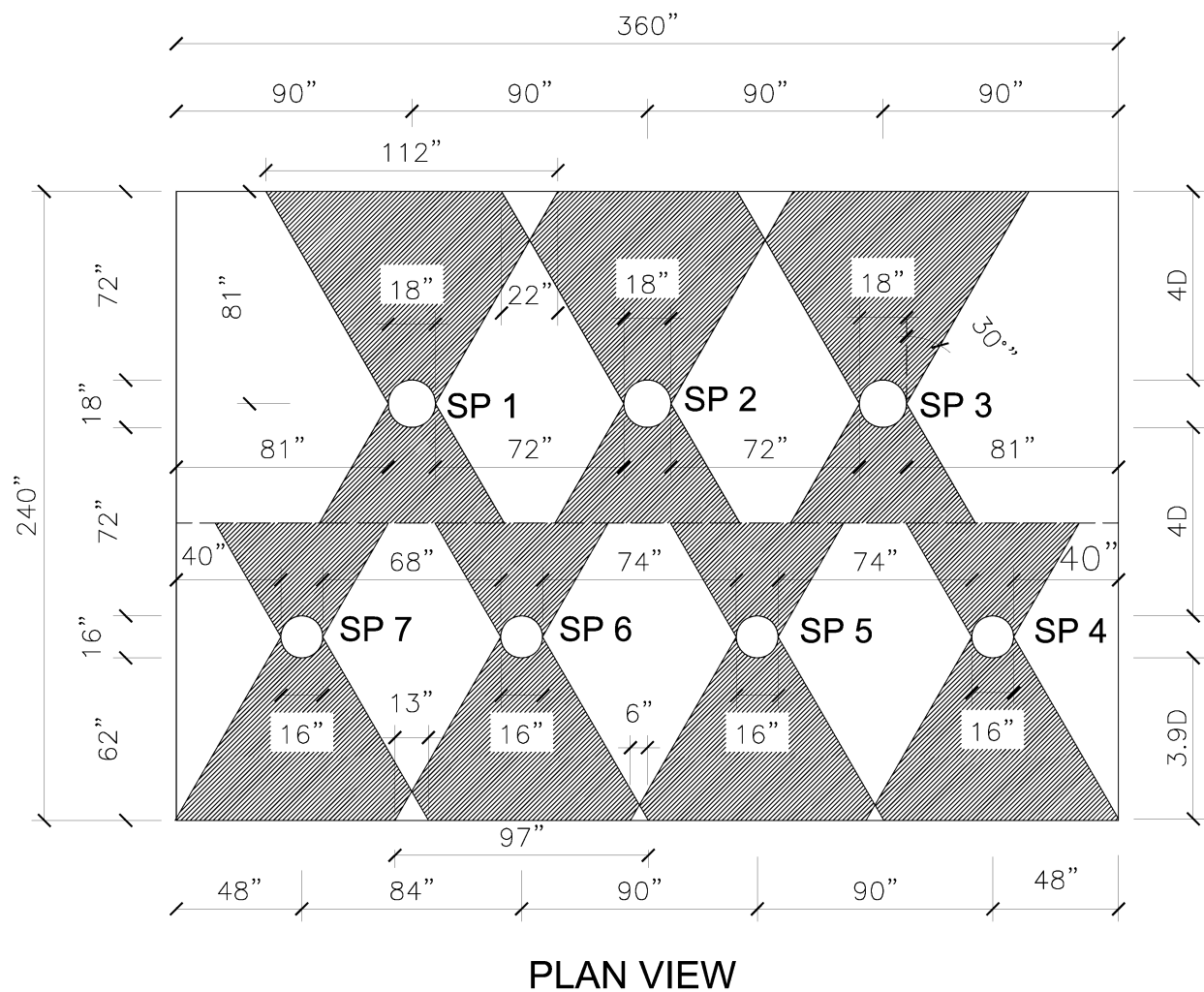


Figure 3-4 Specimen layout in the soil pit and their predicted wedge of failure at shallow depth

### 3.3. Specimen configuration

The reinforced concrete shafts were 4.57 m [15.0 ft] in length and 0.46 m [18.0 in] in diameter, the shafts were embedded in 1.20 m [4.0 ft] of “rock”, simulated experimentally by high strength concrete ( $f'_c = 48.3$  MPa [7 ksi]). The concrete blocks (*i.e.*, the “rock sockets”) had dimensions of 1.83 m [6.0 ft] in length, 1.22 m [4.0 ft] in width, and 1.22 m [4.0 ft] in height. The blocks were secured to the reinforced concrete floor of the testing facility using pre-drilled, epoxy-grouted, high strength steel anchors as shown in Figure 3-5. The shafts extended a total of 3.35 m [11.0 ft] above the rock. A rectangular “shaft cap” with cross-sectional dimensions of 0.61 x 0.61 m [24 x 24 in] and a height of 0.41m [16 in] was constructed at each shaft head and used for actuator attachment and application of lateral loading. The geometry and reinforcement configurations of the three specimens are illustrated in Figure 3-6. Longitudinal reinforcement consisted of eight No. 6 Grade 60 A706 steel bars ( $A_{s, total} = 22.71$  cm<sup>2</sup> [3.52 in<sup>2</sup>]), which corresponds to a longitudinal reinforcement ratio of  $\rho = 1.41\%$ . Longitudinal rebars were equally spaced around the circumference of the shaft with a clear concrete cover of 5 cm [2.0 in]. Specimens’ 1 and 2 transverse reinforcement consisted of #4 spirals, and Specimen 3 transverse reinforcement consisted of #3 ties as indicated in Figure 3. The transverse reinforcement of Specimen 1 (#4 spirals) was spaced at a pitch of 114 mm [4.5 in] in the rock socket (*i.e.*, approximately up to an elevation of 1.2 m [4.0 ft] from the shaft tip), and spaced at a pitch of 152 mm [6.0 in] along the remaining shaft height. The closer spiral pitch at the bottom of the shaft is the only configuration that satisfies the amplified shear demand within the rock socket as predicted by the p-y analysis shown in Table 1 and Figure 2. Specimen 2 was reinforced with #4 transverse spirals at a pitch of 152 mm [6.0 in] along the entire shaft length. The transverse

reinforcement consisted of #3 ties spaced at 305 mm [12.0 in] across the entire shaft length and provided just enough structural stability to hold the longitudinal rebar cage together. Specimen's 3 transverse reinforcement ratio is only 0.26%. Its contribution to the overall shear strength  $V_n$  is minimal and analytically not needed, as the concrete cross-section provides adequate shear resistance  $V_c$  to satisfy the applied lateral load demands at the shaft head (i.e., shear amplification at the rock socket is ignored and the internal shear force is assumed to distribute uniformly as the case for cantilever beams.) This scenario implies that the assumed shear magnitude is equal to the applied lateral force at the shaft head. To reiterate, this configuration is not permitted by any structural design codes and was intended for experimental demonstration purposes only.

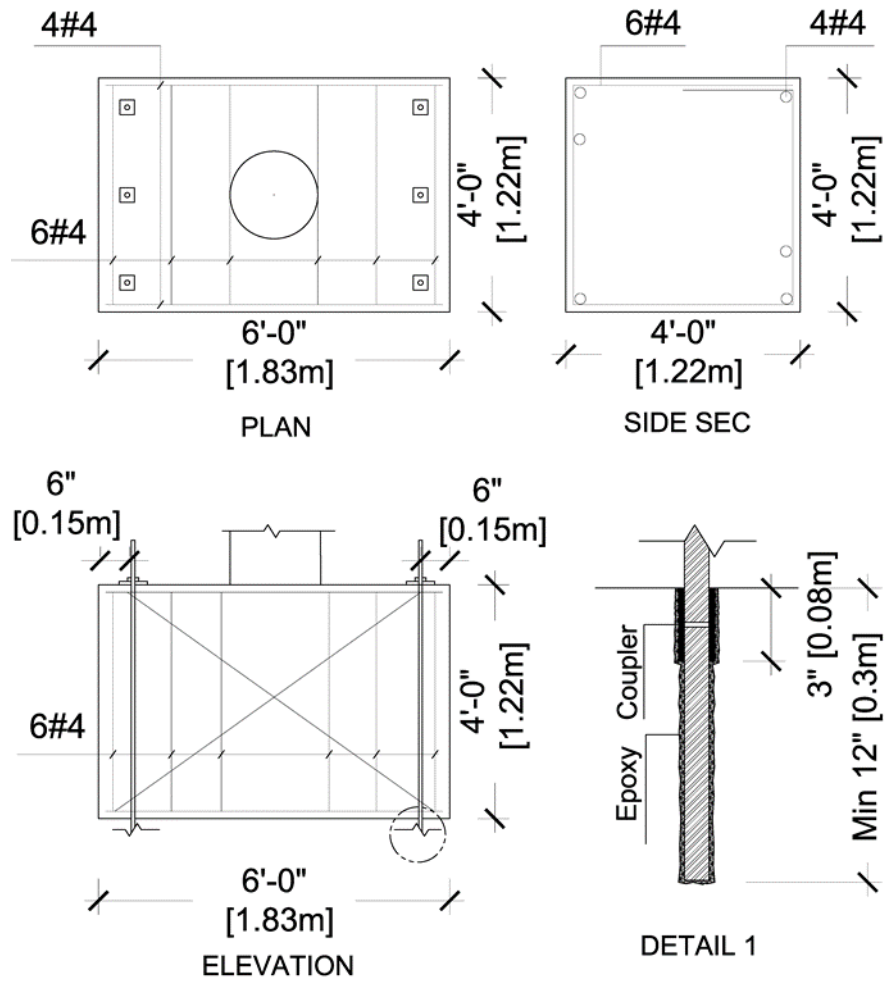


Figure 3-5 Simulated rock-socket blocks configuration

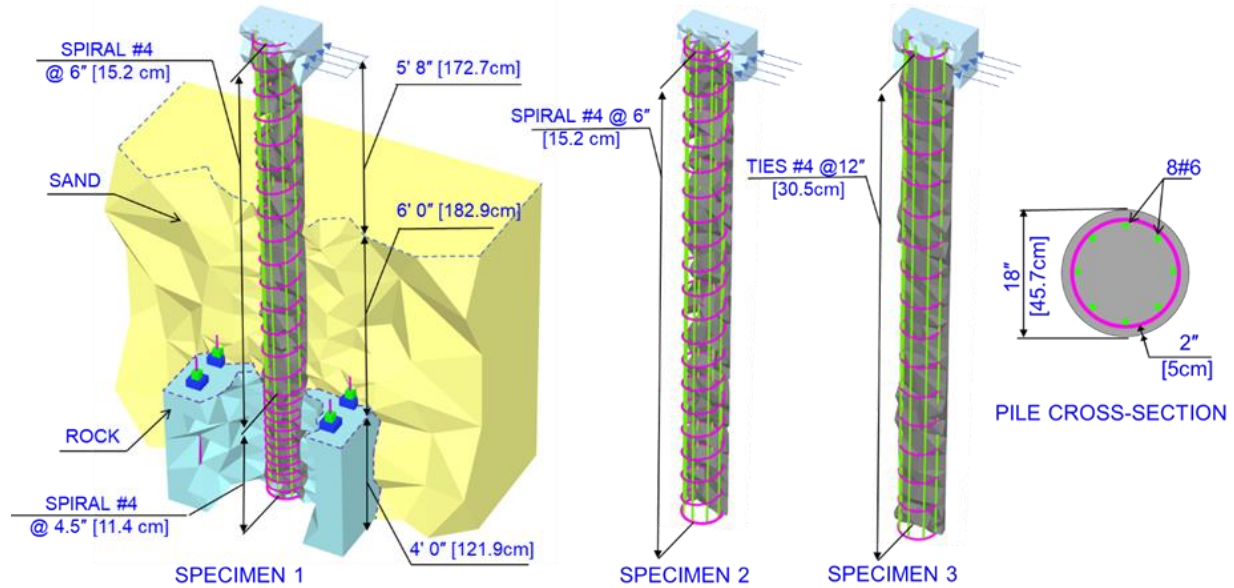


Figure 3-6 Schematic specimen configuration and variation of transverse reinforcement for all specimens

### 3.4. Material characterization

#### 3.4.1. Concrete

Concrete for the shaft specimens and simulated rock blocks was delivered to the UCI experimental facility from a local plant in Orange County. The concrete aggregate consisted of pea gravel with a maximum size of 1 cm [3/8 in]. Slump values measured at the time of placement were 7.6 cm [3 in] for the rock-block concrete and 9.5 cm [3.75 in] for the shaft concrete. Concrete cylinders with dimensions of 15 cm [6 in] in diameter by 30.5 cm [12 in] in height were taken on site per ASTM C39. Cylinder's testing was conducted according to ASTM C39 at 7, 21, 28 days, as well as the day of the shaft testing. The test cylinders were instrumented axially and horizontally with LVDTs as shown in Figure 3-7 to capture the axial deformation and transverse dilation of the specimen in accordance with ASTM C469. Figure 3-8 shows the shaft and rock-block concrete strength over time. The rock-block concrete mix had a 28-day design compressive strength of 34.5 MPa [5 ksi], and an average cylinder break

strength of 48.3 MPa [7 ksi] on the day of testing. Shaft Specimens 1, 2, and 3 had a 28-day design compressive strength of 27.58 N/mm<sup>2</sup> [4 ksi], and cylinder break strengths of 40.7, 39.3, and 39.3 MPa [5.9, 5.7, and 5.7 ksi] on the day of testing, respectively. A summary of the average cylinder test results is shown in Figures 3-9 and 3-10. Young's modulus values measured from the concrete cylinders were  $E_{\text{conc,shaft}} = 26.6 \text{ GPa}$  [3856 ksi] and  $E_{\text{conc,rock}} = 25.5 \text{ GPa}$  [3695 ksi]. The ratio of rock to soil stiffness ( $E_{\text{rock}}/E_{\text{soil}}$ ) is about 15,000.

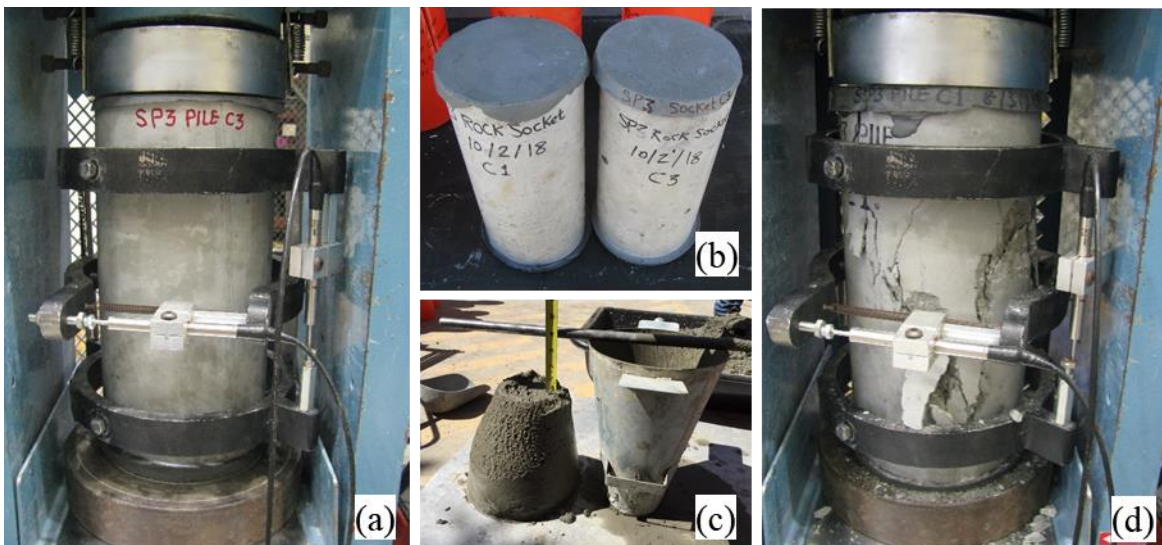


Figure 3-7 (a) Instrumented cylinder sample, (b) Capping of concrete cylinders with sulfur mortar, (c) Slump test (d) Concrete cylinder after test

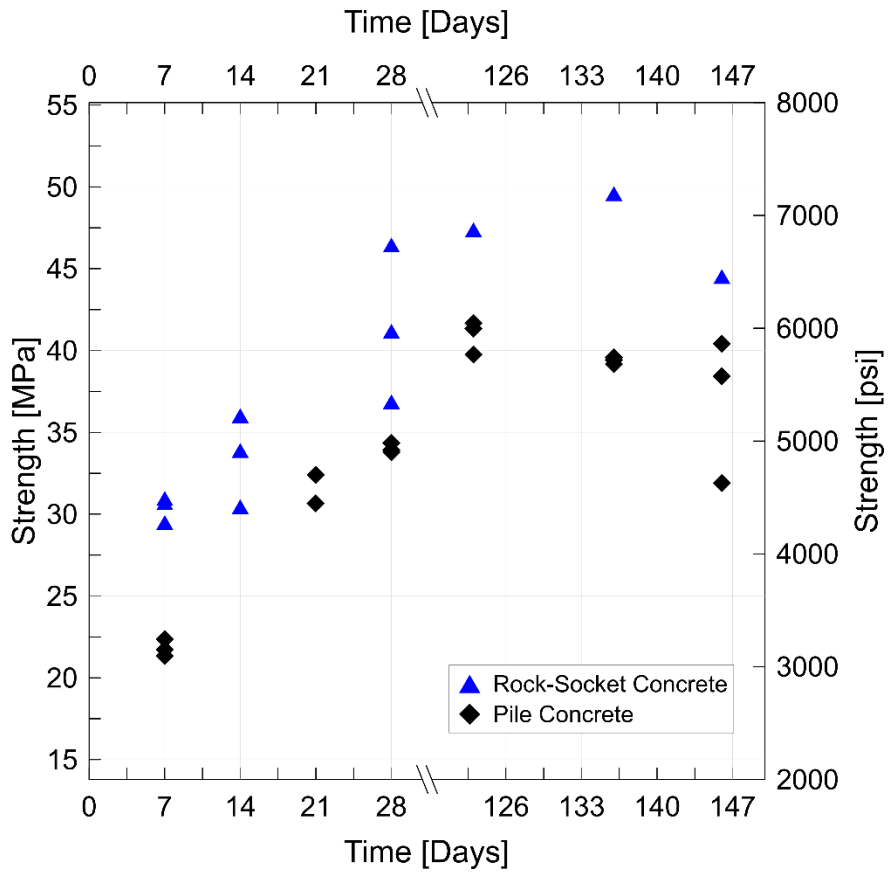


Figure 3-8 shaft and rock-block concrete strength over time



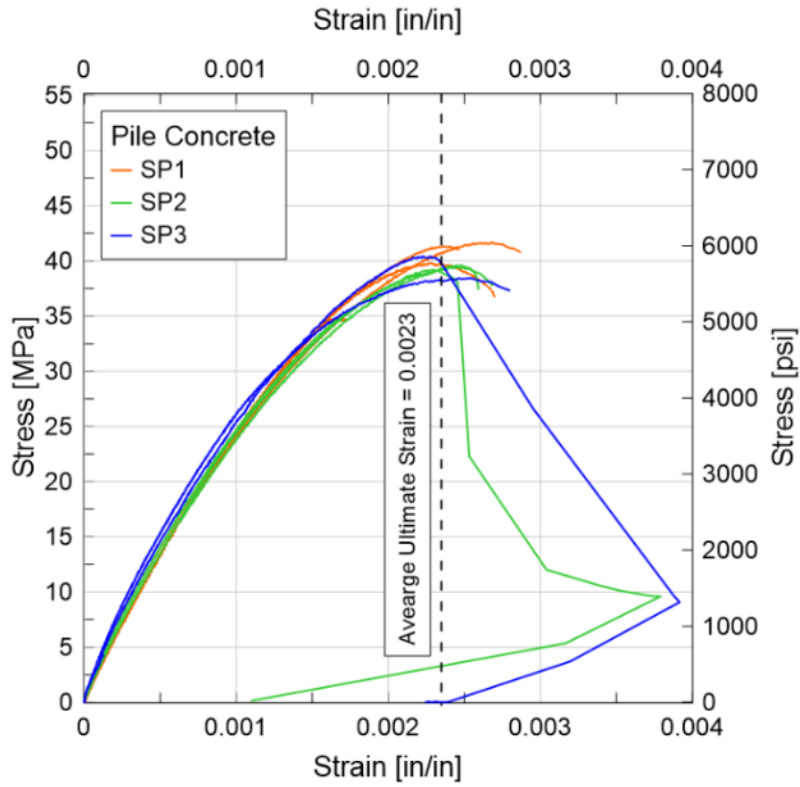


Figure 3-9 Compressive stress-strain relationship of shaft concrete at the day of testing

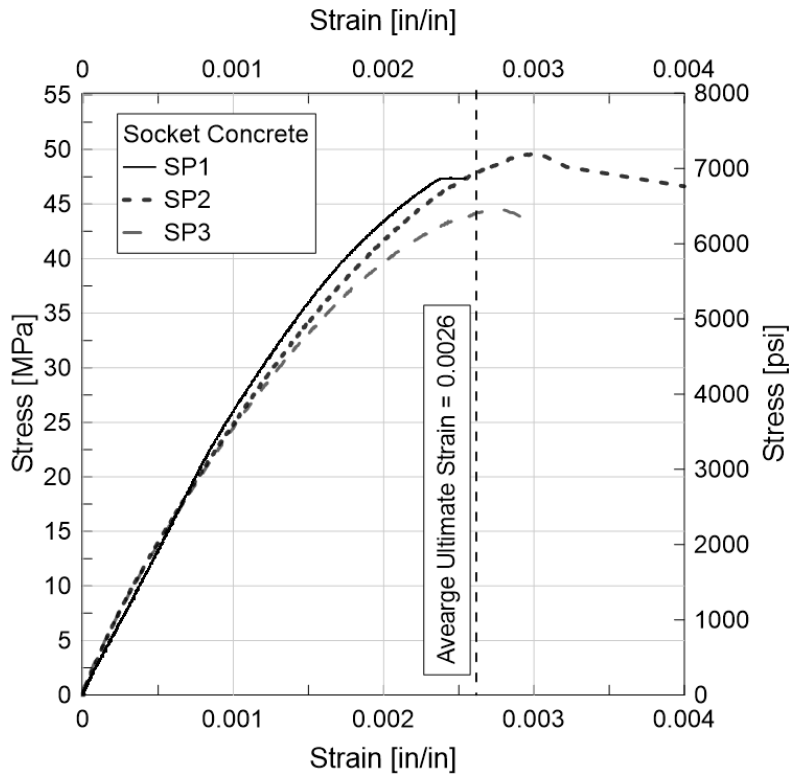


Figure 3-10 Compressive stress-strain relationship of rock-block concrete at the day of testing

### 3.4.2. Soil Material

The sand material was selected based on the following criteria: (1) ease of installation and pluviation into the soil pit, (2) local availability, (3) properties being representative of typical loose in-situ granular soil, and (4) costs associated with material and transportation to UCI. Prior to selecting the final soil material, about a dozen fill materials from different suppliers were investigated in the laboratory to identify their mechanical and index properties. The final choice consisted of a fill sand with a friction angle of 34.8 deg determined through direct shear testing per ASTM D3080, and a maximum dry unit weight of 21 kN/m<sup>3</sup> [134 pcf] determined via modified Proctor compaction testing (ASTM D1557). The sand was pluviated from a minimum height of 3.66 m [12 ft] to reach a target average relative density of 20%. Pluviation was accomplished using a self-designed and calibrated sieve system attached at the bottom of a concrete hopper. The calibration process included the iteration of optimum freefall heights as well as the assembly of multiple sieve openings until the desired relative density was reached as shown in Figure 3-13. The low in-situ relative density of 20% provided a strong stiffness contrast between the soil and simulated rock. The average in-situ moisture content of the soil was 6%. Figure 3-14 shows the in-situ relative density profile.

Table 3-1 Properties of the sand layer

Percentile sand grain diameters $D_{10}, D_{30}, D_{60}$ [mm]	0.33, 0.7, 1.51
Uniformity coefficient, $C_u$	4.52
Coefficient of curvature, $C_c$	0.98
Particle density, $G_s$	2.69
Maximum dry unit weight, $\gamma_{d_{max}}$ [pcf]	134
Minimum dry unit weight, $\gamma_{d_{min}}$ [pcf]	80
Minimum Void Ratio, $e_{min}$	0.25
Maximum Void Ratio, $e_{max}$	1.1
Friction angle, $\phi$ [°]	38.4°
Cohesion, $c$ [psi]	0.0

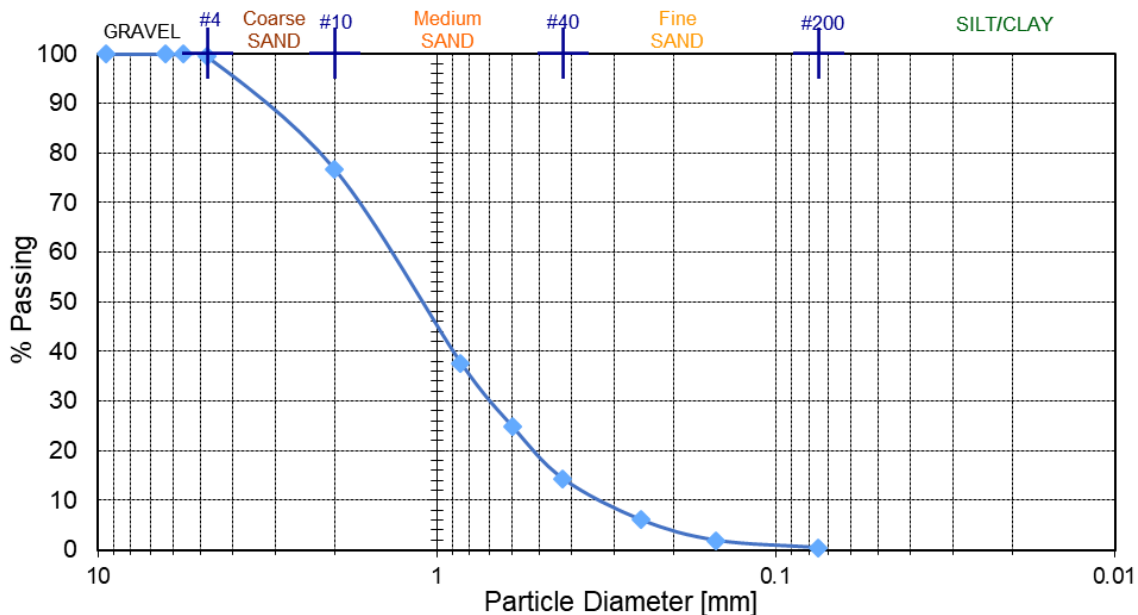


Figure 3-11. Sieve analysis

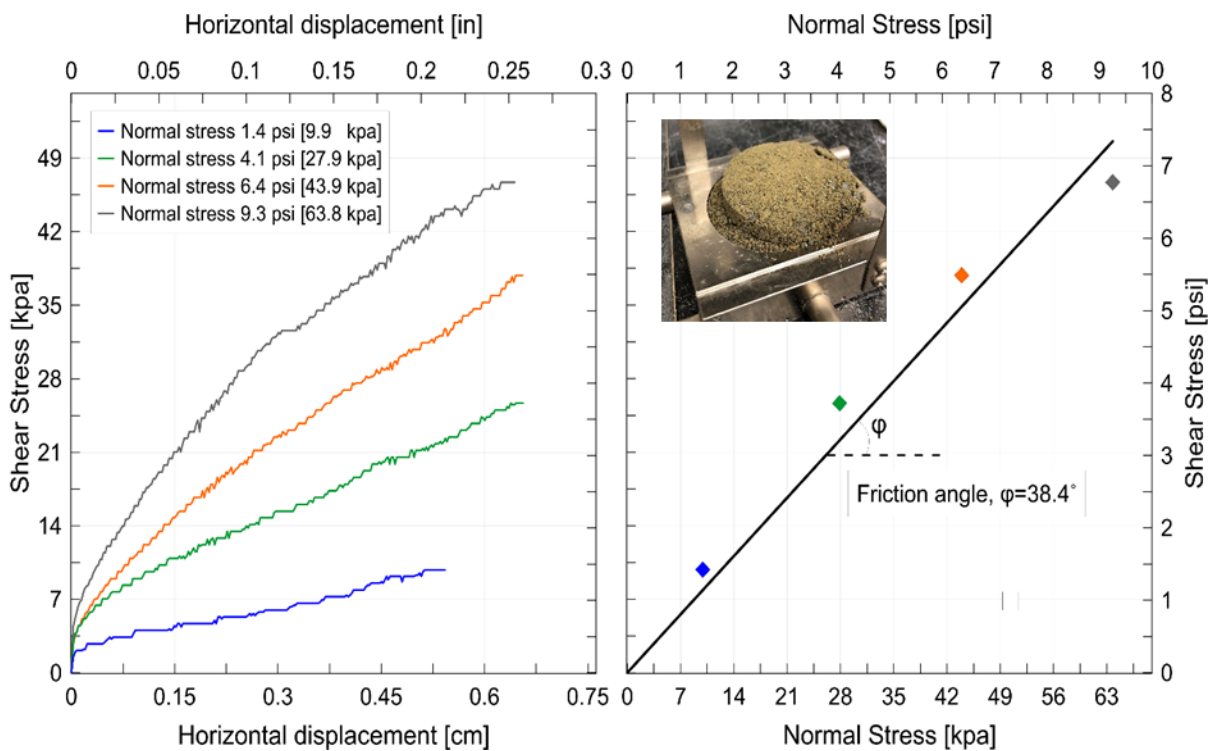


Figure 3-12. Direct shear test data

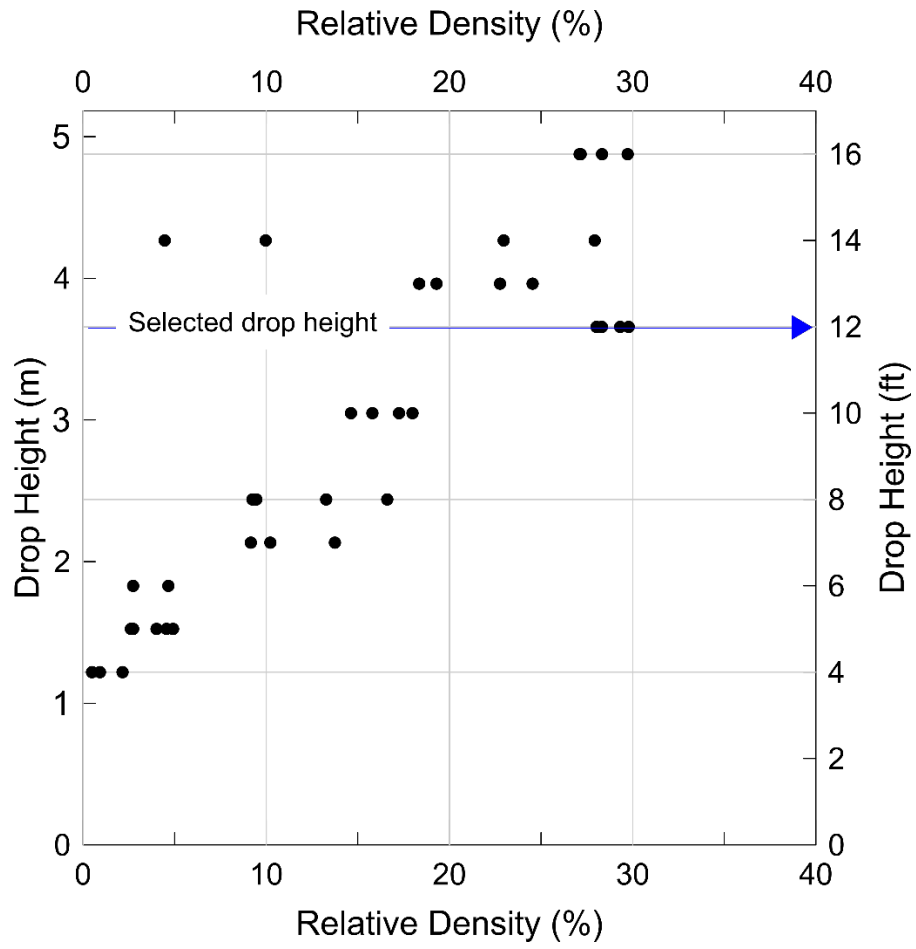


Figure 3-13 Relationship between relative density and pluviation drop height

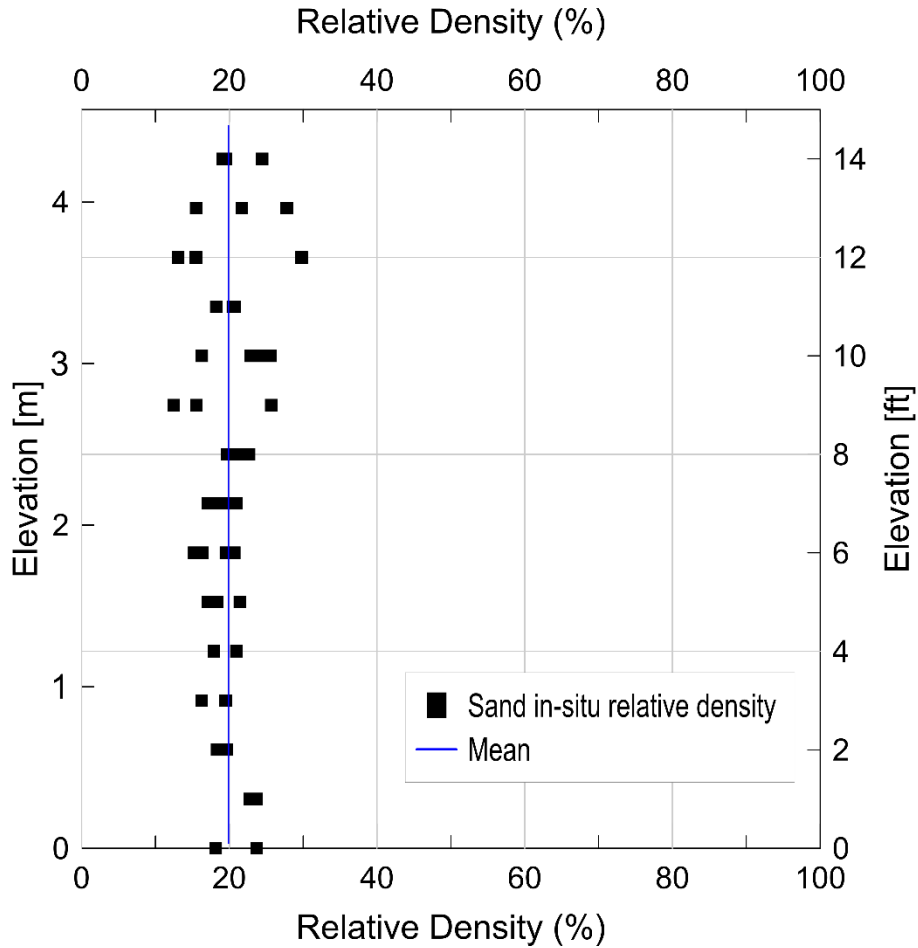


Figure 3-14 In-situ relative density profile measured during pluviation

Three types of in situ geotechnical investigation tests were performed, namely the Marchetti dilatometer test (DMT), the cone penetration test (CPT) and seismic cone penetration test (SCPT). The DMT test procedure and its correlations followed Marchetti (1997) and were performed following the ASTM D6635-15 guidelines. The material index ( $I_D$ ), horizontal stress index ( $K_D$ ), and dilatometer modulus ( $E_D$ ) were evaluated using Equations 3-1 to 3-5, where  $p_0$  = contact pressure needed prior to membrane expansion,  $p_1$  = contact pressure to produce a membrane displacement of 1.1mm,  $u_0$  = pore water pressure,  $\sigma'_0$  = in-situ vertical effective stress, and  $\mu_s$  = soil Poisson's ratio.  $I_D$ ,  $K_D$ , and  $E_D$  were determined to be 1.5 MPa

[217 psi], 2.8 MPa [406 psi], and 2.08 MPa [301 psi], respectively. The soil's elasticity modulus,  $E_s$ , can be obtained from the dilatometer modulus using Equation 3-4. The soil friction angle can be back calculated from the horizontal stress index  $K_D$  using Equation 3-5. The variation of soil's elasticity modulus and friction angle versus depth are shown in Figure 3-15. The average in-situ friction angle was found to be  $33^\circ$  and the average soil modulus ( $E_s$ ) was approximately 1.89 MPa [274 psi].

$$I_D = \frac{p_1 - p_2}{p_0 + u_0} \quad (3-1)$$

$$K_D = \frac{p_1 - u_0}{\sigma'_0} \quad (3-2)$$

$$E_D = 34.7(p_1 - p_2) \quad (3-3)$$

$$E_s = (1 - \mu_s^2) E_D \quad (3-4)$$

$$\phi' = 28 + 14.6 \log^2 K_D \quad (3-5)$$

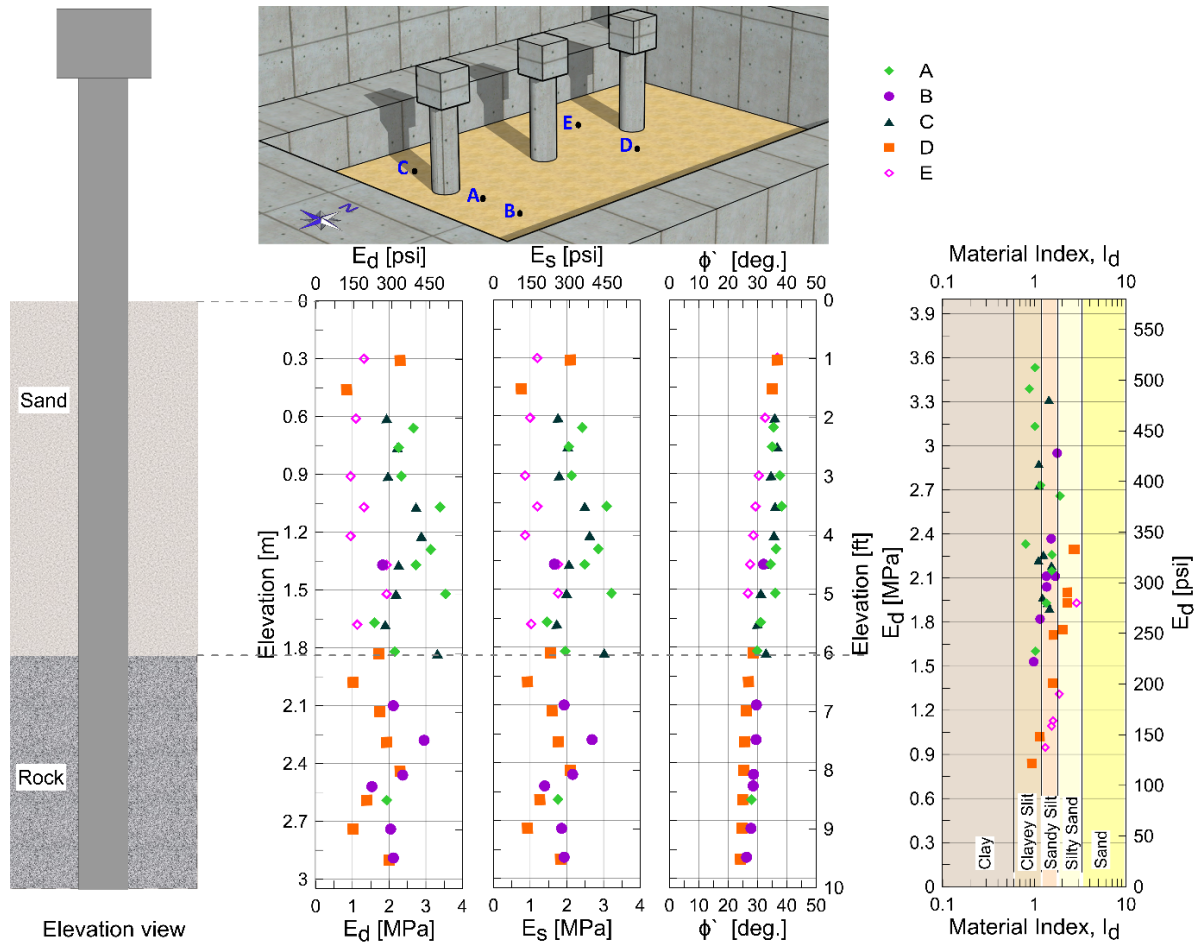


Figure 3-15. Flat dilatometer DMT test results at boreholes A, B, C, D, and E inside the soil pit

The cone penetration test (CPT) was performed following the ASTM D5778-20 guidelines. Figure 3-16 shows the results from the CPT soundings at boreholes A, B, C, D, and E. The shear wave velocity mean value of 78.6 m/s [258 ft/s] over the depth from 0.6 to 1.8 m [ 2 to 6 ft] was found based on Robertson (2012) correlations. The mean value of the sand friction angle over the depth from 2 to 6 ft was found through the correlations proposed by Kulhawy & Mayne (1990) and Robertson & Campanella (1983) to be 34 deg and 42 deg respectively as shown in Figure 3-17. The seismic cone penetrometer was pushed into the soil and shear waves generated at the surface by hitting a beam with a sledgehammer were collected at 0.3 m [1.0 ft] intervals. The shear wave velocity was then calculated from the difference of arrival

times. A sample of the SCPT results measured at the north-east side of specimen 2 is shown in Figure 3-18. The procedure followed to execute the SCPT test was based on pseudo-time interval method., at which the travel paths (The distance between the excitation source and the seismometer at a given depth) L1 and L2 of the seismic wave from the excitation source at the surface to the seismometer in the SCPT body at depths D1 and D2 respectively are used to derive the shear wave velocity in the interval between D1 and D2 as illustrated in Figure 3-18. It was observed that the shear wave velocity for the very first intervals are probably not accurate, that could be attributed to the s-wave mix up with the p-wave at shallow elevations, often seen in practice for such cases. SCPT shear wave velocity measurements suggested an average shear wave velocity ( $V_s$ ) of 220 m/s [722 ft/s].



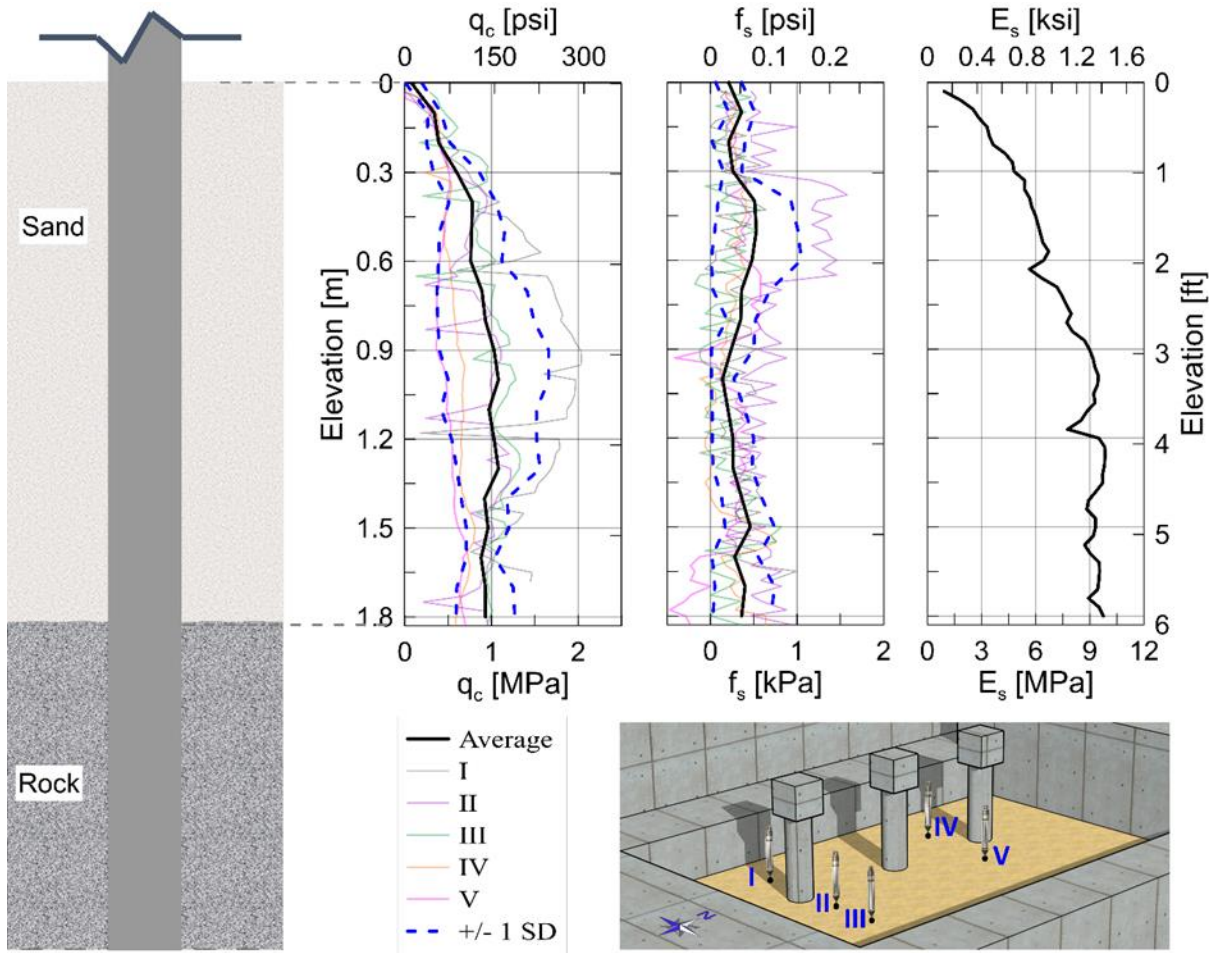


Figure 3-16 CPT test results at boreholes I, II, III, IV, and V inside the soil pit

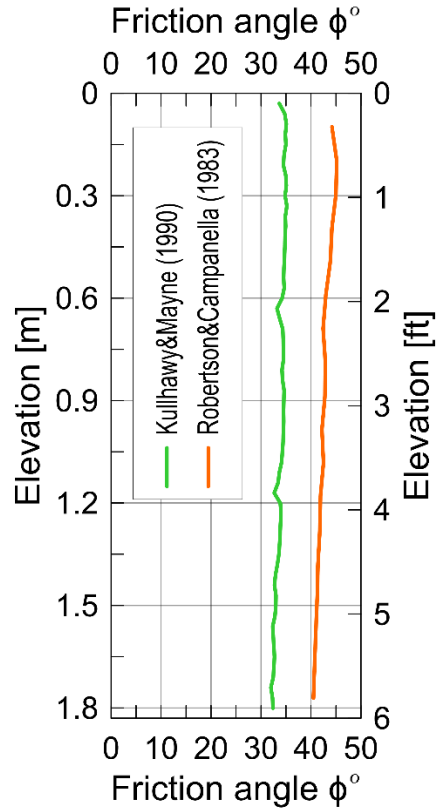


Figure 3-17 Sand friction angle correlated to the CPT measured data

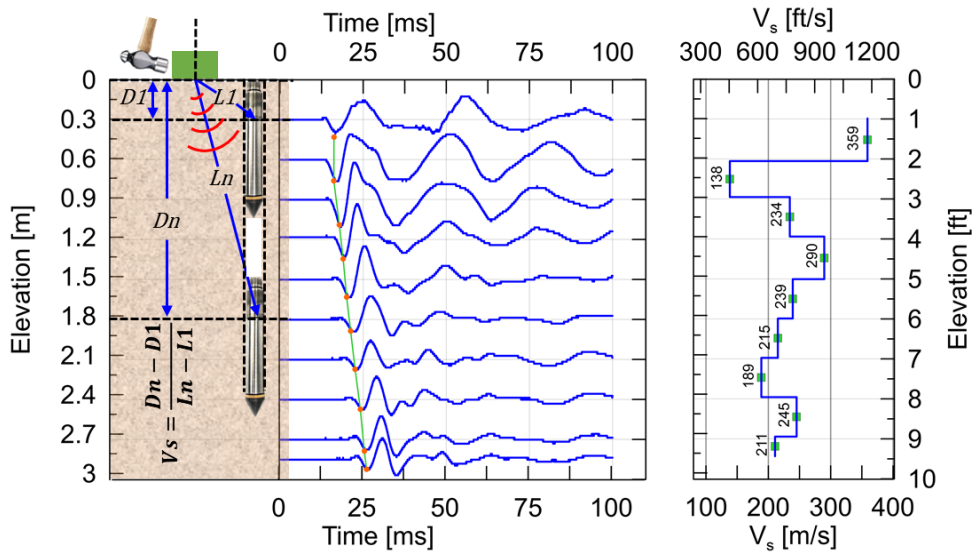


Figure 3-18. Shear wave velocity generated from the Seismic CPT collected data at the northeast of specimen 2

### 3.5. Specimen Construction

Figure 3-19 shows photographs during specimen construction. The overall construction sequence consisted of first constructing the shafts, then casting the simulated rock blocks around them; this is of course the opposite of normal construction procedures in which a drilled shaft is cast in a drilled hole, but was utilized here for convenience and to allow for careful specimen construction without damaging the extensive instrumentation network. After instrumenting all rebar cages outside the soil pit, the cages were placed inside Sonotubes and aligned along the wall of the soil pit (Figure 3-19b). Concrete was poured and manually vibrated to avoid sensor damage. The “shaft caps” were constructed after the shafts had cured for approximately one week. Along the socket lengths of the shafts (1.22 m [4 ft]), the shaft surfaces were roughened with a pneumatic needle scaler to improve adherence with the rock-block concrete and to better simulate the rough interface typical of a drilled rock socket. The shafts were then placed and secured inside the rock-block formwork (Figure 3-19c) and the block concrete was poured as shown in Figure 3-19d. The hardened rock blocks were connected to the strong floor via high-strength steel anchors. The space between the rock sockets, which is unaffected by the lateral shaft displacement since the rock blocks are anchored to the floor, was filled with geof foam (Figure 3-19f). The soil was placed in the pit by dry pluviation and leveled upon reaching the design height as shown in Figure 3-20. Pre- and post-lateral load test in-situ investigations were performed to further characterize the fill material as explained in the previous section. Figure 3-21 shows schematically the completed setup for all the specimens in the soil pit.

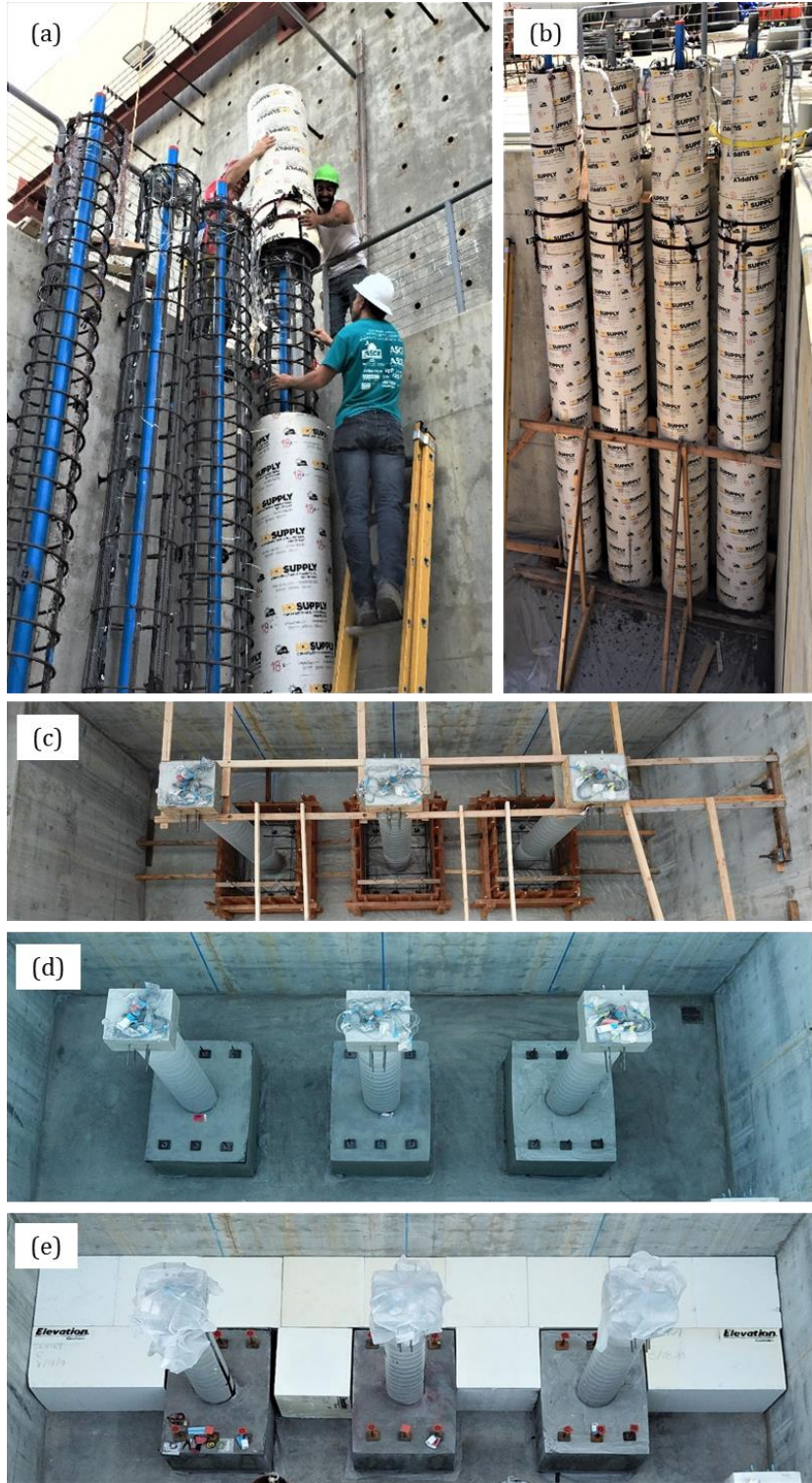


Figure 3-19 (a) Instrumented specimens prior to concrete pouring, (b) Shafts braced to the wall prior to concrete pouring, (c) Concrete shafts placed in rock-socket formwork, (d) Specimens with rock-sockets anchored into the floor (e) Geofabric blocks in place



Figure 3-20 Sand pluviation process

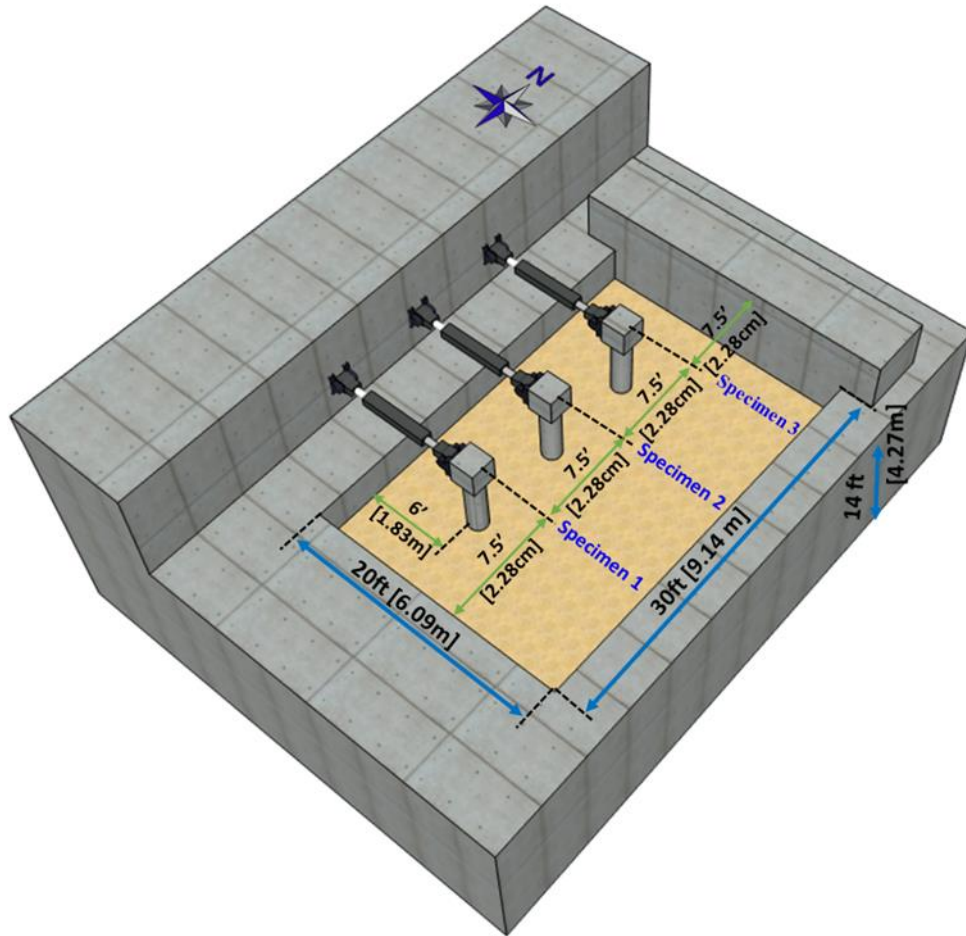


Figure 3-21 Specimen layout in the soil pit.

### 3.6. Load Application

#### 3.6.1. Testing without fill soil

Small amplitude lateral load testing without fill soil was conducted on specimen 1. The testing prior to adding the sand was intended to validate the structural behavior of the shaft within the linear elastic range. Figure 3-22 shows the test setup of the “no-soil” test. Prior to testing. The specimen’s experimental response was used to validate and refine the analytical moment-curvature ( $M-\phi$ ) relationship of the shaft as presented in Chapter 6. Shaft head lateral displacements were applied through the hydraulic actuator attached to the shaft cap

up to approximately 50% of the analytically predicted cracking displacement of the shaft (0.13 cm [0.05 in]). The corresponding applied lateral load was up to 3.6 kN [0.8 kips]. Figure 3-23 shows the shaft head applied displacement history and loading cycles adopted.

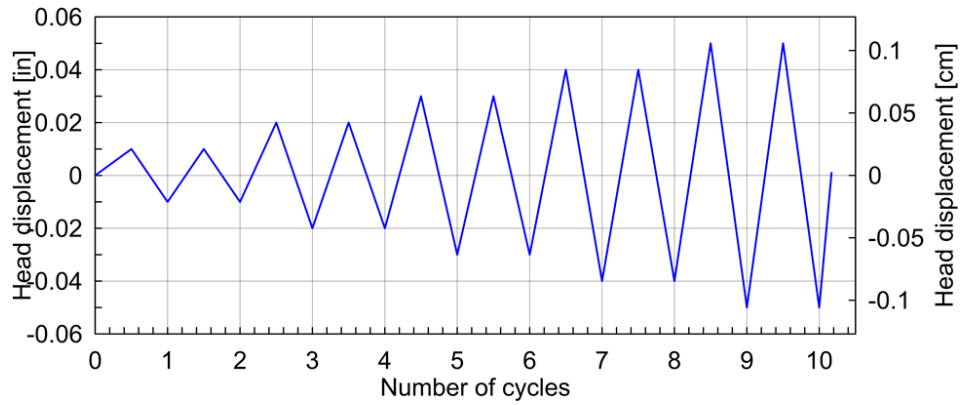


Figure 3-22 Shaft head displacement history and loading cycles for Specimen 1 testing without the sand

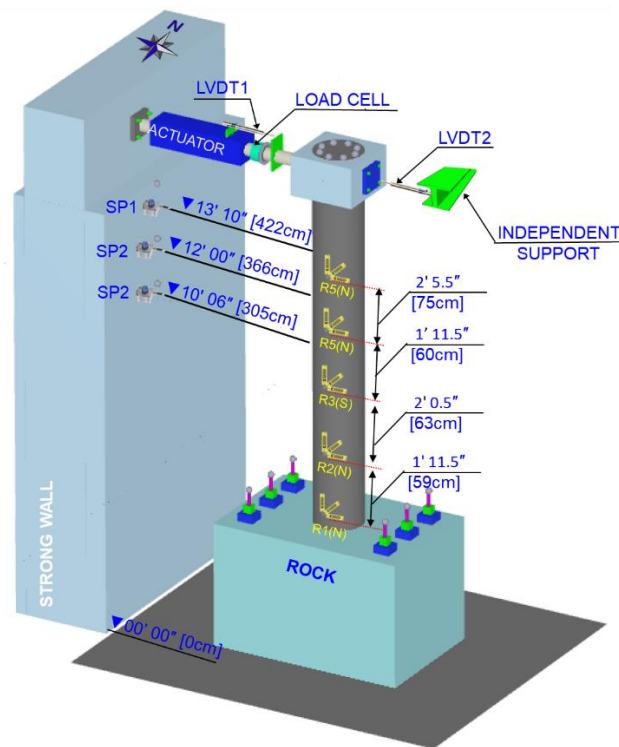


Figure 3-23 Completed test setup for specimen 1 testing without the sand

### **3.6.2. Testing with the fill sand**

The lateral loading protocol was developed based on the predictive analyses and followed the general guidelines of the ASCE 41-17 (2017) recommendations in which applied lateral displacement levels are selected as fractions or multipliers of the anticipated yield displacement. This approach is most commonly used for the seismic evaluation of structures and simulated the earthquake loading through quasi-static fully reversed cycles with progressively increasing displacement amplitudes. Loading was applied at the shaft head using three cycles per displacement level up to ultimate capacity. Hereafter, two cycles per displacement level were performed until substantial degradation of the lateral load-displacement relationship was noticeable as shown in Figure 3-20. Loading was applied under displacement control at the center of the shaft cap using a 76.2-cm [30-in] stroke, 667-kN [150-kip] capacity hydraulic actuator (see Figure 3-21). The strong wall of the UCI laboratory served as a reaction wall to the loading setup. The actuator was controlled by an MTS 407 dual-channel controller and data were recorded using a National Instrument data acquisition system. A total of 115 channels were utilized for each test. An externally installed LVDT, mounted between an independent reference frame and the backside of the shaft cap was used to control the experiment and record the shaft head displacement.



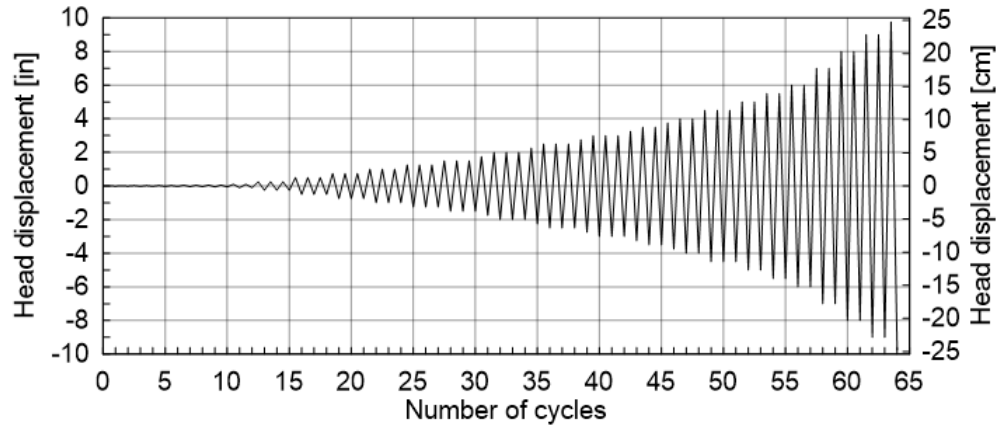


Figure 3-24 Shaft head displacement history and loading cycles for Specimen 1

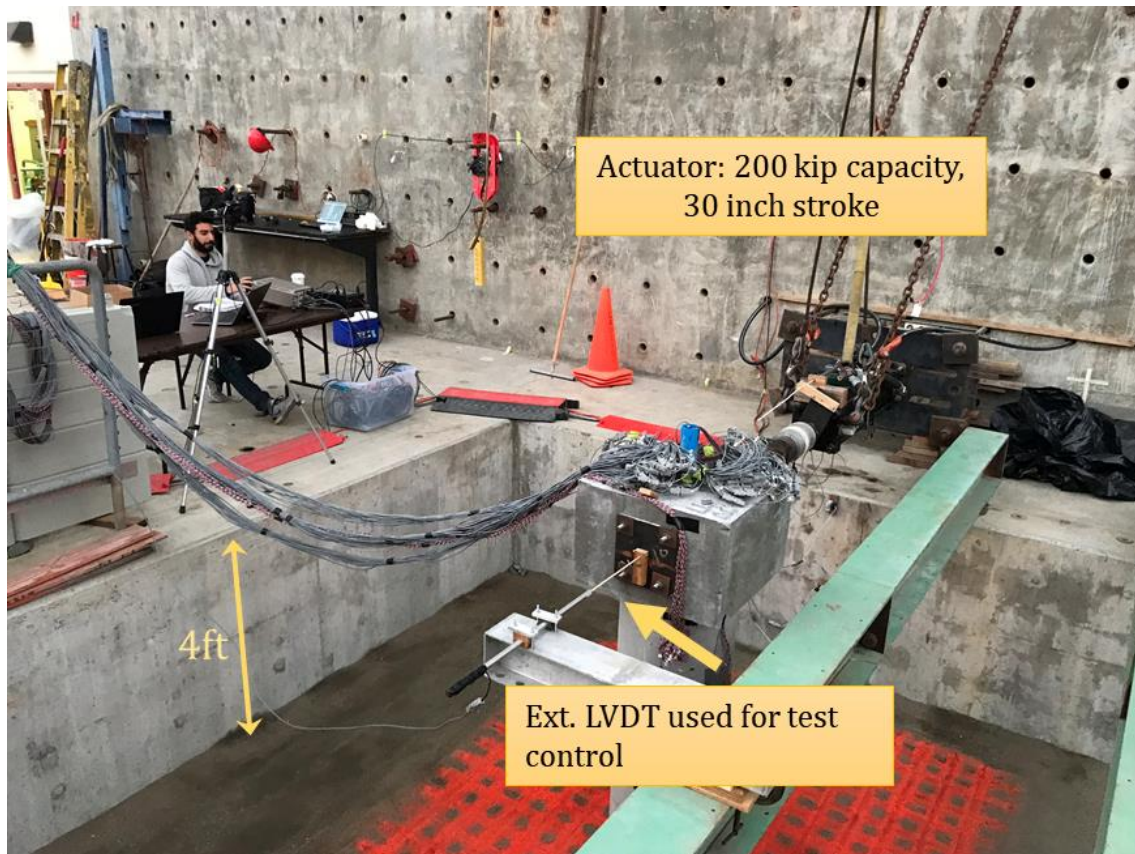


Figure 3-25 Completed test setup of specimen 1

### 3.6.3. Retesting with the added soil

Following test completion of specimen 2 and 3, they were retested (Test 2) under the same loading protocol but reduced cycles as shown in Figure 3-26; however, a sand layer of 4ft [1.2 m] thickness was added in an attempt to (1) identify potential post-test residual capacities, (2) strategically relocate the plastic hinge developed in Phase 1 to a higher elevation, and (3) separate the contribution of soil resistance from the overall shaft capacity in an attempt to better understand the soil structure interaction behavior of the foundation-soil system. The sand was pluviated following the same procedure mentioned in section 3.5. Figure 3-28 shows schematics of the specimen configurations and soil stratigraphy during testing in Phase 1 (Test 1) and Phase 2 (Test 2). Figure 3-29 shows the complete test setup of specimen 2 after adding the sand and before retesting.

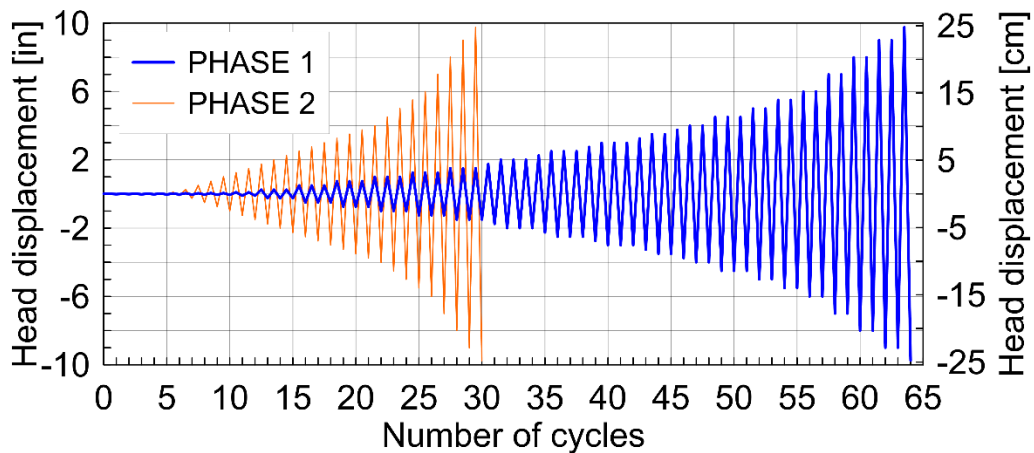
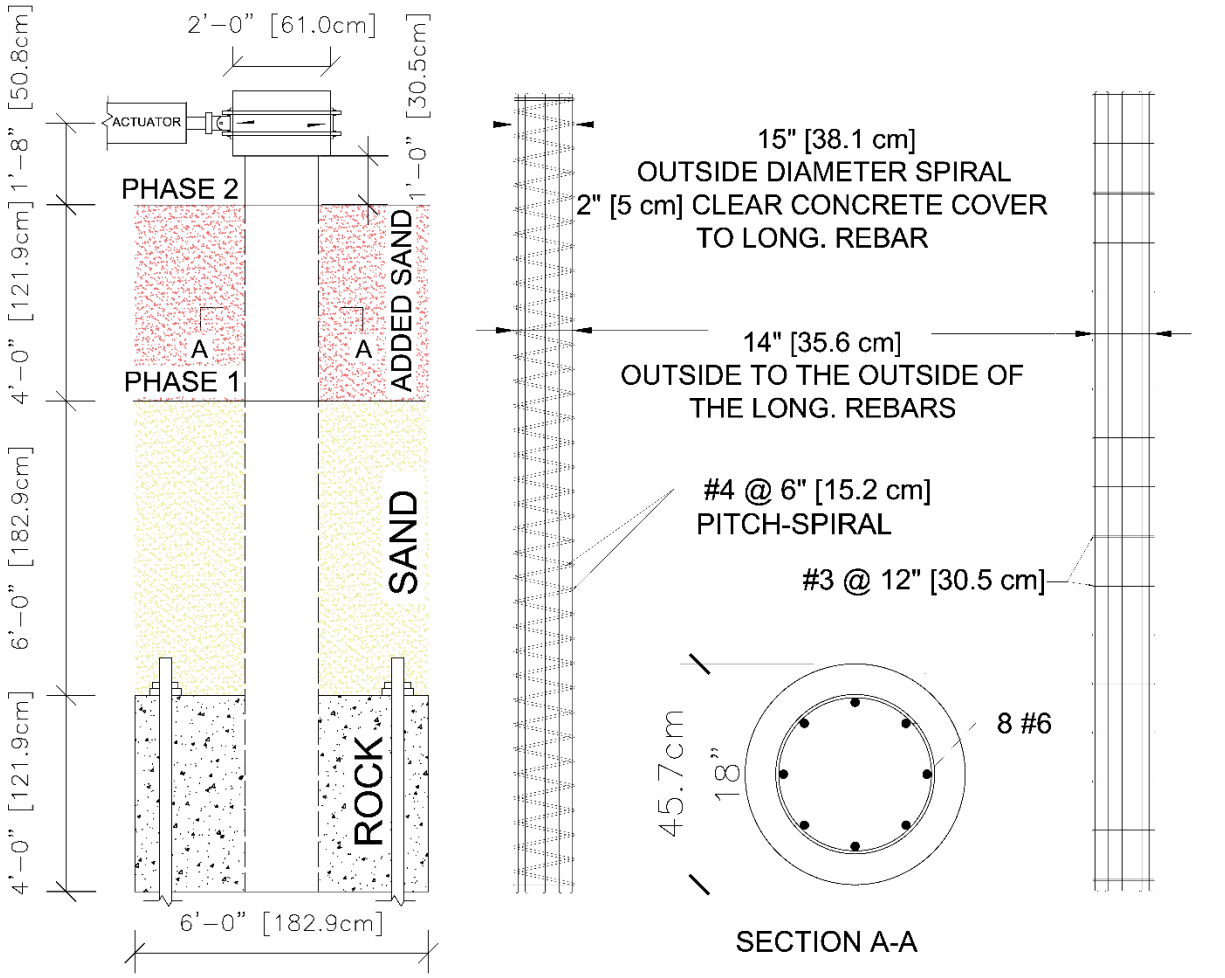


Figure 3-26 Shaft head displacement history and loading cycles for Phase 1 and 2



GEOMETRY

SPECIMEN 2

SPECIMEN 3

Figure 3-27 Schematic specimens' configuration and soil stratigraphy

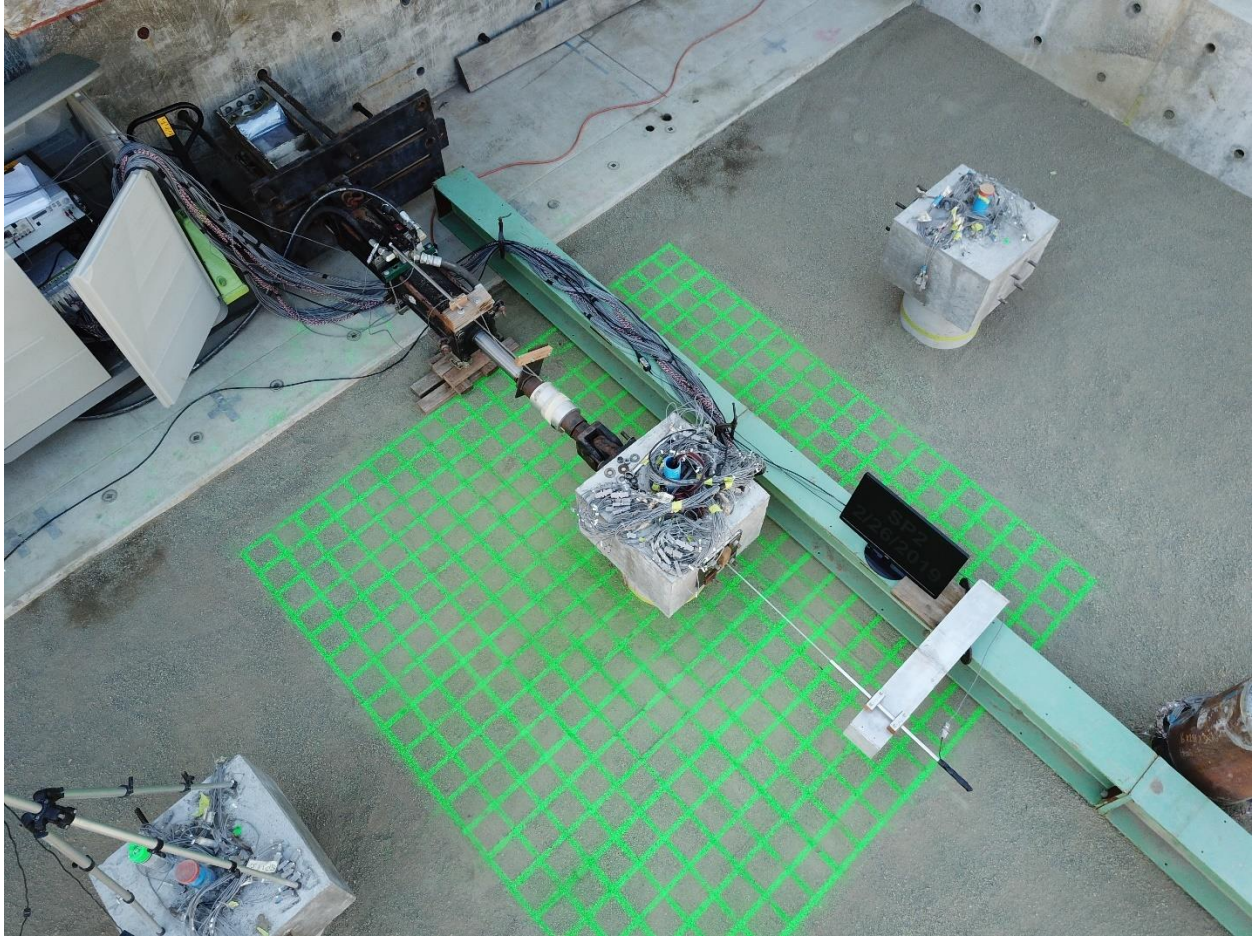


Figure 3-28 Completed test setup of Specimen 2 after adding the sand layer and prior to retesting.

### 3.7. Visual observations

A spray-painted grid with dimensions of 15 x 15 cm [6 x 6 in] was applied to the sand surface around the shaft specimen to monitor the extents of soil cracking, heaving, and caving as shown in Figure 6-7. Two fixed cameras were set up at two different angles and were set to capture one frame per five seconds. Following each test completion, the shaft surrounding soil was manually excavated to identify cracking patterns and detect the presence and approximate location of plastic hinge(s).



## Chapter 4 Instrumentation

### 4.1. Introduction

Specimen instrumentation consisted of external and internal sensors including linear voltage differential transducers (LVDT), string potentiometers (SP), inclinometers, and strain gauges in longitudinal (E/W) directions, as well as rosette (R), and tetrahedral configurations (T). Strain gauges arranged in rosette configuration were placed as surface strain gauges on the exterior concrete surface of the shaft. Strain gauges attached to a novel tetrahedral sensor carrier were placed inside the shaft section at multiple locations to capture internal shear strains. Figure 4-1 shows schematically the internal and external instrumentation plan.

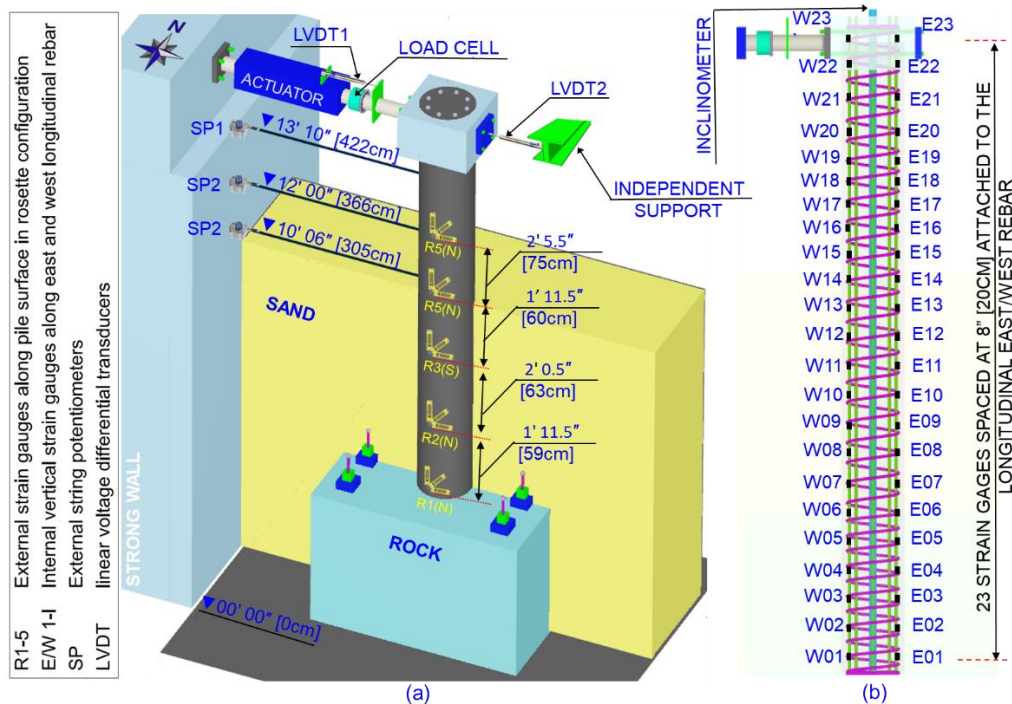


Figure 4-1 Instrumentation layout for Specimen 1: (a) External sensors; and (b) Internal sensors (tetrahedral sensors not shown)

## **4.2. Internal instrumentation**

### **4.2.1. Strain Gages**

Micro-Measurements model CEA-06-250UW-120 strain gages were installed on the longitudinal rebars of Specimen 1 and Micro-Measurements model CEA-06-240UZ-120 strain gages were installed on the longitudinal rebars of specimens Specimen 2 and 3. A precise procedure followed for installation of bonded strain gages on rebars which includes necessary materials and a recommended practice for surface preparation, installation, and protection of the strain gauges. Even though the flexural deformations were expected to approach yield and form a plastic hinge at around 3.5 shaft diameters below the ground level, Strain gages were attached longitudinally along the whole shaft height on two longitudinal opposite rebars with an approximate spacing of 8 inches to capture the curvature of the overall shaft profile as shown in Figure 4-1b above.

### **4.2.2. Inclinometer**

Two Geodaq modules model INC6-R216 in-place inclinometer modules were used. Each module is 8-feet in length and had 16 tilt sensors with 0.005-degree resolution spaced 6 inches apart. The two modules were connected end-to-end forming a continuous 16-foot chain of tilt sensors. 4-wheel centralizer were attached to the outside of the module housing every 50.8 cm [20 in] to allow for installation in 7 cm [2.75 in] diameter inclinometer casing which had grooves longitudinally to fit the centralizer wheels maintaining the orientation of the inclinometer in the plane normal to the axis of the casing. The casing was installed and secured in place at the centerline of the shaft rebar cage (see Figures 4-1b and Figure 4-2). A single cable connects the modules to Geodaq controller module version 4 (GCM4) to collect

the inclinometer displacement profiles in real-time and GCM4 PC software was used to process and store the inclinometer data.



Figure 4-2 Inclinometer setup

### 4.2.3. Tetrahedra

The Tetrahedra sensors development and calibration are discussed in detail in Chapter 5. Figure 4-3 shows schematically the tetrahedra that were used in this study. According to the prediction, significant shear deformations were expected to take place right below the rock-



soil interface, therefore, the tetrahedra were distributed and securely affixed to the shaft cage around these location as shown in Figures 4-4 through 4-6 for Specimen 1, 2, and 3 respectively. Tetrahedra were located at four different elevations starting right above the rock socket by 7.6cm [3 in] and spaced 15.2cm [6 in] apart approximately. The shear stresses were assumed to be identical in south and north directions (Homogeneous symmetric circular shaft cross-section and soil conditions surrounding the shaft are uniform), therefore it was more beneficial to move the north tetrahedra to the west and east direction to evaluate the shear stress distribution along the shaft specimens' cross-section at multiple locations (i.e., collect shear distribution data points across the cross-section rather than monitoring only maximum stresses in north and south directions). The new abbreviation for the tetrahedra kept the same for the ones located at south direction (T-S); however, for the ones that were moved to east or west a letter E or W were added to the abbreviation. All the tetrahedra were oriented to have the cord (a) perfectly vertical and the base (d, e, f) perfectly horizontal using zip ties at four different corners of each tetrahedron.

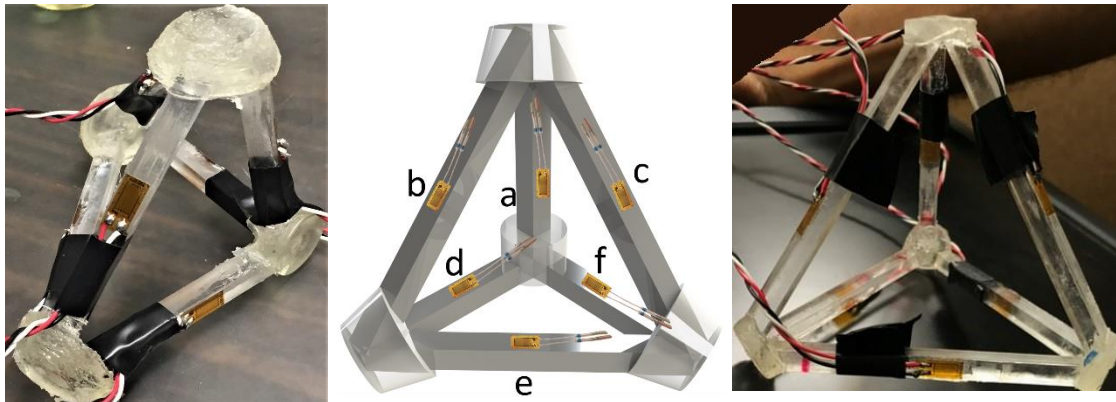


Figure 4-3 Tetrahedron strain gages carrier device with the six strain gages attached.

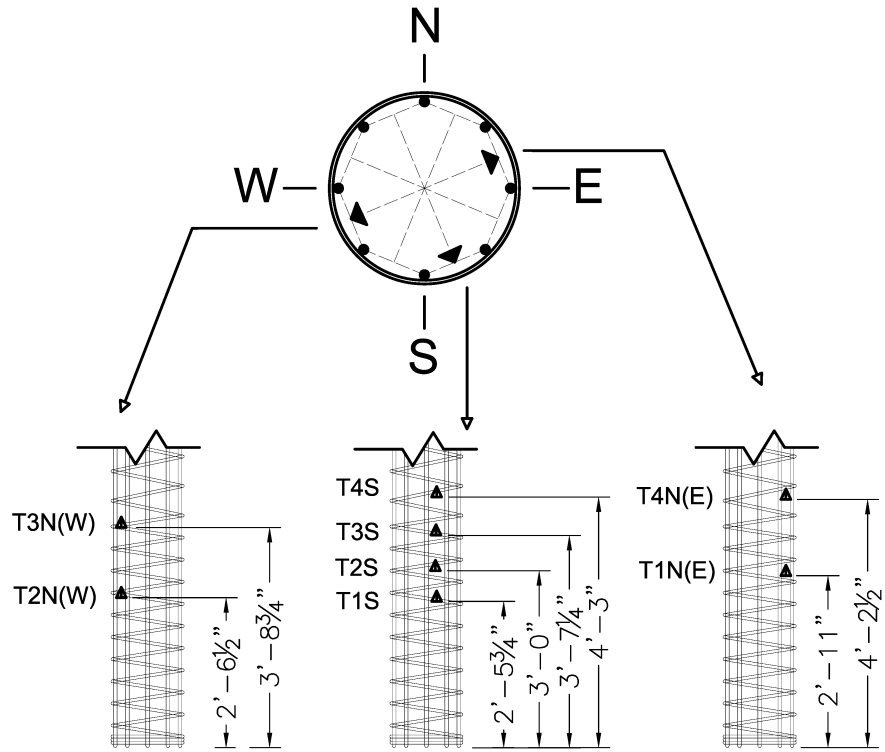


Figure 4-4 Tetrahedra layout for Specimen 1

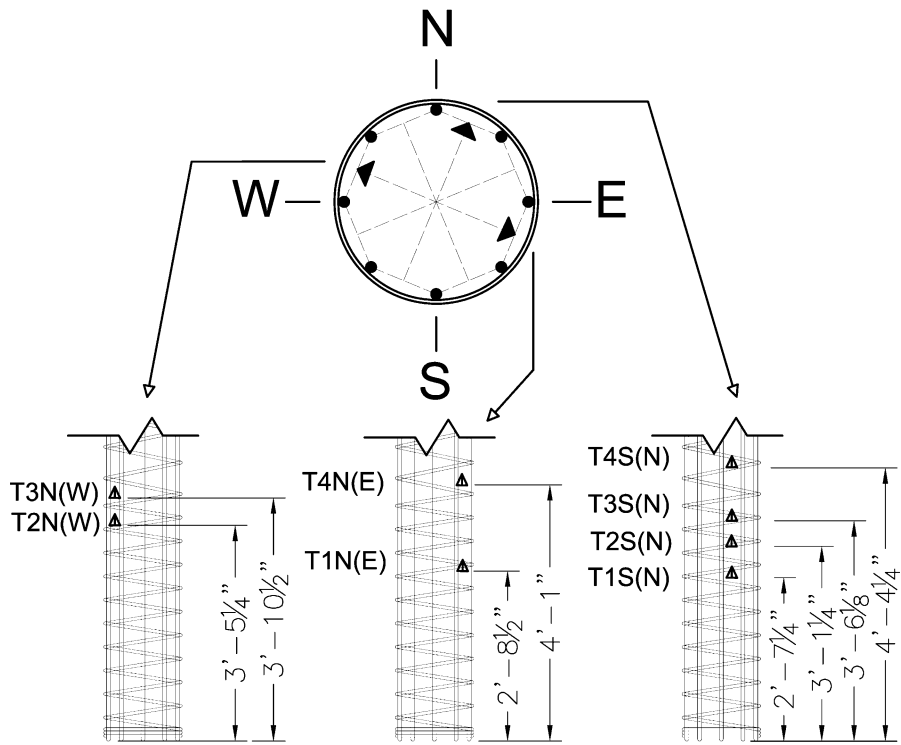


Figure 4-5 Tetrahedra layout for Specimen 2

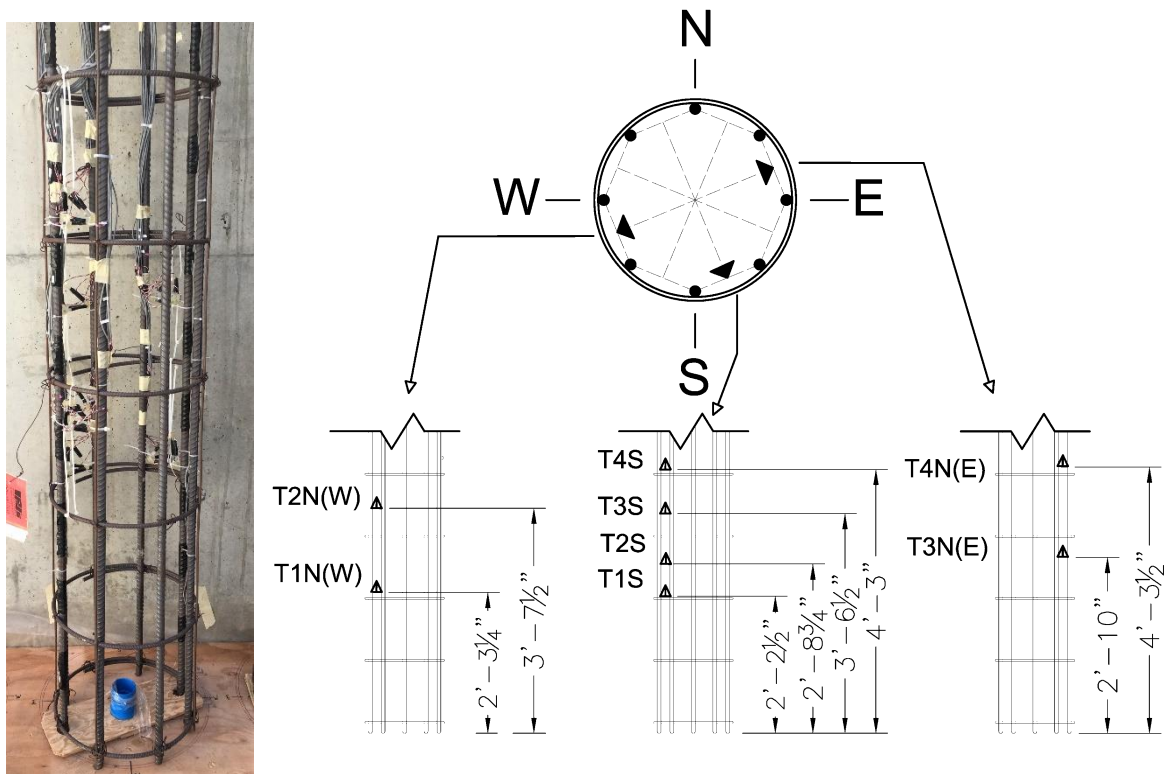


Figure 4-6 Tetrahedra layout for Specimen 3

### 4.3. External Instrumentation

#### 4.3.1. Strain Gages

External strain gages were installed at a 45° rosette configuration on the concrete surface of the Specimens 1 and 2 at multiple locations along the shaft height at south and north directions where the maximum shear stresses are expected to occur as shown in Figures 4-7 and 4-8 respectively. Micro-Measurements model C2A-06-20CLW-350 strain gages were used for rosettes R1 and R3 and model C2A-06-20CLW-120 strain gages were used for rosettes R2, R4, and R5. A precise procedure followed for installation of bonded strain gages on rebars which includes necessary materials and a recommended practice for surface preparation, installation, and protection of the strain gauges.

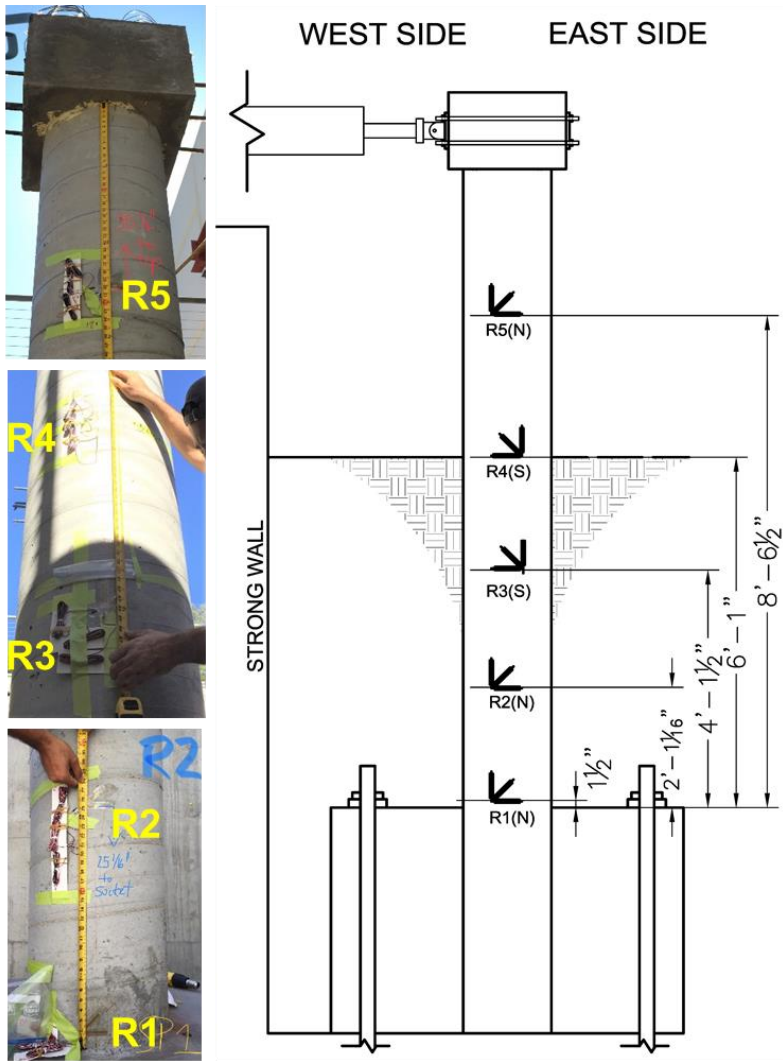


Figure 4-7 External strain gages rosettes for Specimen 1

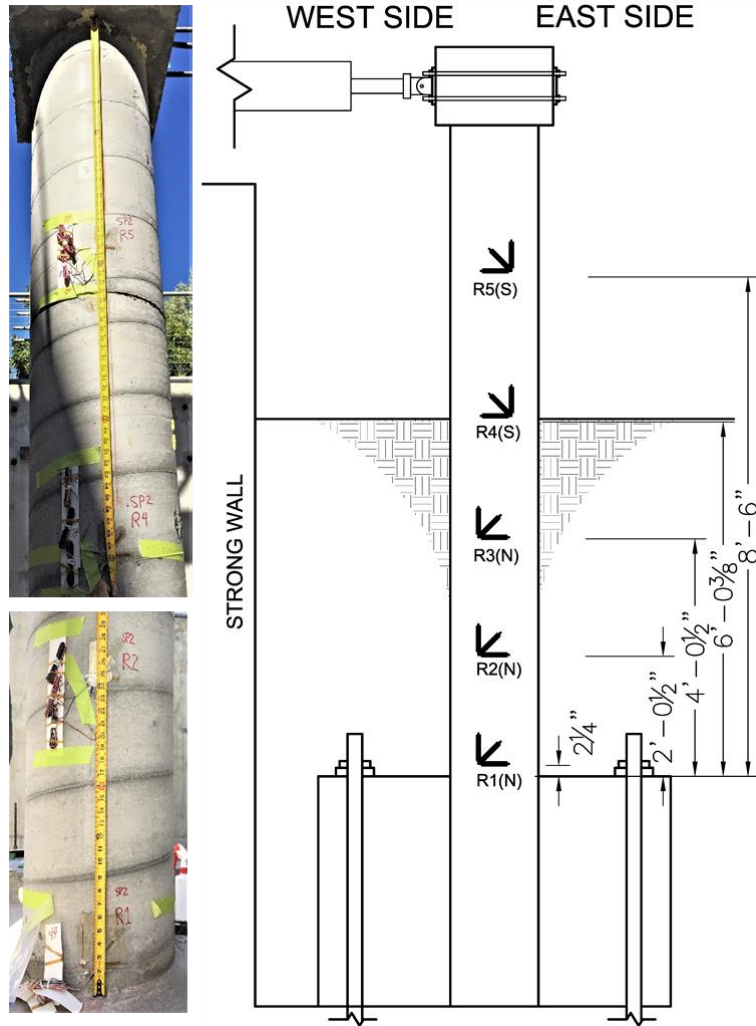


Figure 4-8 External strain gages rosettes for Specimen 2

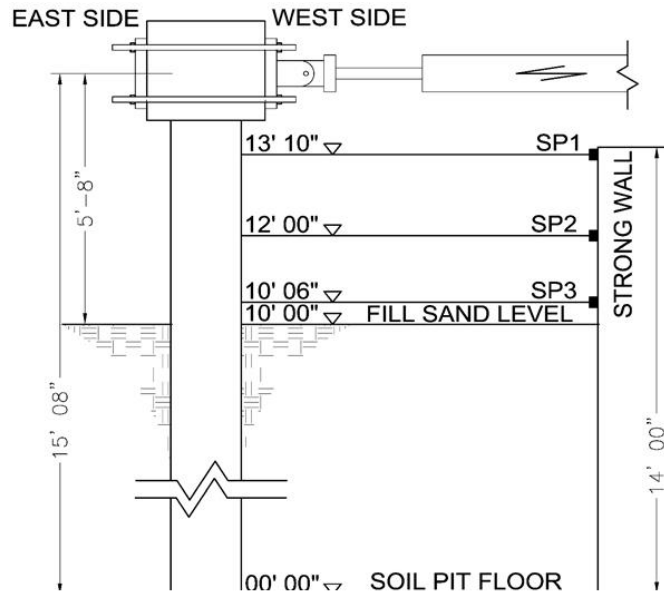
#### 4.3.2. String potentiometers (SP)

Celesco string potentiometers (<http://www.celescotransducers.com>) model SP1-25 were used to measure the shaft deformation above the sand (see specifications in Table 4-1). The locations of the string pots were identical for all the specimens. The string pots were mounted to the strong wall of the soil pit and hooked up to the above the ground portion of the shaft at three different elevations. One was mounted right above the sand level (SP1) at

3.2 m [10.5 ft] from the tip of the shaft. The other two (SP2 and SP3) were mounted at 3.65m [12 ft] and 4.2m [13.8 ft] from the shaft tip respectively (See Figure 4-9)

Table 4-1 elesco string potentiometers specification model SP1-25

Full Stroke Range	0-63.5 cm [0-25 inches]
Output Signal	voltage divider (potentiometer)
Accuracy	±0.25 to ±1.00%
Repeatability	± 0.05% full stroke
Measuring Cable	0.019-in. dia. nylon-coated stainless steel
Measuring Cable Tension	7 oz. (1,9 N) ±25%
Maximum Cable Acceleration	15 g
Enclosure Material	polycarbonate
Resolution	essentially infinite
Sensor	plastic-hybrid precision potentiometer
Input Resistance	10K ohms, ±10%
Recommended Maximum Input Voltage	30 V (AC/DC)
Output Signal Change Over Full Stroke Range	94% ±4% of input voltage
Electrical Connection	solder terminals
Operating Temperature	0° to 160°F (-18° to 70°C)



(a)



(b)

Figure 4-9 String pots SP1, SP2, and SP3 layout;(a) schematically; (b) as built

#### 4.3.3. AC Linear Variable Differential Transducers (LVDTs)

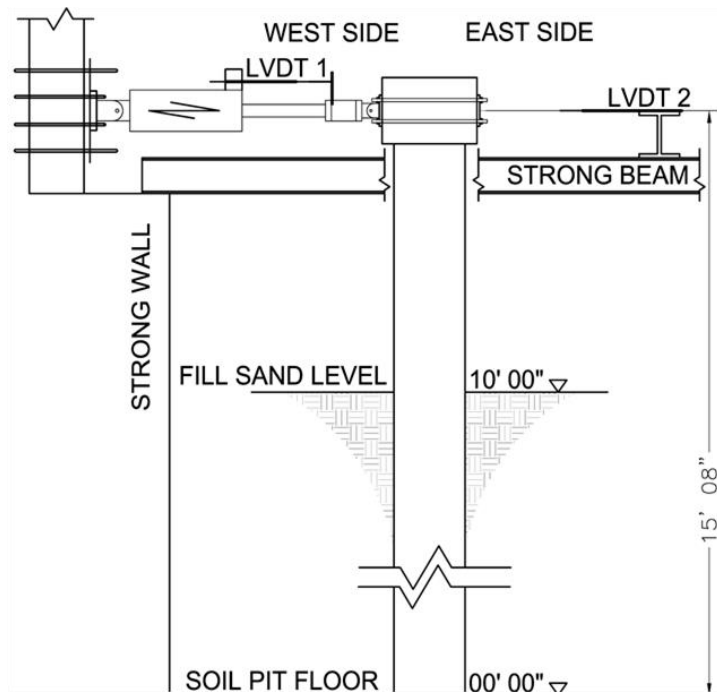
Two long-stroke AC LVDTs TransTek model 0222-00000 with stroke range of +/- 25.4 cm [+/- 10 inches] were used at identical locations for all tested specimens (see specification in Table 4-2). One LVDT was mounted between the hydraulic actuator body and the moving piston (LVDT 1) to control the actuator for the displacement-control testing as shown in Figure 4-10. The other LVDT was mounted between an independent reference frame and the

backside of the shaft cap (LVDT 2) and was used to control the experiment and record the shaft head displacement.

Table 4-2 Trans.Tek AC LVDT model 0222-00000 Specifications

Full Stroke Range	+/- 25.4 cm [+/- 10 inches]
Non-Linearity	$\leq \pm 0.25\%$ FS (Best Fit Straight Line)
Reference Frequency	7.0 KHz;
Sensitivity	0.50 V/V $\pm 10\%$ at FULL SCALE
Input Voltage	20 VRMS, Max.
Null Voltage	< 1.0% Excitation Voltage
Temperature Coefficient	< $\pm 0.001\%$ FS/ $^{\circ}$ F Zero, < $\pm 0.01\%$ Reading/ $^{\circ}$ F Span
TEMPERATURE RANGE	-67 $^{\circ}$ F to +257 $^{\circ}$ F (-55 $^{\circ}$ C to +125 $^{\circ}$ C) Operating -67 $^{\circ}$ F to +275 $^{\circ}$ F (-55 $^{\circ}$ C to +135 $^{\circ}$ C) Storage
Core	Chrome Plated Iron/Nickel Alloy





(a)



(b)

Figure 4-10 LVDTs locations, (a) schematically; (b) as built

## Chapter 5

### Development and Calibration of Novel Sensors

#### 5.1. Introduction

An innovative experimental prototype strain-gage based sensor development and calibration are presented in this chapter. The objective of these sensors is to capture the three-dimensional internal strain in a structure. Such measurements could improve our fundamental understanding of complex three-dimensional (3D) soil-structure interaction (SSI) by extracting volumetric measurements in deep foundation systems that could not be obtained in geotechnical engineering with any known method or device to date. Pioneering work on strain measurements performed in the early 1960s utilized uniaxial strain gauges in test specimens, whereby small material sections were extracted, strain gauges were attached to the sections, and then reinserted in the larger test specimen (Brasier & Dove, 1961; Serdengecti et al., 1962). This concept was extended into the 3D field by arranging strain gauges in 3D rosette configurations on various sides of an extracted specimen block or by attaching sensors on the inside of a cored section (Moore & Barrett, 2010). When reinserting the instrumented element into the original test specimen, limitations arise by introducing dissimilar interfaces (i.e., joints) through the bonding agent (e.g., glue) between the carrier material and the specimen material. The need for improved incorporation of the sensors inside the test specimen led to the development of gauge carrier sections in cubic or wafer form fabricated from the same material as the test specimen (e.g., Baker & Dove, 1963; Rossetto et al., 1975). Measurement accuracies must be carefully evaluated when using materials that cure highly exothermic, as surface softening/melting may cause unwanted gauge misalignment of the section (Little, 1982). Moreover, solid gauge carriers can

introduce construction joints between materials, which cause surface bonding weaknesses. To overcome these limitations, Slowik et al. (1998) successfully demonstrated the measurement of 3D core stresses developed in fiber reinforced concrete cubes using a set of fiber optic sensor (FOS) strands attached around a wire carrier. This mechanism allowed the test material to be poured around the wire carrier, which minimized the cross-sectional difference between the carrier and the test material. The sensor carrier was fabricated of brass and had a comparatively small cross section and a smaller modulus of elasticity than steel. This limits the sensor's influence on the strain field in the concrete. Only one test was performed by Slowik et al. (1998) as part of a materials research program and was not extended towards other structural or geotechnical applications. Another attempt to replicate this sensor in a similar manner was performed by Favaretti (2018). However Favaretti's configuration and materials led to unsuccessful sensor performance during construction and testing.

This chapter demonstrates the successful construction and application of a similar sensor device deployed in deep foundation testing. The proposed instrumentation is groundbreaking in that it will be the first attempt to measure 3D strains experimentally in foundation engineering using embedded sensor technology. The proposed sensors performance was evaluated first through a calibration process by locating them internally into a structural element (beam) at locations at which the internal strains are known. Following the successful prove of concept and calibration process, the proposed sensor was deployed into large scale testing of three rock-socketed shaft specimen to address the controversy over shear stresses explained in chapter 2 and fill in vital data gaps to enhance our progress towards performance-based foundation design. A successful development of

the proposed instrumentation will facilitate direct measurements superior to inverse data analyses and pave the way towards developing a more robust sensor than its current prototype version.

## **5.2. Theoretical background**

Predicting shear behavior of reinforced concrete structures is a crucial and challenging task which has not been fully solved yet. Deep foundation and infrastructure applications are complicated to be monitored due to lack of visual signs of failure (inaccessibility). Therefore, embedded instrumentation is needed. Internal strain at a point within the structure varies in all directions. All these strains contain significant physical information about the structural behavior under applied set of forces. Therefore, measurement of the interior strain is critical and could be very beneficial towards analyzing the structural response. To determine the strain tensor at a given point, three normal strains and six shearing strains must be known. Since there are only three independent shearing strains, the strain tensor is reduced to six independent strains. Therefore, a minimum of six normal strain components is needed to compute the strain tensor and that could be accomplished by impeding a carrier device of those six strain gages at the point of interest within the structure. The stress tensor could be further derived from the strain tensor following Hooke's law knowing the young's modulus of the material and Poisson ratio within the linear elastic range. Based on the Cauchy's stress theorem the stress vector on any plane passing through a point can be found through coordinate transformation equations by knowing the stress vectors on three mutually perpendicular planes at that point.

### 5.3. Tetrahedron prototype assembly

The proposed instrumentation, a tetrahedron shaped element, hereafter called intelligent tetrahedron (*iTET*), is constructed with a stiffness ( $EI$ ) adaptable skeleton and composed of three equilateral triangles that serve as a 3D gauge carrier. The concentric arrangement reduces the influence of normal bending strains and allows for capturing of volumetric expansions or contractions resulting from the imposed loading. Ideal *iTET* dimensions should be three to four times as long as the concrete's maximum aggregate size to enable strain averaging within the inhomogeneous composite material. The tetrahedra skeletons were assembled using 3d printed molds and its struts were connected using a high-strength epoxy-based adhesive specifically selected for the application at hand. Figure 5-1 and 5-2 shows the tetrahedron configuration prior to attaching the strain gages to its struts and Figure 5-3 shows the completed sensor with the strain gages attached. *iTET* struts had cross-sectional dimensions of 0.64cm [0.25 in] square and were made of acrylic material with an E-modulus of 2826.85 MPa [410 ksi] (approximately 10% of the concrete modulus). The material's axial compressive and tensile strength were 100 MPa [14.5 ksi] and 70 MPa [10.15 ksi], respectively. The struts were connected through cast-in-place corner caps to ensure maximal anchorage when the sides are strained with the deformed material. Given the carrier material's flexibility relative to that of the cast specimen, the embedded *iTET* is expected to deform with the applied loading and could be used in a wide range of structures without significant impact on the mechanical properties of its host.



Figure 5-1 Tetrahedra carriers

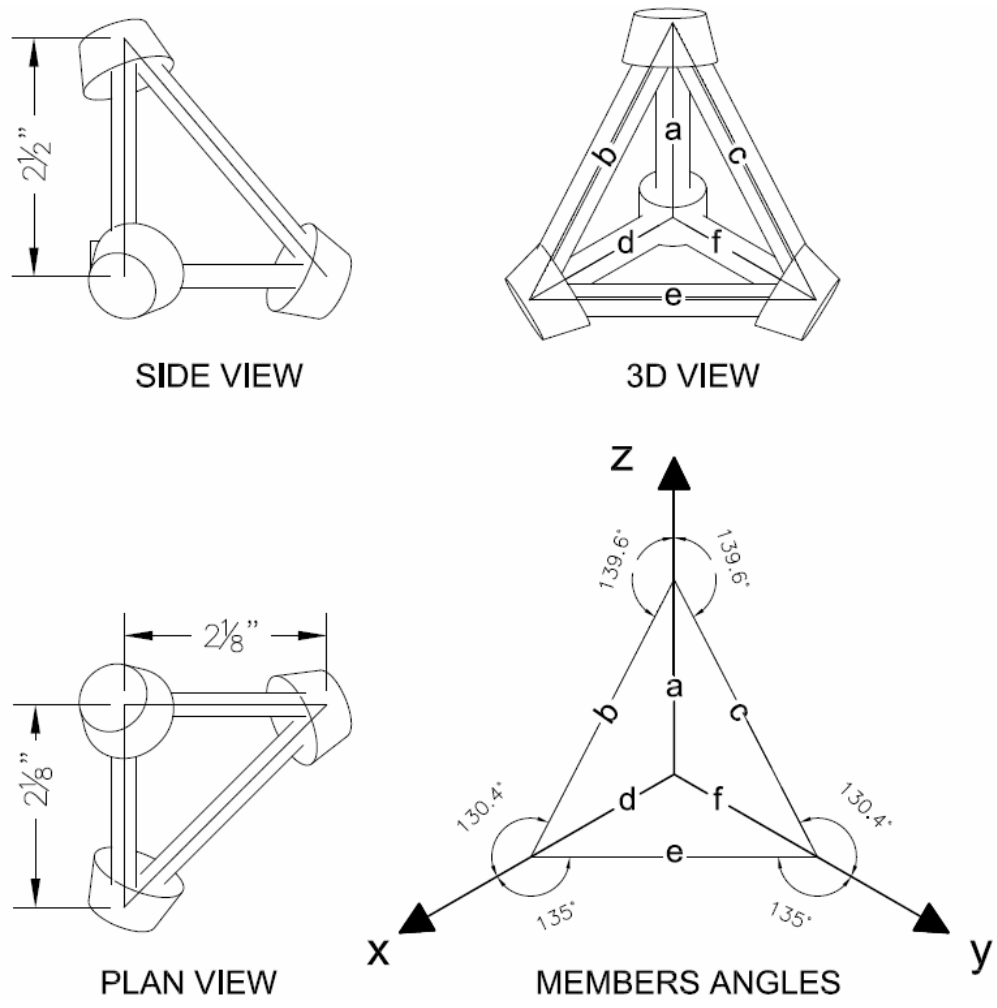


Figure 5-2 Schematic tetrahedron configuration

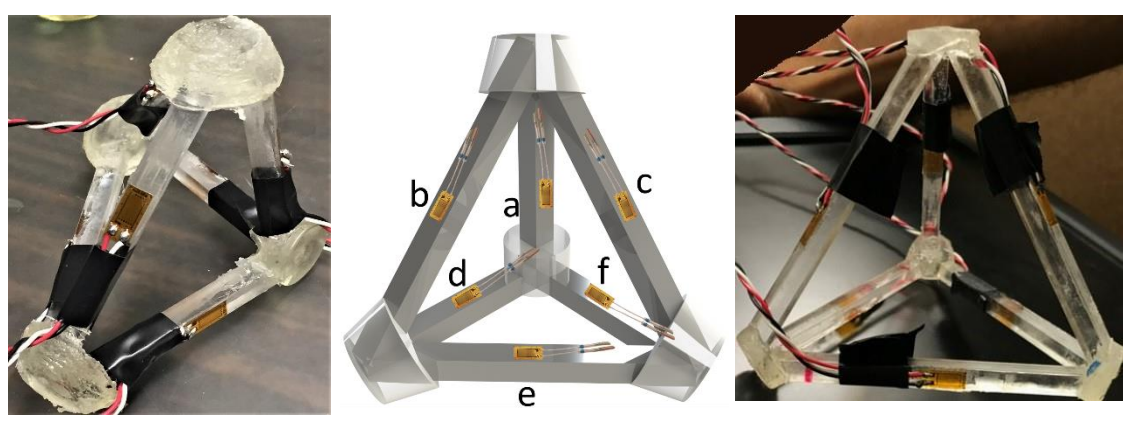


Figure 5-3 Tetrahedron strain gage carrier device with the six strain gages attached

#### 5.4. Strain transformation

The strain at the direction of the strain gages (a, b, c, d, e, f) can be expressed as a function of the strain components in the rectangular system of coordinates ( $x \perp y \perp z$ ) and the directions cosine in which the strain components in the rectangle system are  $\varepsilon_x, \varepsilon_y, \varepsilon_z, \gamma_{xy}, \gamma_{yz}, \gamma_{zx}$  and the directions with x, y and z are assumed to be  $\alpha, \beta,$  and  $\gamma$  respectively (see tables 5-1). A set of six equations can be obtained:

$$\begin{aligned} \varepsilon_{(a,b,c,d,e,f)} = & \varepsilon_x (\cos \alpha)^2_{(a,b,c,d,e,f)} + \varepsilon_y (\cos \beta)^2_{(a,b,c,d,e,f)} + \\ & \varepsilon_z (\cos \gamma)^2_{(a,b,c,d,e,f)} + \gamma_{xy} \cos \alpha_{(a,b,c,d,e,f)} \cos \beta_{(a,b,c,d,e,f)} + \\ & \gamma_{yz} \cos \gamma_{(a,b,c,d,e,f)} \cos \beta_{(a,b,c,d,e,f)} + \gamma_{zx} \cos \gamma_{(a,b,c,d,e,f)} \cos \alpha_{(a,b,c,d,e,f)} \end{aligned} \quad (5-1)$$

Equation 5-1 in a matrix form (for computation purpose) becomes:

$$\begin{bmatrix} \varepsilon_a \\ \varepsilon_b \\ \varepsilon_c \\ \varepsilon_d \\ \varepsilon_e \\ \varepsilon_f \end{bmatrix} = \begin{bmatrix} \cos^2 \alpha_a & \cos^2 \beta_a & \cos^2 \gamma_a & \cos \alpha_a \cos \beta_a & \cos \gamma_a \cos \beta_a & \cos \gamma_a \cos \alpha_a \\ \cos^2 \alpha_b & \cos^2 \beta_b & \cos^2 \gamma_b & \cos \alpha_b \cos \beta_b & \cos \gamma_b \cos \beta_b & \cos \gamma_b \cos \alpha_b \\ \cos^2 \alpha_c & \cos^2 \beta_c & \cos^2 \gamma_c & \cos \alpha_c \cos \beta_c & \cos \gamma_c \cos \beta_c & \cos \gamma_c \cos \alpha_c \\ \cos^2 \alpha_d & \cos^2 \beta_d & \cos^2 \gamma_d & \cos \alpha_d \cos \beta_d & \cos \gamma_d \cos \beta_d & \cos \gamma_d \cos \alpha_d \\ \cos^2 \alpha_e & \cos^2 \beta_e & \cos^2 \gamma_e & \cos \alpha_e \cos \beta_e & \cos \gamma_e \cos \beta_e & \cos \gamma_e \cos \alpha_e \\ \cos^2 \alpha_f & \cos^2 \beta_f & \cos^2 \gamma_f & \cos \alpha_f \cos \beta_f & \cos \gamma_f \cos \beta_f & \cos \gamma_f \cos \alpha_f \end{bmatrix} \begin{bmatrix} \varepsilon_x \\ \varepsilon_y \\ \varepsilon_z \\ \gamma_{xy} \\ \gamma_{yz} \\ \gamma_{zx} \end{bmatrix} \quad (5-2)$$

The strain components in the rectangle system are obtained by taking the inverse of the transformation matrix as following:

$$\begin{bmatrix} \varepsilon_x \\ \varepsilon_y \\ \varepsilon_z \\ \gamma_{xy} \\ \gamma_{yz} \\ \gamma_{zx} \end{bmatrix} = \begin{bmatrix} \cos^2 \alpha_a & \cos^2 \beta_a & \cos^2 \gamma_a & \cos \alpha_a \cos \beta_a & \cos \gamma_a \cos \beta_a & \cos \gamma_a \cos \alpha_a \\ \cos^2 \alpha_b & \cos^2 \beta_b & \cos^2 \gamma_b & \cos \alpha_b \cos \beta_b & \cos \gamma_b \cos \beta_b & \cos \gamma_b \cos \alpha_b \\ \cos^2 \alpha_c & \cos^2 \beta_c & \cos^2 \gamma_c & \cos \alpha_c \cos \beta_c & \cos \gamma_c \cos \beta_c & \cos \gamma_c \cos \alpha_c \\ \cos^2 \alpha_d & \cos^2 \beta_d & \cos^2 \gamma_d & \cos \alpha_d \cos \beta_d & \cos \gamma_d \cos \beta_d & \cos \gamma_d \cos \alpha_d \\ \cos^2 \alpha_e & \cos^2 \beta_e & \cos^2 \gamma_e & \cos \alpha_e \cos \beta_e & \cos \gamma_e \cos \beta_e & \cos \gamma_e \cos \alpha_e \\ \cos^2 \alpha_f & \cos^2 \beta_f & \cos^2 \gamma_f & \cos \alpha_f \cos \beta_f & \cos \gamma_f \cos \beta_f & \cos \gamma_f \cos \alpha_f \end{bmatrix}^{-1} \begin{bmatrix} \varepsilon_a \\ \varepsilon_b \\ \varepsilon_c \\ \varepsilon_d \\ \varepsilon_e \\ \varepsilon_f \end{bmatrix} \quad (5-$$

3)



Table 5-1 Sensors angles [°]  $\alpha$ ,  $\beta$ ,  $\gamma$  with respect to x, y, z axis respectively

Strain gage	$\alpha$	$\beta$	$\gamma$
a	90	90	0
b	130.364	90	40.364
c	90	130.364	40.364
d	0	90	90
e	135	45	90
f	90	0	90

### 5.5. Stress tensor components

The stress tensor is an operator with physical properties which is the state of stress at a point within the structure. The stress tensor has nine components that completely define the state of stress at a point inside the structural element in the deformed state and satisfies certain laws for transformation as shown in Figure 5-4. Equilibrium requires that the summation of moments with respect to an arbitrary point is zero (conservation of angular momentum principal), therefore the stress tensor is symmetric and has only six independent stress components, instead of the original nine. The nine components that defines the state of stress at a point is shown in equation 5-4 which could be reduced to the six-component tensor shown in equation 5-5.

$$\text{The stress tensor} = \begin{bmatrix} \sigma_x & \tau_{xy} & \tau_{xz} \\ \tau_{yx} & \sigma_y & \tau_{yz} \\ \tau_{zx} & \tau_{zy} & \sigma_z \end{bmatrix} \quad (5-4)$$

Since  $\tau_{xy} = \tau_{yx}$ ,  $\tau_{xz} = \tau_{zx}$ , and  $\tau_{yz} = \tau_{zy}$ . The stress tensor could be reduced to six components:

$$\text{Stress vector} = \begin{bmatrix} \sigma_x \\ \sigma_y \\ \sigma_z \\ \tau_{xy} \\ \tau_{yz} \\ \tau_{zx} \end{bmatrix} \quad (5-5)$$

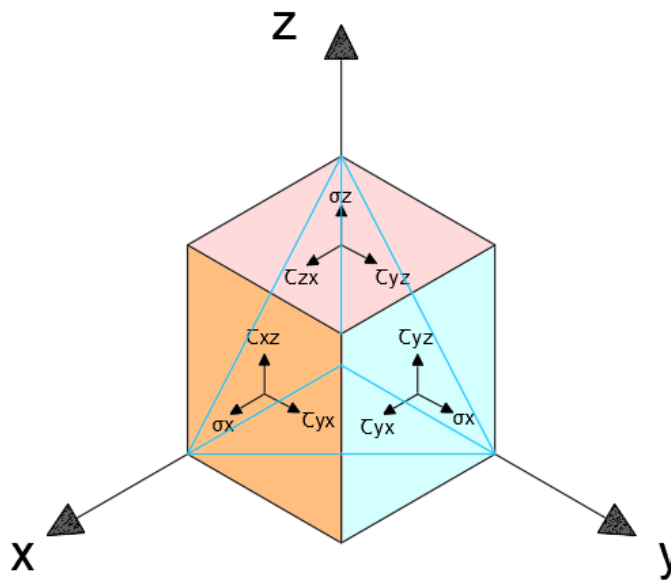


Figure 5-4 Components of stress in three dimensions

Since the iTET sensor is measuring strain not stress, transformation is needed. According to Hooke's law the six components of stress can be expressed as a linear function of the strain components within the linear elastic range knowing the young's modulus of the material and Poisson ratio as following:

$$\begin{bmatrix} \sigma_x \\ \sigma_y \\ \sigma_z \\ \tau_{xy} \\ \tau_{yz} \\ \tau_{zx} \end{bmatrix} = \frac{E}{(1+\nu)(1-2\nu)} \begin{bmatrix} 1-\nu & \nu & \nu & 0 & 0 & 0 \\ \nu & 1-\nu & \nu & 0 & 0 & 0 \\ \nu & \nu & 1-\nu & 0 & 0 & 0 \\ 0 & 0 & 0 & \frac{1-2\nu}{2} & 0 & 0 \\ 0 & 0 & 0 & 0 & \frac{1-2\nu}{2} & 0 \\ 0 & 0 & 0 & 0 & 0 & \frac{1-2\nu}{2} \end{bmatrix} \begin{bmatrix} \epsilon_x \\ \epsilon_y \\ \epsilon_z \\ \gamma_{xy} \\ \gamma_{yz} \\ \gamma_{zx} \end{bmatrix} \quad (5-6)$$

## 5.6. Proof of Concept Testing

The proposed sensors performance was evaluated through proof-of-concept testing using a small scale unreinforced concrete beam subjected to known loading. Similar test layouts have been used for other calibration procedures in literature (insert references). By placing sensors internally at predetermined locations at which the directional internal strains are known, data measurements can be validated by applying fundamental structural analysis concepts. Four tetrahedra were embedded along the length of the beam as shown in Figure 5-5. The tetrahedra were affixed in place using 3 mm [1/8 inch] balsa wood rods as shown in Figure 5-6a. Concrete was then poured and concrete cylinders with dimensions of 15.2 cm [6 inch] in diameter and 30.5 cm [12 inch] in height were taken on site per ASTM C39. The cylinder was instrumented and loaded uniaxially to measure young's modulus and poisson's ratio as shown in Figure 5-7. Youngs's modulus and poisson's ratio values measured from the concrete cylinder were 31040 MPa [4502 ksi] and 0.16 respectively.

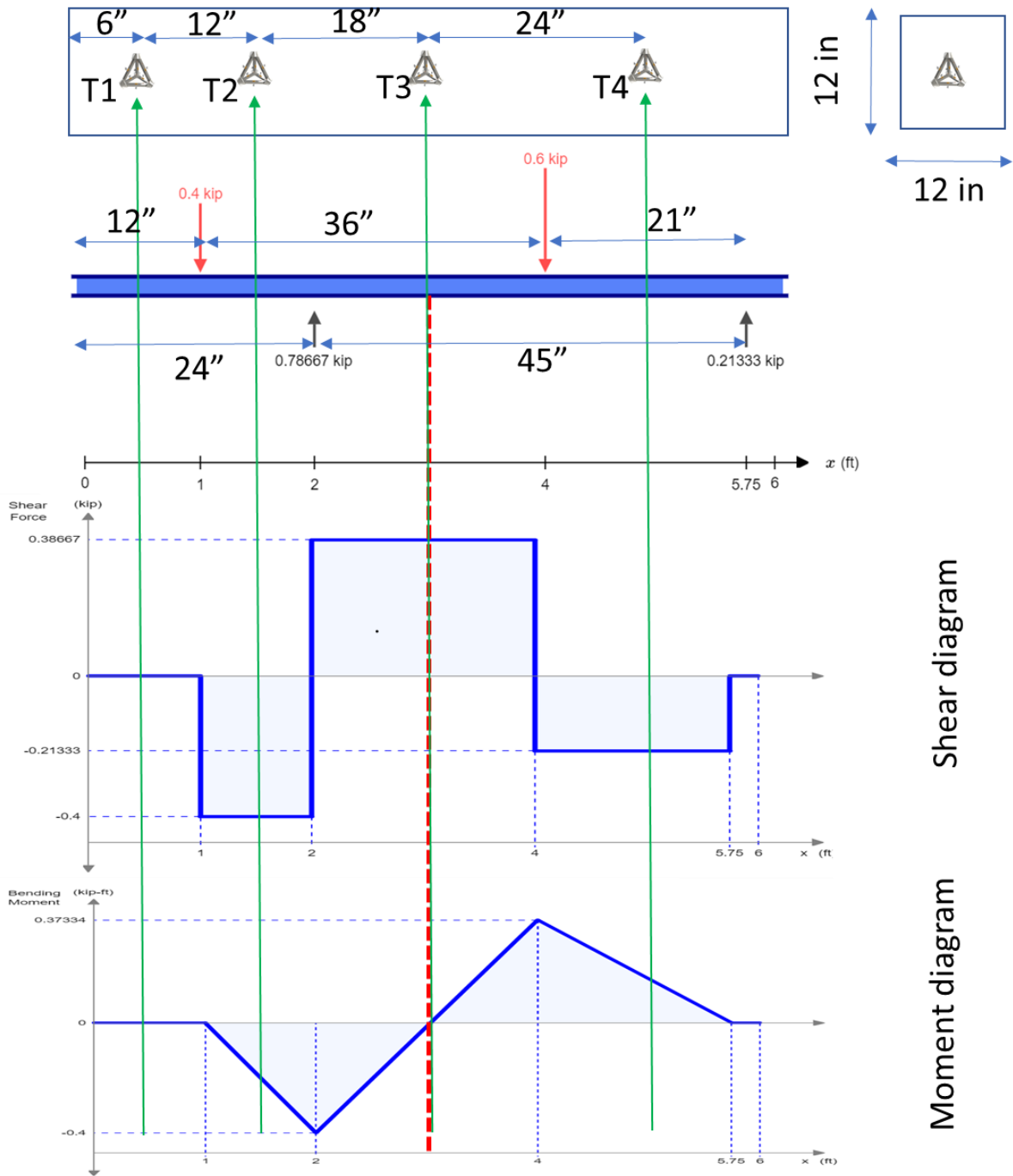


Figure 5-5 Locations of the tetrahedra and moment and shear diagram of the tested beam

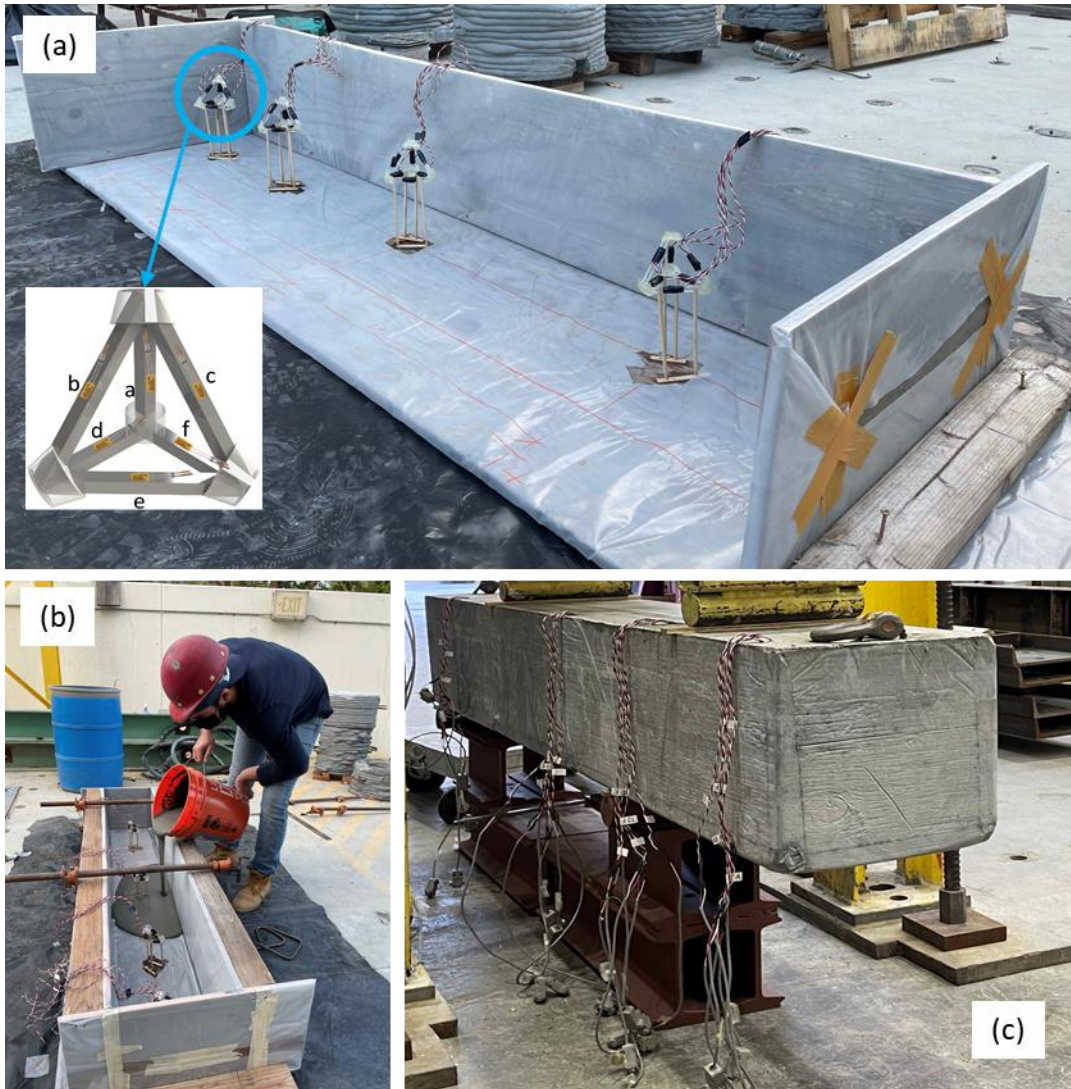


Figure 5-6 (a) affixed tetrahedra inside the beam formwork; (b) concrete pouring; and (c) cured completed beam

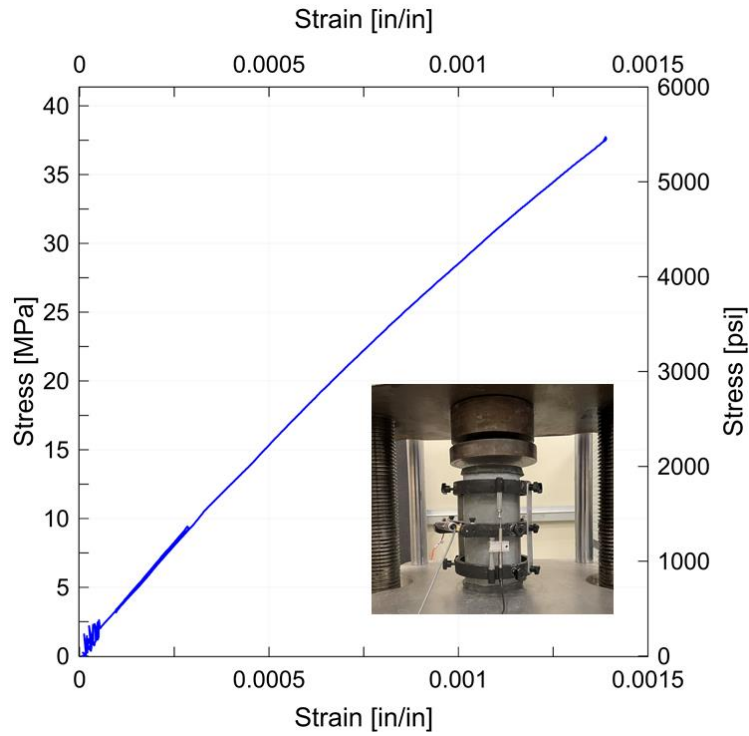


Figure 5-7 Concrete stress-strain relationship of the concrete at the day of beam testing

### 5.7. Load application

The beam was tested in a four-point test configuration. The loading configuration was designed to develop maximum shear and zero moment at the beam mid-span. The beam was loaded within the linear elastic range in a nondestructive load test protocol. The load was applied in an increment of 4.4 kN [1.0 kip] until the maximum applied load of 44 kN [10 kip] was reached. Unloading followed a similar pattern. The load was held at each target increment for 60 seconds. Figure 5-8 shows the completed test setup.



Figure 5-8 Completed test setup

### 5.8. Numerical simulation

Finite element analysis was used to numerically find the three-dimensional internal stresses of the tested beam. The finite element analysis was established by means of the commercial three-dimensional approach of PLAXIS 3D. The concrete beam was modeled via volume element and was assigned a linear elastic material model. The beam was subjected to the experimental load history and the internal shear stress response at any internal point was

extracted as shown schematically in Figure 5-9. The extracted shear stress response was used to validate the experimentally measured stresses by the tetrahedra.

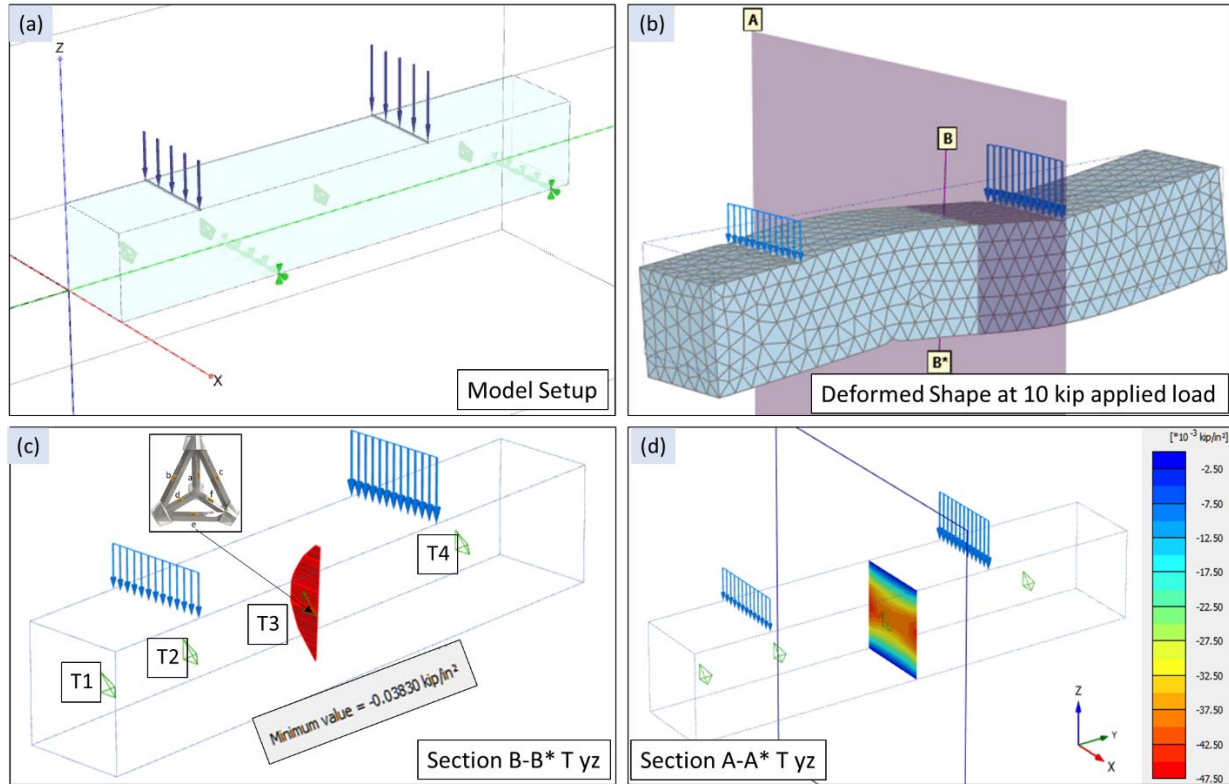


Figure 5-9 (a) Model setup; (b) Deformed shape at applied load of 10 kip; (c) Shear stress at an internal point extraction; and (d) Shear stress at selected yz plane.

### 5.9. Tetrahedron performance

Figure 5-10 shows exemplarily the response history of tetrahedron “T3”. The strains measured at the directions a, b, c, d, e, and f were transformed into global strain tensor following equation 5-3 above. The shear strain at the y-z plane was then transformed into shear stress following equation 5-6 above. The tetrahedra were located at the expected maximum shear stress and for a rectangular section the shear force could be calculated following equation 5-7.



$$V = \frac{\tau_{yz} A_{cross\ section}}{1.5} \quad 5-7$$

Figure 5-11 shows the measured shear strain, shear stress, and shear force histories, along with the applied load and the numerically obtained shear force. A comparison of measured shear versus numerically extracted shear at the beam mid-span is also shown in Figure 5-12. In a similar manner the measured shear by tetrahedra T1, T2, and T4 was compared to the numerically generated shear at each tetrahedron location, and the measured results show a very good agreement with the numerically generated results (see Figure 5-13).

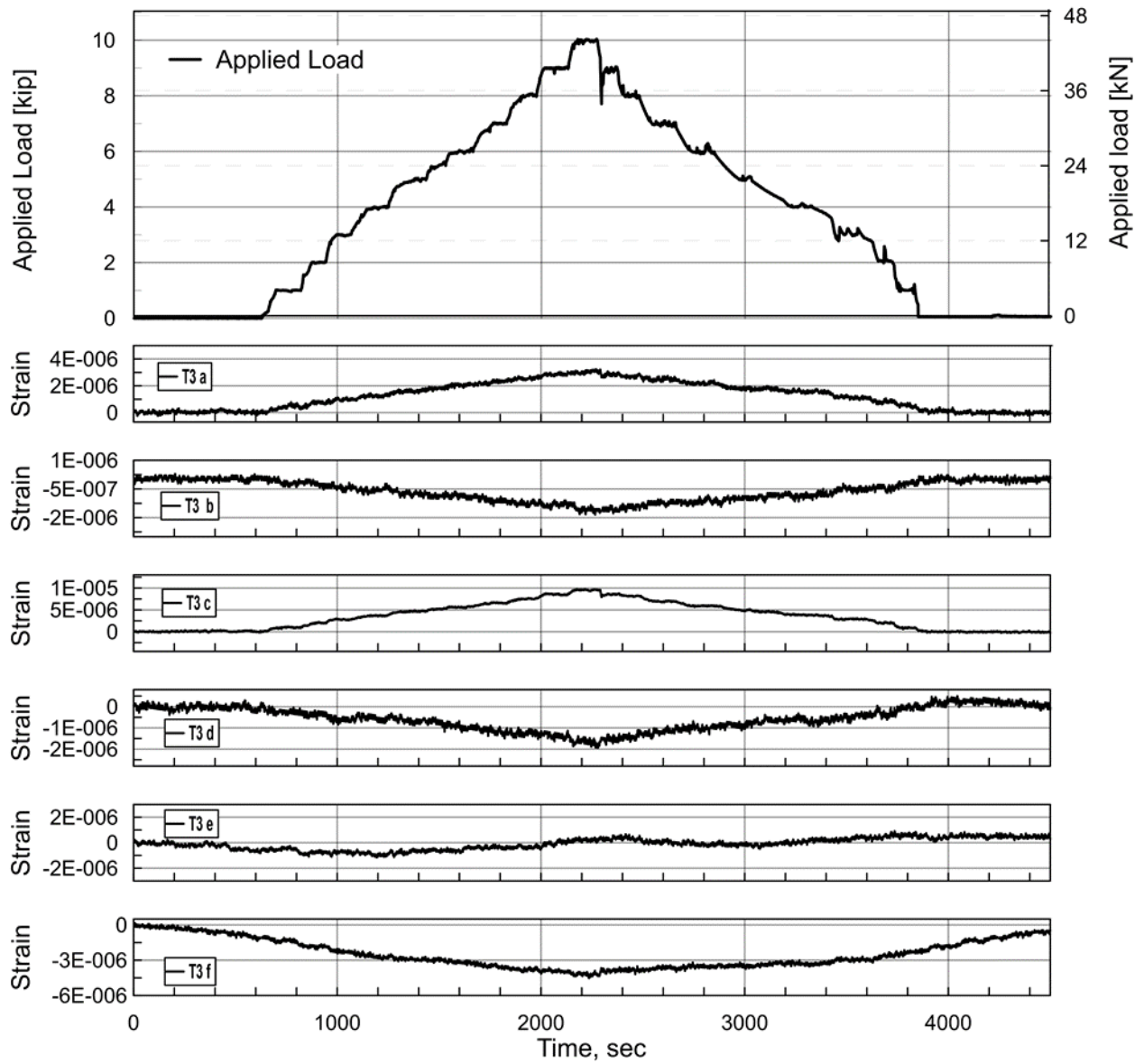


Figure 5-10 Tetrahedron T3 response history

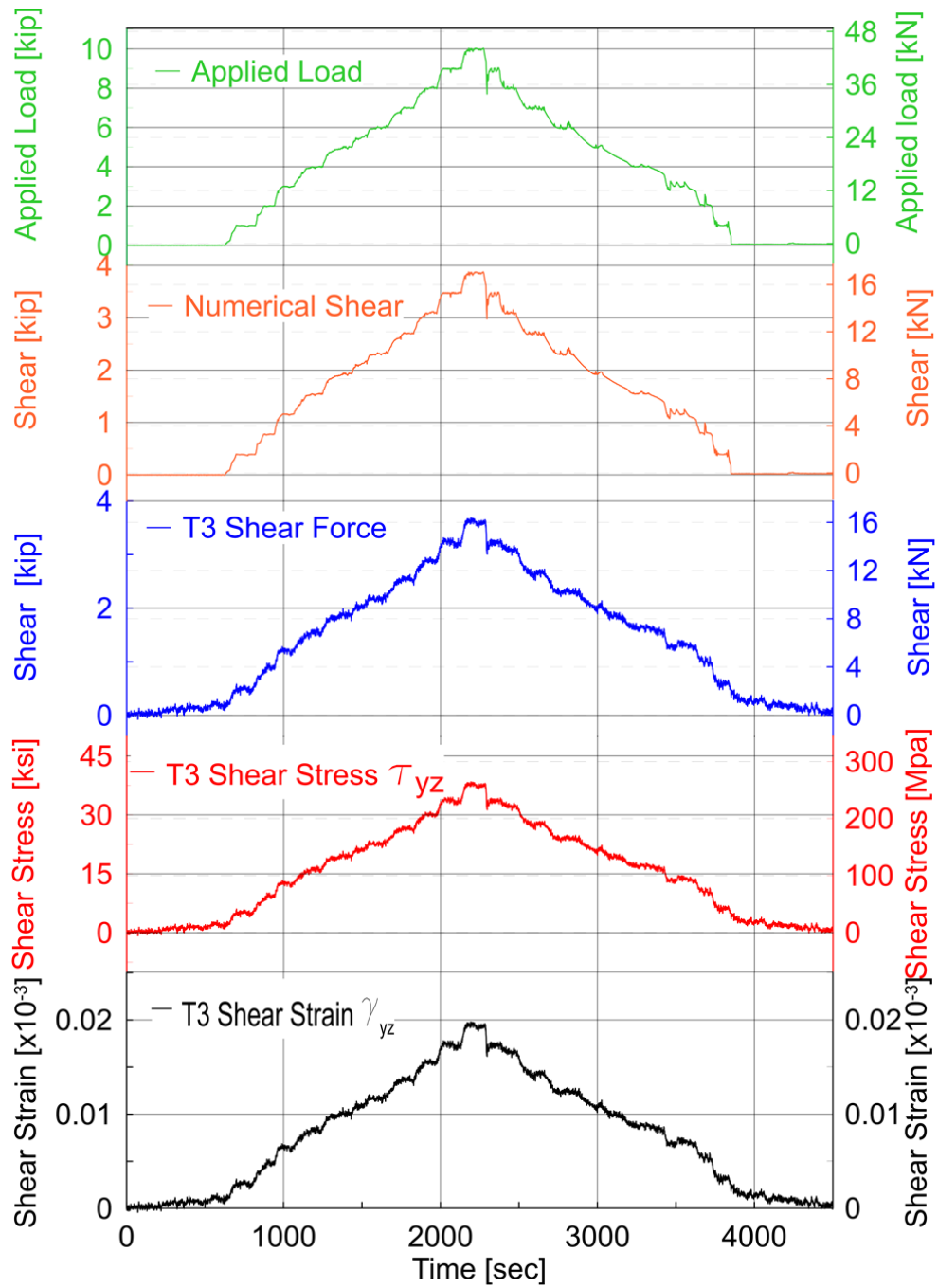


Figure 5-11 Measured and numerically generated shear strain, stress, and force histories

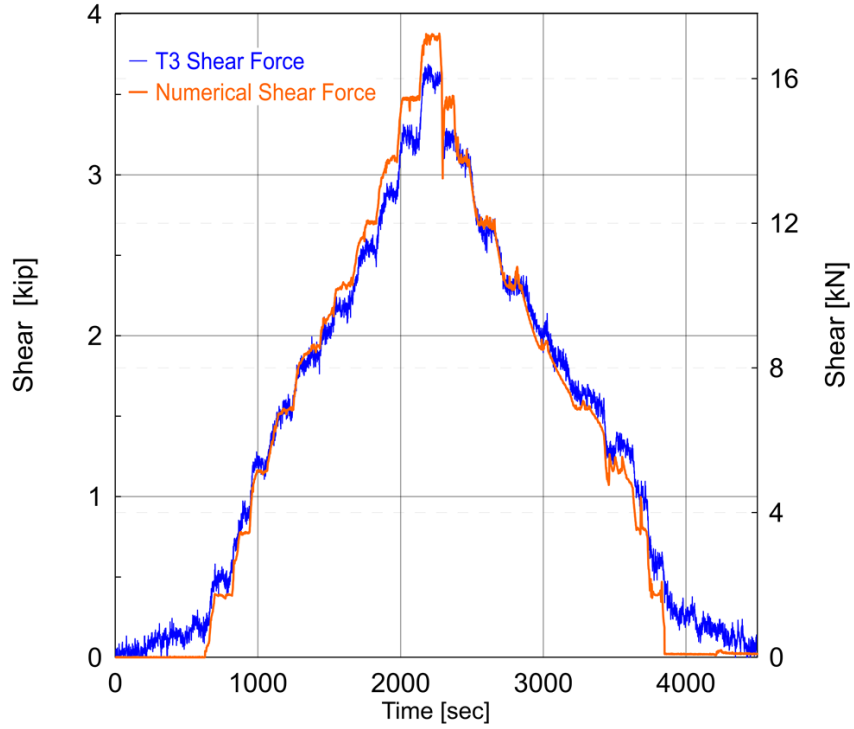


Figure 5-12 Measured shear versus numerically generated shear comparison at the beam mid-span.

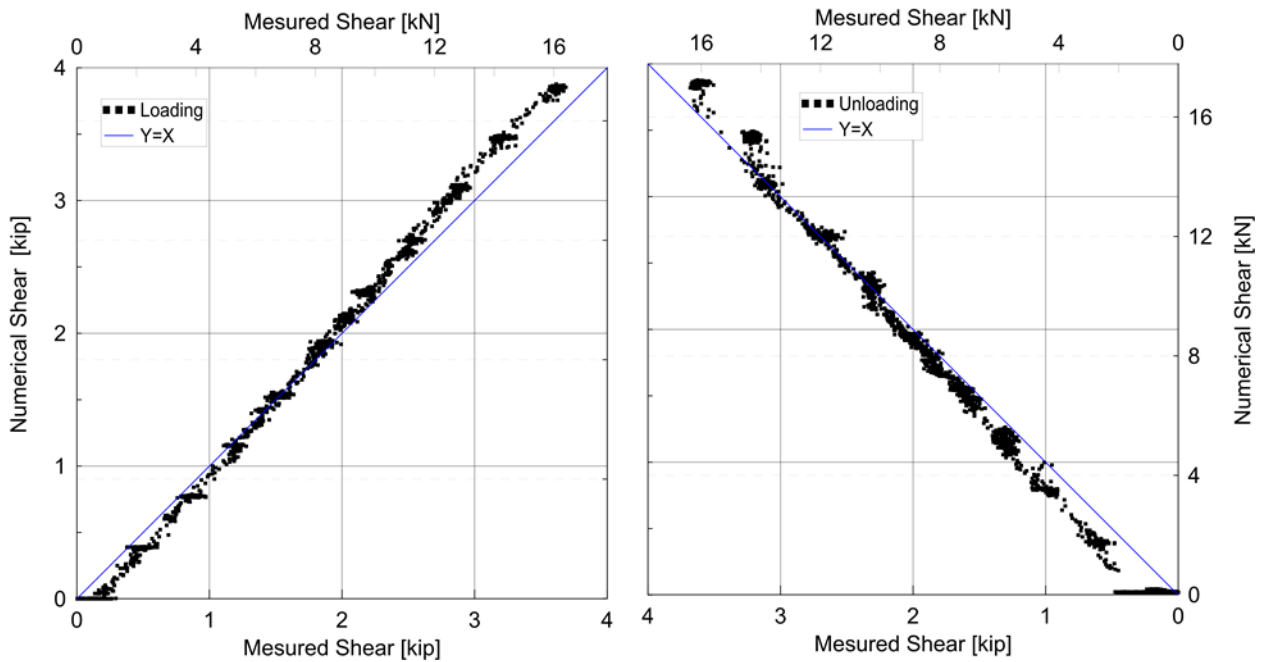


Figure 5-13 Agreement of the numerically generated, and measured shear for loading and unloading cases.

## Chapter 6

### Experimental Results and Data Analysis

#### 6.1. Shaft Testing without Fill Soil

To validate the numerical input parameters and to better calibrate post-test numerical models, small amplitude lateral load testing without fill soil was conducted on specimen SP1. Figure 6-1 shows the test setup of the “no-soil” test. Prior to testing, the specimen’s analytical moment-curvature ( $M-\phi$ ) relationships was blind-predicted using a variety of software tools, including Response2000 (Bentz, 2000), OpenSees (McKenna *et al.*, 2000), and LPILE (Ensoft xxxx). The analytical  $M-\phi$  relationships were estimated using the specified design material strengths, *i.e.*, not the measured or overstrength values. The compressive strength was taken as 33.7 MPa [4.9 ksi], the concrete strain at maximum strength,  $\epsilon_c$  was taken as 0.003, and the confined concrete compressive strength,  $f'_{cc}$  was estimated as 44.13 MPa [6.4 ksi] following Mander *et al.*’s (1988) constitutive model. The reinforcement ultimate stress, yield strength, and yield strain were taken as 517 MPa [75 ksi], 413 MPa [60 ksi], and 0.002, respectively. Figure 6-2 shows a comparison of analytically and experimentally derived moment-curvature data. Lateral displacements were applied through the hydraulic actuator attached to the shaft cap up to approximately 50% of the analytically predicted cracking displacement of the shaft [0.13 cm, 0.05 in]. The corresponding applied lateral load was up to 3.6 kN [0.8 kips]. Only one prediction was performed after concrete compressive testing was completed, which is labeled “post-test OpenSees” in Figure 6-3. This prediction uses a refined estimate of concrete strain at maximum strength using 0.002 instead of 0.003.

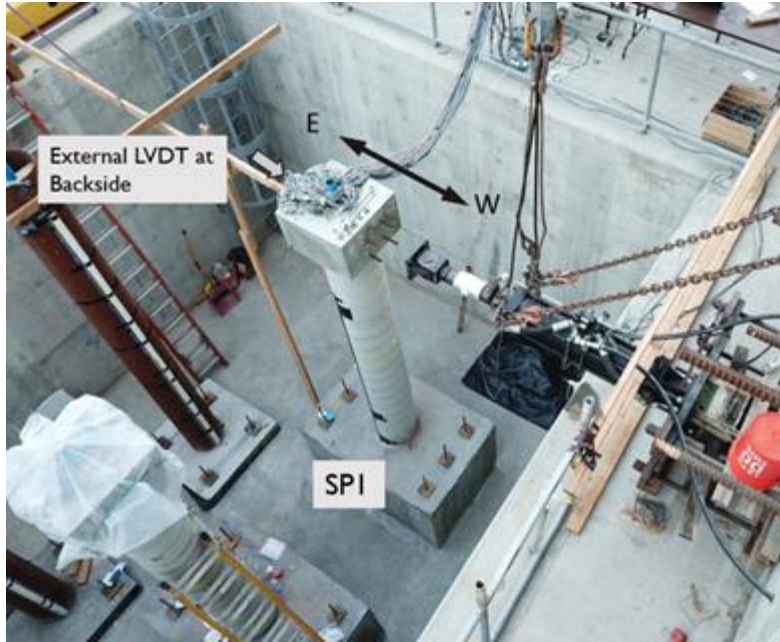


Figure 6-1 Specimen one lateral load test without backfill soil

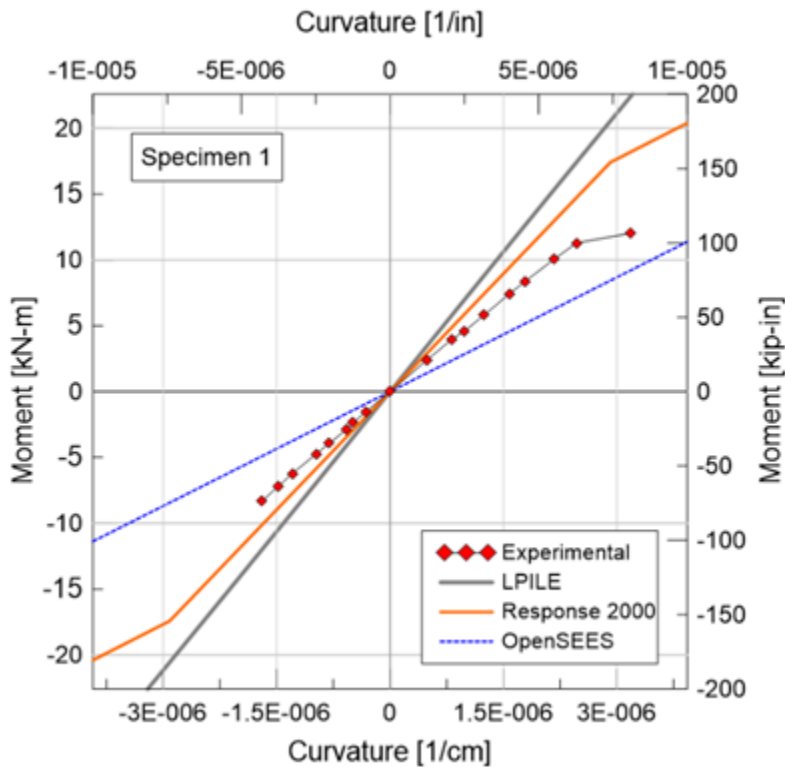


Figure 6-2 Comparison of analytically and experimentally derived moment-curvature data of SP 1 in the linear deformation range

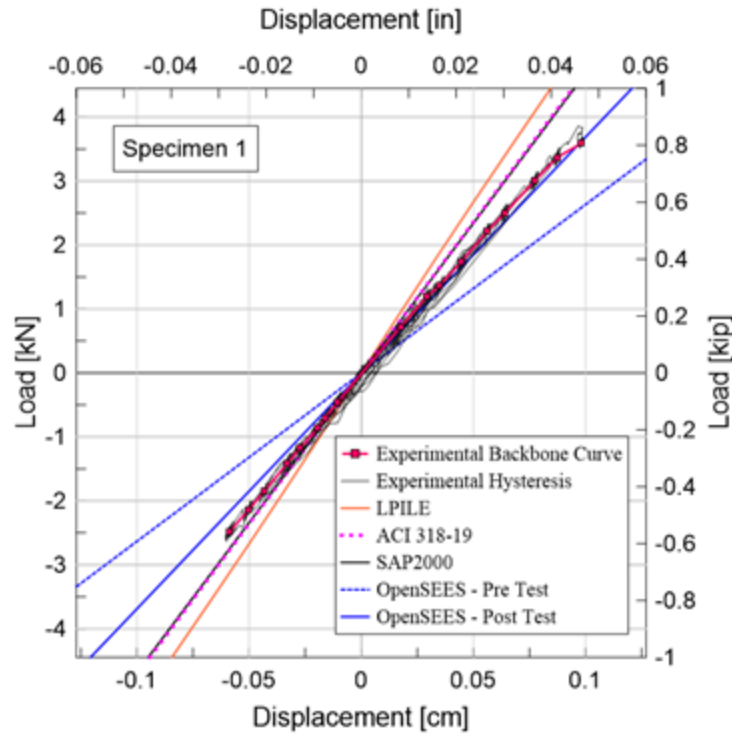


Figure 6-3 Comparison of analytically and experimentally derived load-displacement data of specimen one without backfill soil

## 6.2. Shaft Testing with Fill Soil

Figure 6-4 shows the experimental load-displacement behavior of all specimens with their respective backbone curves. Specimen 1 reached an ultimate load of approximately 72 kN [16.2 kips] at a shaft head displacement of 17.8 cm [7.0 in] in the push direction, and approximately 72 kN [16.2 kips] at a shaft head displacement of 20.0 cm [7.8 in] in the pull direction. Similarly, Specimen 2 reached ultimate resistance at 71 kN [16 kips] and 17.8 cm [7.0 in] in the push direction, and approximately 79 kN [17.8 kips] at a shaft head displacement of 17.8 cm [7.0 in] in the pull direction. Specimen 3 reached an ultimate resistance of 77 kN [17.3 kips] at 20.0 cm [7.8 in] of lateral displacement in the pull direction and exhibited similar behavior in the push direction. All specimens behaved essentially identically up to “concrete cracking”, *i.e.*, up to a displacement level of 0.64 cm [0.25 in] and

a corresponding load of 13.34 kN [3 kips] (about 20% of the ultimate load). The yield displacement was approximately 6.35 cm [2.5 in] at a corresponding load of 8 kips (about 50% of the ultimate load) after which the shafts accumulated substantial permanent deformations for repeated loading cycles. Figure 14 includes a comparison between the experimental and predicted load-displacement curves as well as the applied shaft-head load loads corresponding to predicted failure in flexure (SP1) and shear (SP2 and SP3). The experimental data show that the predicted failure loads have been exceeded by 23%, 53%, and over 100% for SP1, SP2, and SP3, respectively.

The observed damage patterns and nearly identical load versus deformation behavior for the three specimens suggest that all specimens exhibited a flexural failure mechanism. Specifically, the predicted shear failure due to potential shear amplification near the rock-socket interface would have caused a much earlier failure of SP 2 and SP3 at applied shaft head loads of approximately 52 kN [11 kips] and 35 kN [7.8 kips], respectively, which was not observed experimentally. Note that these failure predictions using the  $p$ - $y$  method are based on as-built material properties as presented earlier in the manuscript, not specified nominal material properties. Instead, the shaft specimens SP2 and SP3, which were insufficiently reinforced for the analytically predicted shear amplification, performed identically to the shaft specimen SP1, which was sufficiently reinforced for the shear amplification. SP2 resisted a lateral ultimate load at failure of more than 1.3 times the predicted ultimate capacity based on shear failure and SP3 resisted a lateral ultimate load at failure of more than 2 times the predicted ultimate capacity based on shear failure.



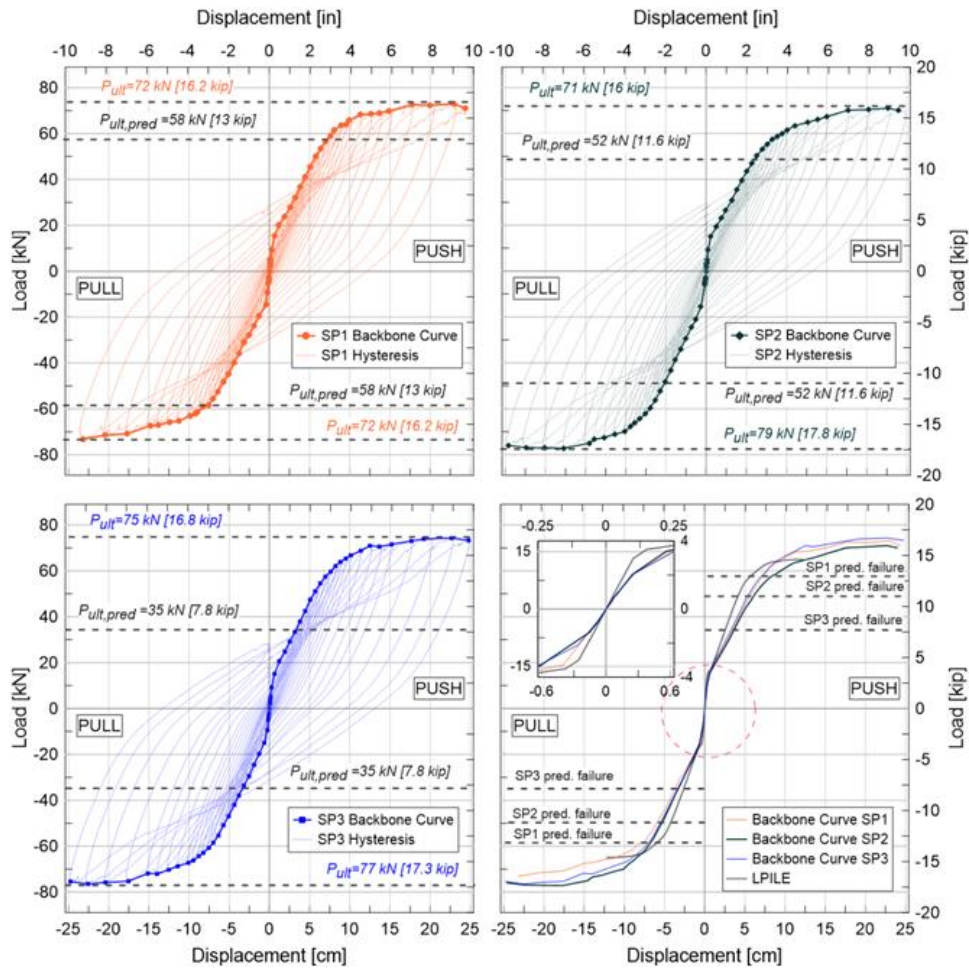


Figure 6-4 Experimental load-displacement relationships with backbone curves

Figure 6-5 shows the lateral deformation profiles recorded through the inclinometer. As expected, measurements indicate that insignificant deformation occurred within the rock socket. Small lateral shaft deformations were noticeable beyond 15 cm [0.5 ft] above the rock socket. Deformed shapes were similar for all specimens in both “pull and push” directions. Curvature profiles (not depicted for brevity) suggest the formation of a plastic hinge within 60 cm [2 ft] above the rock-socket which corresponds to 1.2 m [4 ft] below the ground surface (*i.e.*, about 3 shaft diameters (3D)); which also coincides with the plastic hinge

location) and agrees well with crack patterns observed upon excavation and the maximum moment location shown in Figure 6-6.

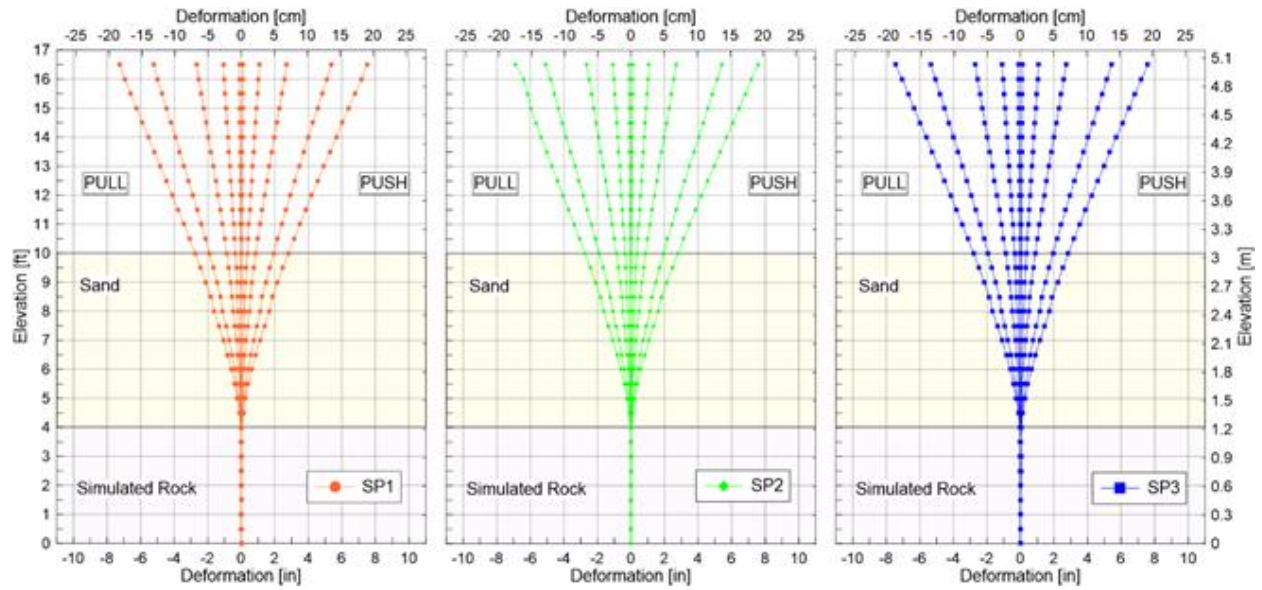


Figure 6-5 Deformed shape of Specimen 1 (left), Specimen 2 (middle) and Specimen 3 (right) at each applied displacement level (inclinometer readings)

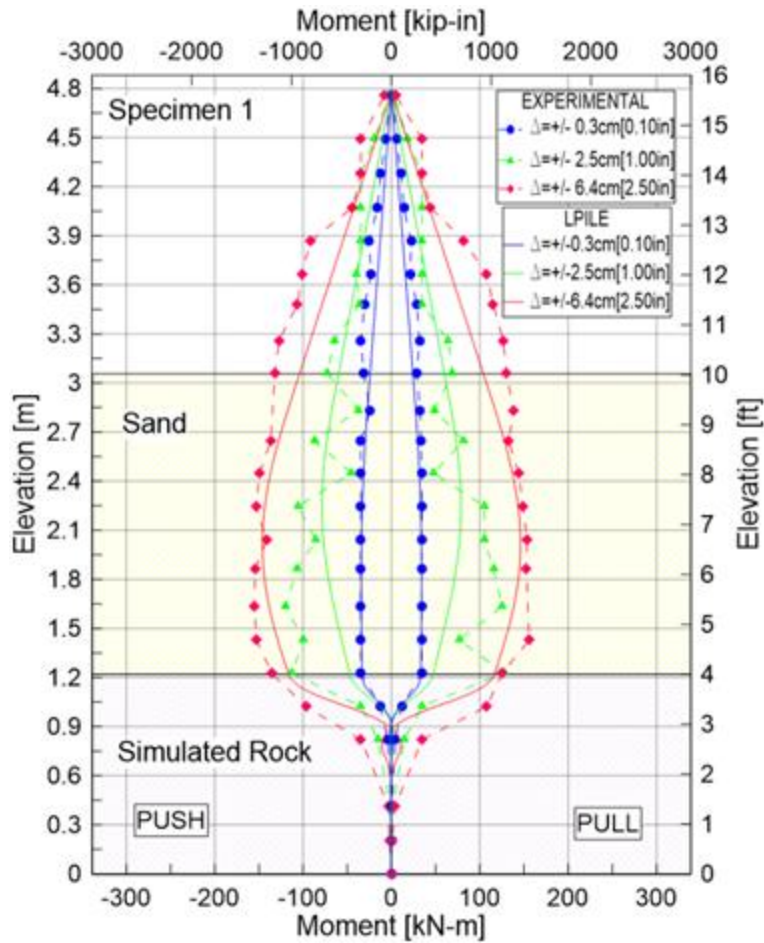


Figure 6-6 Comparison of analytically and experimentally derived moment-profile of specimen one

### 6.3. Post Test Failure Documentation

A spray-painted grid with dimensions of 15 x 15 cm [6 x 6 in] was applied to the sand surface around the shaft specimen to monitor the extents of soil cracking, heaving, and caving as shown in Figure 6-7. An example of the circumferential crack expansion and the formation of “crater-type” holes around the shafts for lateral displacements larger than 10 cm [4 in] is depicted in the photographs of Figure 6-8. Following test completion, each shaft was manually excavated (in push direction) to identify cracking patterns and detect the presence and approximate location of plastic hinge(s) (Figure 6-9). Typical structural failure modes in

a reinforced concrete shaft are classified into two dominant types, flexural failure, or shear failure. Cracks associated with flexural failures start at the tension side of the specimen section and extend to the compression side. These cracks are mostly horizontal and are concentrated at the location(s) of maximum moment. Shear failure occurs when imposed shear stresses are higher than the section shear strength. In the case of shear failure of a rock-socketed drilled shaft, it would be expected that shear cracks would be concentrated at or slightly below the soil-rock interface. Shear cracks are conventionally understood to form at an angle, bending down towards the compression side of the cross section. For all three of the test specimens, the most substantial structural cracking was concentrated within 61 cm [24 in] above the rock socket but also extended to higher elevations at increasingly larger spacing. Almost all cracks formed perpendicular to the shaft axis indicating a flexural mechanism; very few diagonal cracks that would be indicative of shear failure were recorded. No spalling was observed along the shaft circumference. In addition, there were no signs of cracking or damage along the socket surface or within the rock socket itself as shown in Figure 6-9.

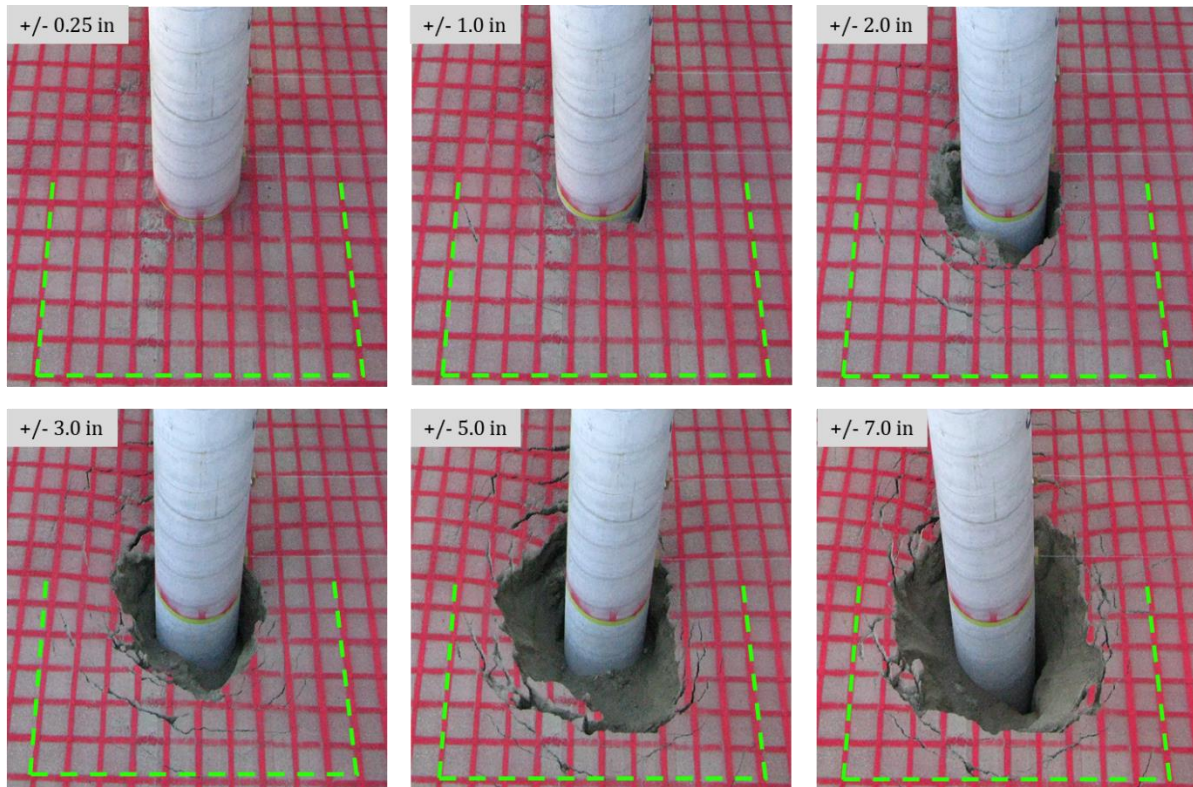


Figure 6-7 Specimen 3 crater formation at different levels of shaft head applied displacement

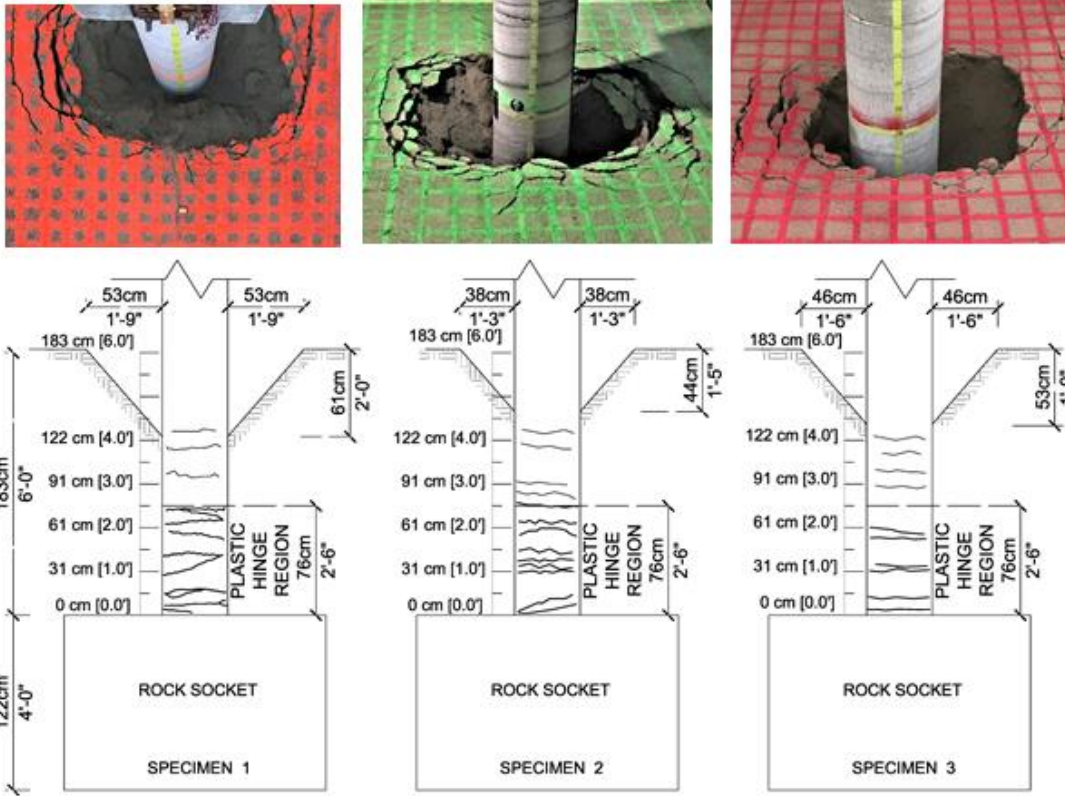


Figure 6-8 Summary of major cracks along the shaft depth and around the surface soil at test completion



Figure 6-9 Crack pattern observation upon excavation of specimens 1 and 3

### 6.3.1. Experimental shear measurements

The embedded tetrahedra were placed at an angle with the shaft global axis (X, Y, Z) as shown in Figure 6-10. Therefore, axis transformation was needed to determine the state of stress with respect to the global axis. Tetrahedra axis were rotated by an angle of  $\theta$  around z-axis. Since the axis z remains unchanged, only two-dimensional rotation matrix shown in equation 6-1 was used.

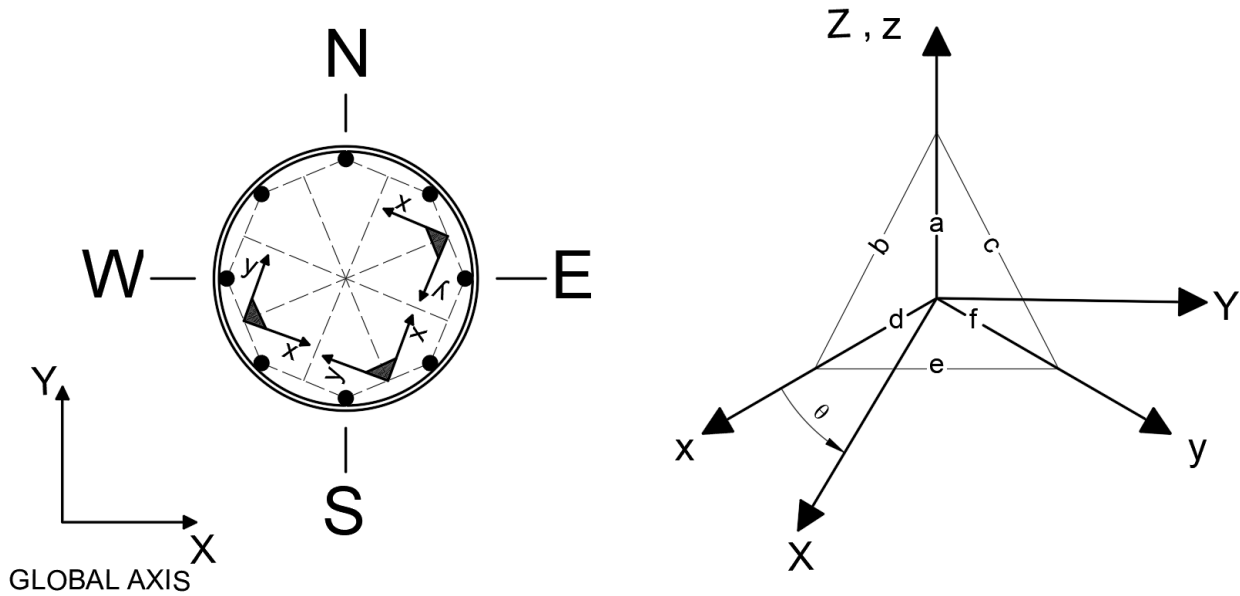


Figure 6-10 Global axis versus the tetrahedron local axis

For rotation angles around z-axis at counterclockwise direction the following rotation matrix could be obtained:

$$R = \begin{bmatrix} \cos\theta & \sin\theta & 0 \\ -\sin\theta & \cos\theta & 0 \\ 0 & 0 & 1 \end{bmatrix} \quad (6-1)$$

The transformed stresses can then be determined by:

$$\begin{bmatrix} \sigma_X & \tau_{XY} & \tau_{XZ} \\ \tau_{YX} & \sigma_Y & \tau_{YZ} \\ \tau_{ZX} & \tau_{ZY} & \sigma_Z \end{bmatrix}_{GLOBAL} = \begin{bmatrix} \cos\theta & \sin\theta & 0 \\ -\sin\theta & \cos\theta & 0 \\ 0 & 0 & 1 \end{bmatrix} \begin{bmatrix} \sigma_x & \tau_{xy} & \tau_{xz} \\ \tau_{yx} & \sigma_y & \tau_{yz} \\ \tau_{zx} & \tau_{zy} & \sigma_z \end{bmatrix}_{LOCAL} \begin{bmatrix} \cos\theta & \sin\theta & 0 \\ -\sin\theta & \cos\theta & 0 \\ 0 & 0 & 1 \end{bmatrix}^T \quad (6-2)$$



Shear stress and force of a circular cross section could be obtained as illustrated in Figure 6-11 and equations 6-3 to 6-8.

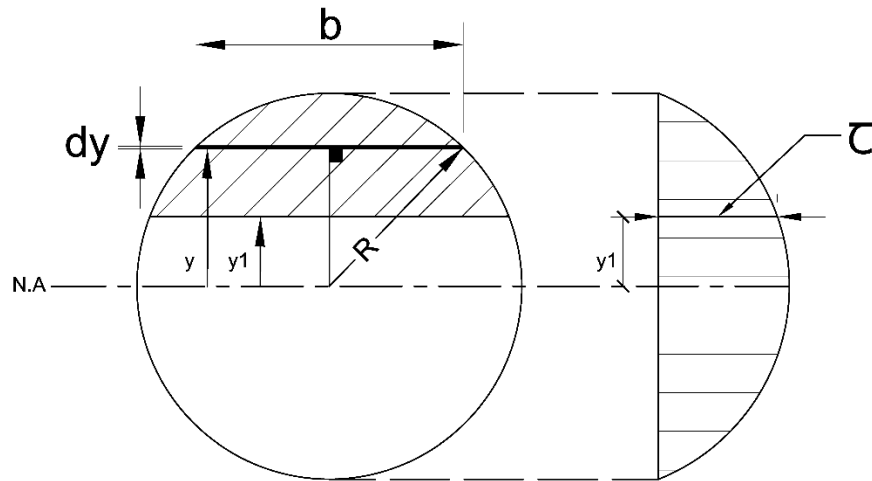


Figure 6-11 Shear distribution of circular cross section

$$\text{Shear stresses at any arbitrary section is } \tau_{y1} = \frac{VQ}{Ib} \quad (6-3)$$

Where:

V = transverse shear force

Q = first moment of area (section above area of interest)

I = moment of inertia

b = width of section

$$\text{The width (b) as a function of y is } b = 2\sqrt{R^2 - y^2} \quad (6-4)$$

First moment of area of the shaded area shown in Figure 6-11 around the neutral axis is obtained by integrating the area of the section above the area of interest since the width (b) of the cross section is a function of y as following:

$$Q = \int_{y1}^R dA \cdot y = \int_{y1}^R dy \cdot b \cdot y = \int_{y1}^R dy \cdot 2\sqrt{R^2 - y^2} \cdot y = \frac{2}{3}(R^2 - y1^2)^{3/2} \quad (6-5)$$

Moment of inertia of a circular section is  $I_{N.A} = \frac{\pi R^4}{4}$  (6-6)

Hence,

$$\tau_{y1} = \frac{VQ}{Ib} = \frac{V \cdot \frac{2}{3}(R^2 - y1^2)^{3/2}}{\frac{\pi R^4}{4} \cdot b} = \frac{4V \cdot (R^2 - y1^2)}{3\pi R^4} \quad (6-7)$$

The shear force (V) that the section is experiencing could be estimated in terms of the shear stresses ( $\tau_{y1}$ ) assuming that the distribution of shear stresses is uniform across the width of the cross section as following:

$$V = \frac{3\pi R^4 \cdot \tau_{y1}}{4(R^2 - y1^2)} \quad (6-8)$$

The tetrahedral measured strains were transformed into stress then rotated to the shaft global axis. The global shear stress was then integrated into shear forces. Figure 6-12 shows the tetrahedra measured data at 6 inches below the soil-rock interface (location of maximum predicted shear). The measured shear profile was also compared to the LPILE (p-y method) generated shear forces as shown in Figure 6-13. The measured data suggests that the predicted amplified shear by p-y method at applied lateral displacement of 0.25 in is 5 times the measured shear forces.

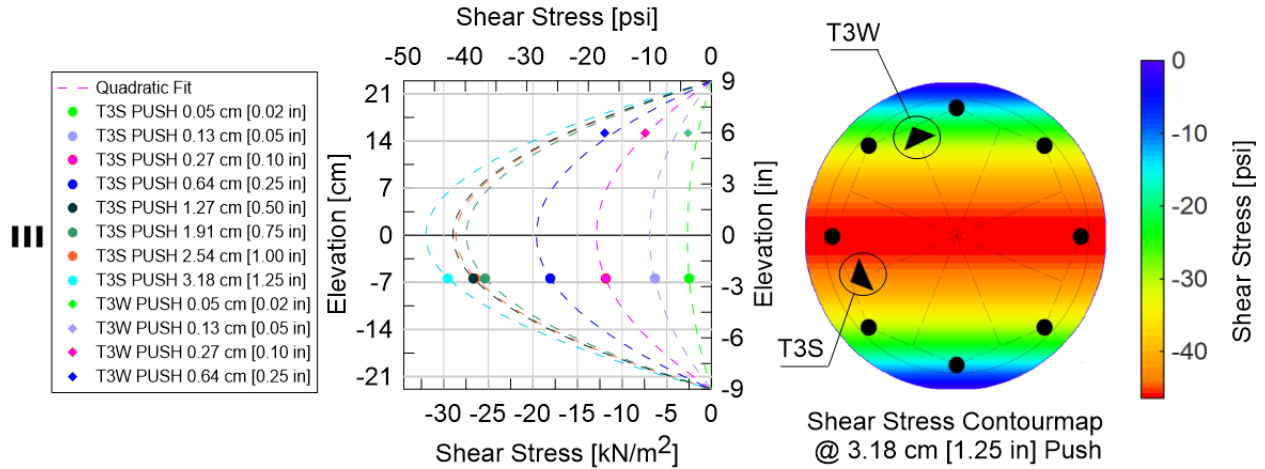


Figure 6-12 Tetrahedra located at the maximum shear inside the rock-socket of Specimen 2 measured data.

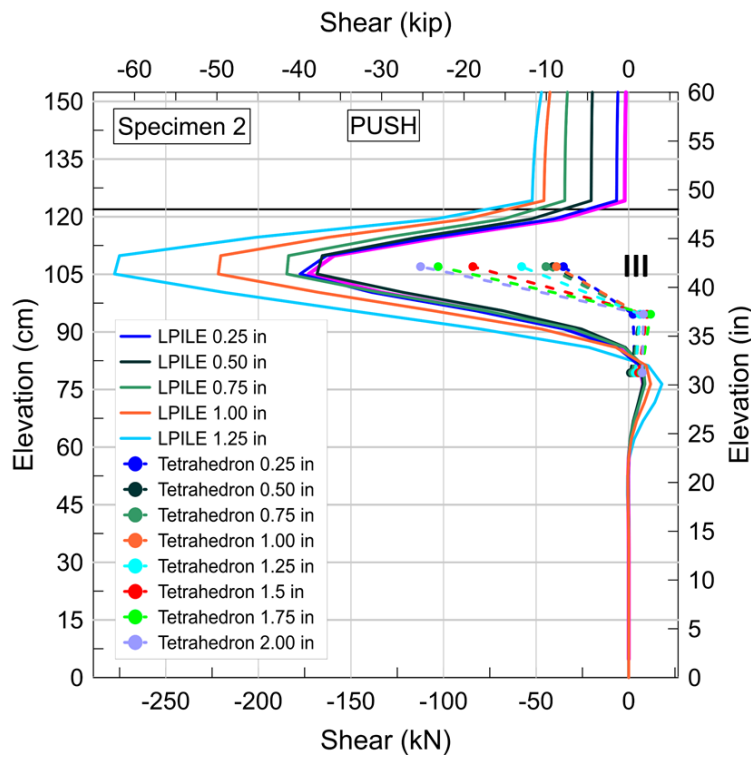


Figure 6-13 Measured shear profile versus the LPILE generated shear profile inside the rock socket

#### 6.4. Results from retest of failed specimens

Phase 2 load-displacement responses of Specimens 2 and 3 are compared to their initial test responses (Phase 1) in Figures 6-10 and 6-11. The backbone curve of Specimen 2 suggests that the retested shaft specimen was able to reestablish the same initial shaft-soil system stiffness. After adding the soil fill, Specimen 2's lateral load capacity increased by approximately 80% in both, pull and push directions. The retested Specimen 2 also showed higher ductility in comparison to its initial testing (Phase 1). On the other hand, Specimen 3 was able to restore about 60% of its initial shaft-soil stiffness. The retested Specimen 3 also showed higher ductility in comparison to the initial testing. This reduced initial stiffness during Phase 2 testing is a result of Specimen 3 having minimal transverse reinforcement, and therefore, the residual stiffness after the initial testing was lower than that of Specimen 2. The Specimen 3 lateral load capacity was increased by about 70% on average for pull and push directions.

The magnitude of plastic deformations ( $\Delta$  plastic) for a certain cycle can be calculated as the difference in displacement at zero shaft head load (e.g., intersection of the load deformation curve with x-axis) as shown in Figure 6-10. Figure 6-10 also shows the accumulated plastic deformations for a lateral shaft head displacement of 10 cm [4 in ] during Phase 1 and Phase 2 testing of Specimens 2 and 3. Both retested specimens had a 100% increase in their plastic deformation. The increase in plastic deformation can be explained by a new plastic hinge being developed as an extension to the preexisting plastic hinge from Test 1. Also, the higher plastic deformations experienced in the retested shafts contributes to the stiffness recovery when cracks are closed during displacements imposed in the other direction, which ultimately contributes to the increase in the observed lateral load capacity. It was also noted that the stiffness of the retested shafts degraded at a slower rate than that of the initial test

(Phase 1). The energy dissipation during each cycle can be calculated from the enclosed area within the hysteresis loop as illustrated in Figure 6-10. The energy dissipation of the retested shafts was approximately double the energy dissipated during Phase 1 testing. Shaft deformation profiles at selected shaft head displacement levels are shown in Figure 6-11. The deformation profiles were recorded with inclinometer instrumentation and recorded during Phase 1 and Phase 2 testing. A comparison of Specimen 2's deformed shapes indicates that the plastic hinge has shifted and extended to a higher elevation by about 0.45 m [1.5 ft].

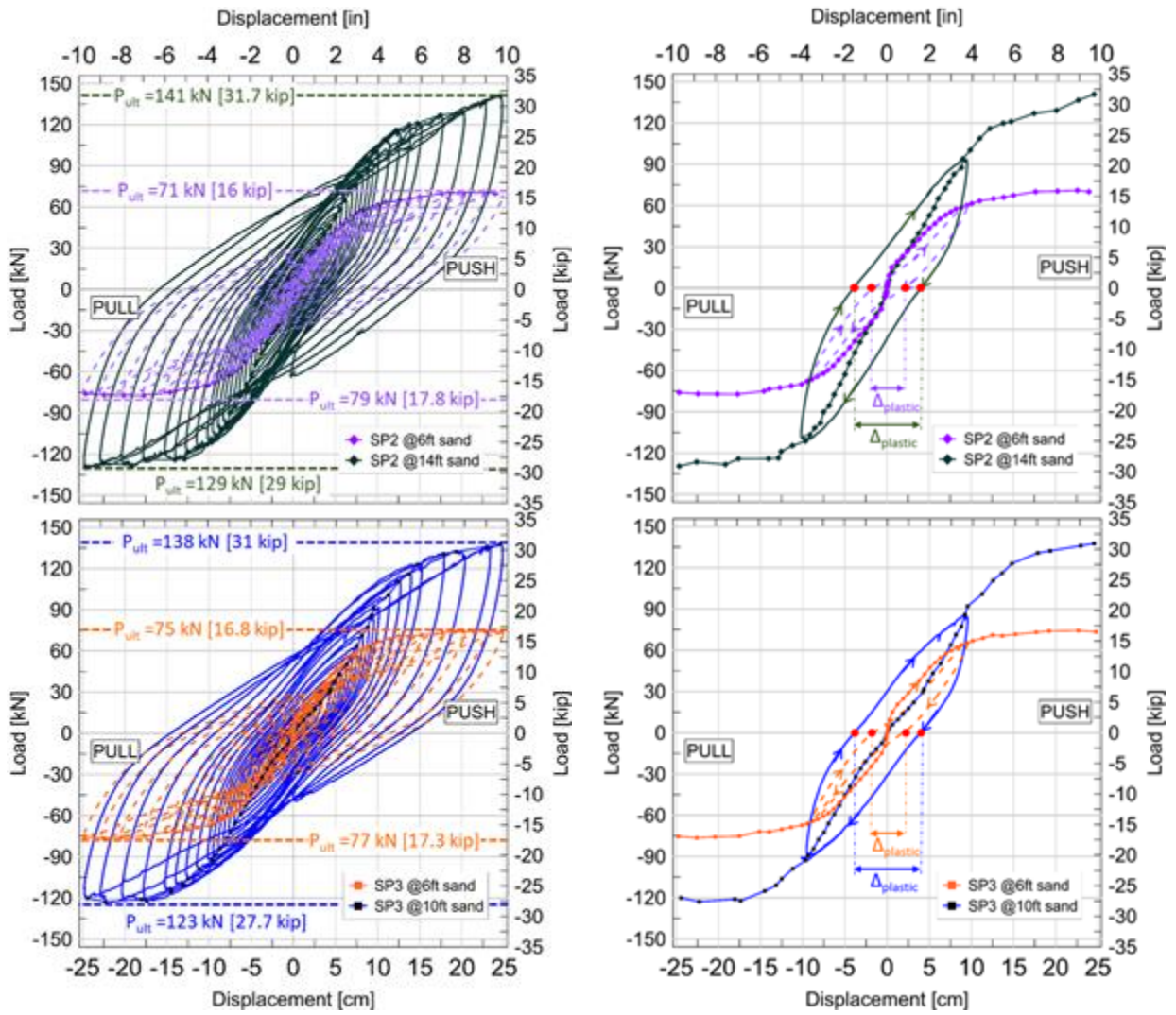


Figure 6-14 Load-displacement relationship of specimen 2 and 3 before and after retesting

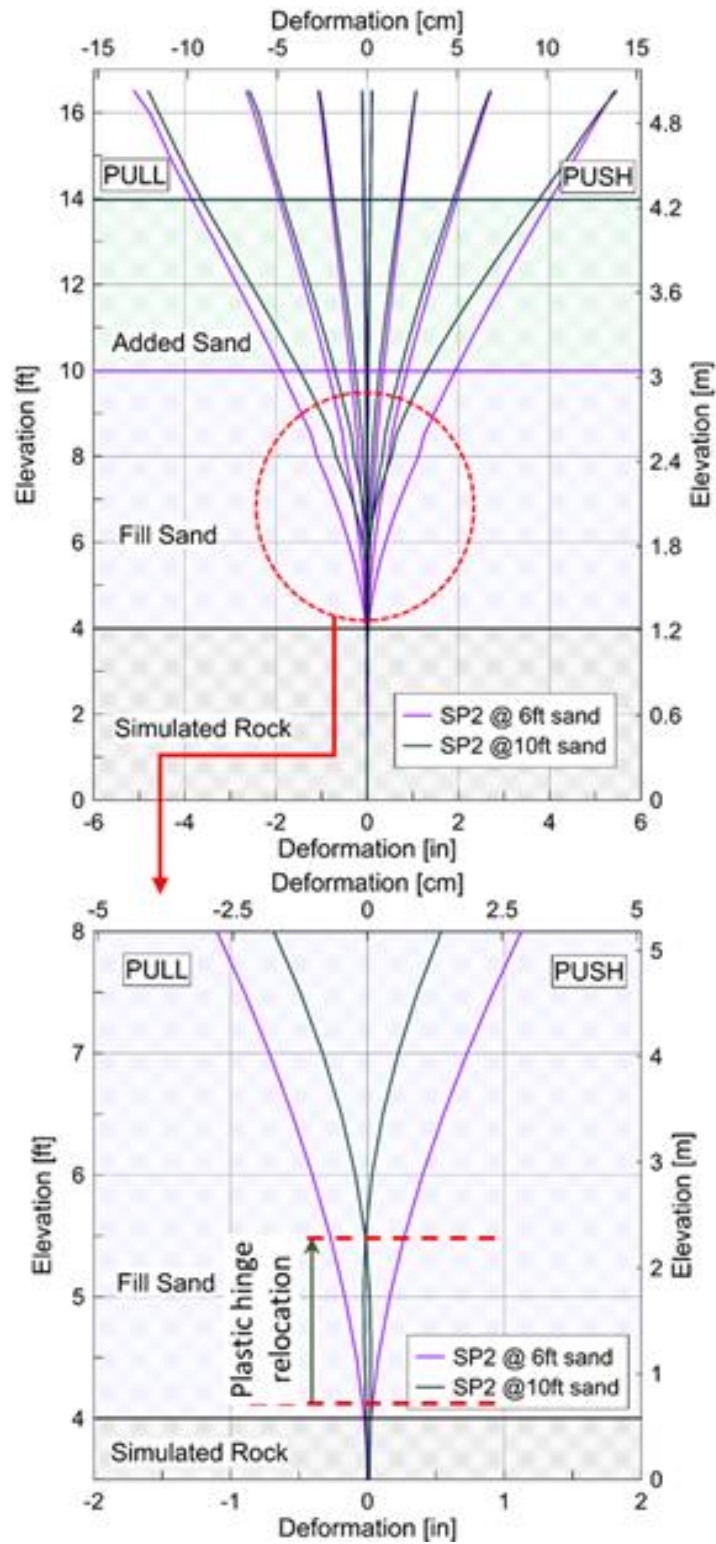


Figure 6-15 Specimen 2 deformed shapes before and after adding sand and retesting

## **6.5. Conclusion**

### **6.5.1. Testing of the shaft specimens**

Three shaft specimens with different transverse shear reinforcement ratios were examined under identical test conditions and subjected to reverse cyclic lateral loading. The specimens were installed in a two-layer stratigraphy with a strong stiffness contrast consisting of loose sand underlain by rock, experimentally simulated by high-strength concrete. Specimens were loaded to complete structural failure and examined after test completion and the results were presented in this chapter. No damage (*i.e.*, cracking) and no significant lateral shaft deformations were observed inside the rock socket. Predominantly flexural cracking occurred along the shafts within 60 cm [2 ft] above the rock socket. This elevation corresponds to a depth of three shaft diameters below ground surface, which is a typical location of plastic hinges of flexible shafts. The differently reinforced shaft specimens would be expected to fail in different failure modes according to their transverse reinforcement ratios and the predicted shear amplification using the  $p$ - $y$  method. The experimental specimen behavior showed that the analytically predicted shear dominated failure did not occur. These preliminary observations could be of future benefit to the construction industry as bulky transverse reinforcement could be minimized and potential issues such as restrictions of concrete flow resulting in defective concrete due to closely spaced transverse reinforcement could be reduced.

### **6.5.2. Retesting of the shaft specimens**

Following initial testing of Specimens 2 and 3 to complete structural failure, the soil stratigraphy was modified by raising the surcharge materials to strategically shift the



initially developed plastic hinge to a higher elevation and to provide additional confinement around the shaft specimens during retesting. The retesting experimental results suggested that adding a 1.2 m [4ft ] thick soil layer was able to recover the initial stiffness of the failed shafts by 100% for Specimen 2 and by 60% for Specimen 3. The lateral reinforcement ratio substantially influenced the shaft ability to restore the initial shaft stiffness but had less contribution to recovering the ultimate shaft capacity. The proposed increase of the soil stratigraphy raised the ultimate shaft capacity of Specimens 2 and 3 by 80% and 70%, respectively. The ductility and energy dissipation of the retested shafts improved greatly as a result of extending/relocating the pre-existing plastic hinge rather than introducing repairs to the plastic hinge region. Despite the different transverse reinforcement ratios, Specimens 2 and 3 reached the same level of ductility during Phase 2 testing, which can be attributed to the confinement provided by the increase in sand surcharge. Findings of this experimental study suggest that modifications to the soil stratigraphy around the shaft upon partial or full loss of structural shaft integrity could provide a temporary solution for post-earthquake retrofit and temporary increase or recovery of shaft-soil capacity.

## Chapter 7

### **3D Numerical Analyses of Shear Demand Within the Rock-Socket of Drilled Shafts Subject to Lateral Loading**

#### **7.1. Introduction**

Finite element analysis is a powerful technique to understand and support complex engineering problems. The aim of this numerical study was to investigate and improve the existing procedures for the estimation of rock-socketed drilled shaft shear demands and introduce in-depth shaft-rock system load-transfer mechanism analysis. In this chapter, a numerical model was constructed and calibrated to the experimental program presented in Chapter 3. Since the presented study represents an interaction of stiff rock and a flexible shaft, an emphasis is put on the behavior of the “drilled shaft” structure rather than the surrounding rock. Elastoplastic and nonlinear based models were assigned to the elements that were expected to reach plasticity or behave nonlinearly. The soil-structure interaction was simulated by introducing a virtual interface element that resembled the interface properties. The constructed numerical model then underwent a calibration process to replicate the experimental response. Finally, the calibrated model was further used to investigate cases of interest that were not tested experimentally. Also, the influence of selected constitutive model input parameters were studied in a sensitivity analysis.

#### **7.2. Numerical simulation**

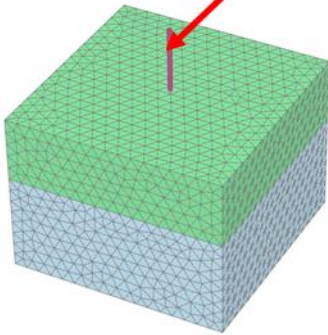
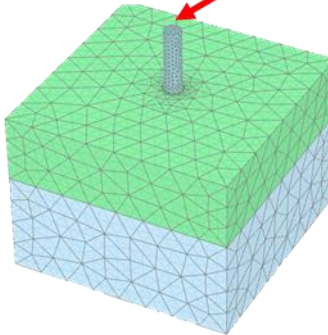
Finite element method of analysis has been used to simulate complex geotechnical and structural problems for decades. In this study, the finite element analysis was conducted using the commercially software PLAXIS 3D. The program is well known for its capability to model subsurface behavior and soil-structure interaction. However, its ability to implement a detailed representation of the reinforcement and the non-linear behavior of concrete is not explicitly defined. Modelling practices and recommendations were developed and introduced in this study to accurately simulate the reinforced concrete shaft behavior.

### **7.3. Modeling reinforced concrete drilled shafts**

Two general ways to model concrete exist; either as a linear elastic material or as a non-linear elastoplastic material. If concrete was to be modeled linearly, the state of stresses must not exceed the linear portion of its stress-strain relationship. Also, the small deformation influence on the soil-shaft system should be minimal in order to eliminate the inaccuracies introduced by assuming the concrete behavior to be linear. The shaft-soil system in this study involved rock-shaft interaction that underwent small deformation and higher stresses. Therefore, using a linear concrete model was not an option. In PLAXIS, reinforced concrete structures are typically modeled with the use of plate elements or embedded beams. These plate elements and embedded beams are then assigned a linear elastic or elastoplastic material behavior model in the two- and three-dimensional modeling. The two-material models do not take into consideration the non-linear behavior of concrete and stiffness degradation due to cracking. Only in two-dimensional modeling can the plate elements be given a pre-defined moment curvature relationship that could take into consideration the non-linear behavior of the concrete. However, shaft-soil interaction under lateral loading is

a three-dimensional problem and simplifying it into a two-dimensional problem especially while investigating small deformations would not resemble the shaft behavior accurately. Preliminary models were developed to distinguish the capabilities and limitations of each element. Table 7-1 shows the benefit of using a volume element over an embedded beam element for the simulation. In order to gain more insight into the cracking process and to incorporate the non-linear behavior of concrete, a volume element was used rather than the embedded 3D beam element or plate element.

Table 7-1 Embedded beam element versus volume element to simulate the reinforced concrete shaft in PLAXIS

3D embedded beam element	Volume element
<ul style="list-style-type: none"> <li>➤ Elastic one shaft diameter zone</li> <li>➤ Linear elastic Skin Interface</li> <li>➤ Shaft foot assigned bearing capacity</li> <li>➤ Shaft-soil interaction is modeled at the center rather than at the circumference</li> </ul>	<ul style="list-style-type: none"> <li>➤ Shaft can be assigned non-linear material model</li> <li>➤ Interface can be assigned specific material model</li> <li>➤ Shaft foot stresses</li> <li>➤ Shaft-soil interaction is modeled at the circumference</li> </ul>
<p style="text-align: center;">Embedded beam</p> 	<p style="text-align: center;">Volume pile</p> 

The volume element could be given the Mohr-Coulomb model, which does not take into consideration the non-linear behavior of the concrete or shotcrete model. The theoretical formulation of the shotcrete model is given in Schädlich & Schweiger (2014). The shotcrete model allows non-linearity and stiffness degradation to be taken into consideration, which improves the accuracy of modeling concrete behavior. The shotcrete model is an advanced elastoplastic model for concrete structures in which the failure criterion involves a Mohr-Coulomb yield surface for deviatoric loading and Rankine yield surfaces in the tensile regime. Although the shotcrete model was developed initially to describe the behavior of the sprayed concrete in tunnel lining applications, it was proven to be applicable for other concrete modelling cases (Witasse, 2016). The shotcrete model stress-strain curve in compression is described by four phases as shown in Figure 7-1:

- Part I -quadratic strain hardening
- Part II – linear strain softening
- Part III – linear strain softening
- Part IV – constant residual strength

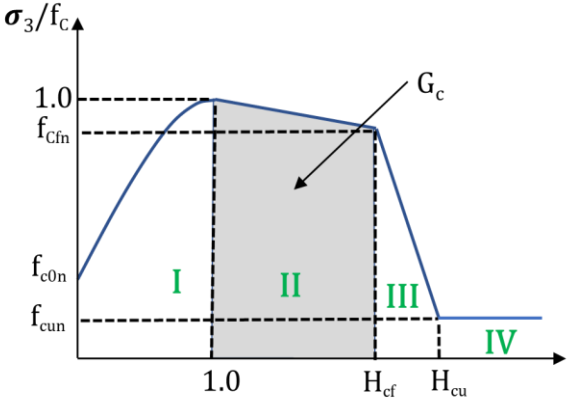


Figure 7-1 Normalized stress-strain curve in compression (Reproduced after Schutz et al. 2011)

More details about the constitutive model are found in Schutz et al. (2011). Table 7-2 shows an overview of the input parameters for the shotcrete model. The time dependent parameters in the model were eliminated since this study deals with mature/hardened concrete under static loading. The concrete model behavior in tension is linear elastic until the tensile strength  $f_t$  is reached, and thereafter softens with linear strain softening.

Table 7-2 Model parameters

Parameter	Description
$E_{28}$	Young's modulus of cured shotcrete
$\nu$	Poisson's ratio
$f_{c,28}$	Uniaxial compressive strength of cured shotcrete
$f_{t,28}$	Uniaxial tensile strength of cured shotcrete
$\psi$	Dilatancy angle
$f_{c0n}$	Normalized initially mobilized strength
$f_{cfn}$	Normalized failure strength (compression)
$\epsilon_{p_{cp}}$	Uniaxial plastic failure strain
$G_{c,28}$	Compressive fracture energy of cured shotcrete
$f_{tun}$	Ratio of residual vs. peak tensile strength
$G_{t,28}$	Tensile fracture energy of cured shotcrete
$a$	Increase of $\epsilon_{p_{cp}}$ with increase of the confining stresses
$\phi_{max}$	Maximum friction angle
$\gamma_{fc}$	Safety factor for compressive strength
$\gamma_{ft}$	Safety factor for tensile strength

Results from uniaxial compression testing of the shafts' concrete cylinders were used to calibrate the concrete model input parameters. The stress-strain curves of the tested unconfined uniaxial concrete cylinders data was used directly to optimize the shotcrete

model under unconfined condition (Lateral stresses are set to zero). On the other hand, in order to calibrate the shotcrete model when confining stresses are present, Mender et al. (1988) theoretical model for confined concrete was used. Mander model of unconfined concrete was needed since the confined concrete uniaxial compression experimental data was not available. The Mender theoretical model for confined concrete was predicted based on the unconfined uniaxial cylinder data. The theoretical model then was used to calibrate the shotcrete confined model. Figure 7-2 shows the performance of the calibrated unconfined/confined concrete model versus the theoretical model and the uniaxial unconfined stress-strain curves of the tested concrete cylinders. Table 7-2 shows the input parameter values for the optimized concrete model.

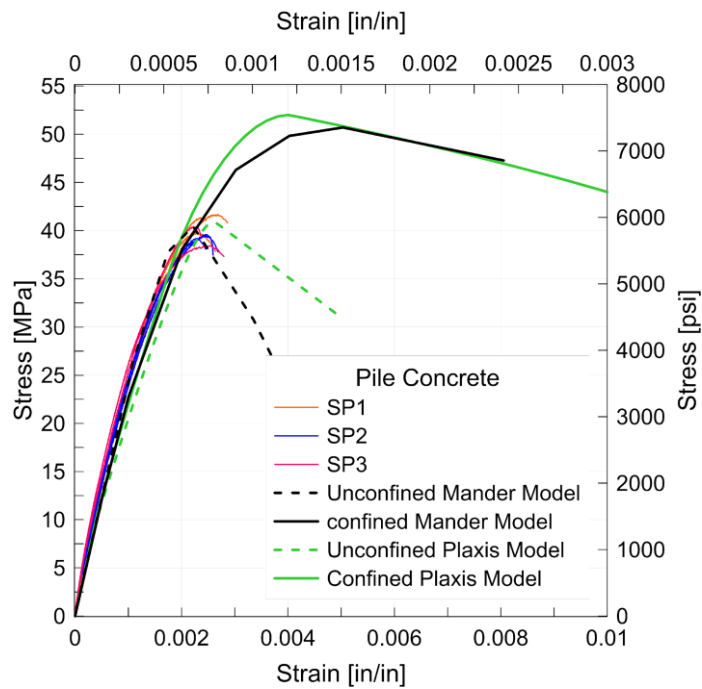


Figure 7-2 Concrete model performance versus tested uniaxial concrete cylinders

Table 7-2 Proposed values for concrete modelling based on the parametric optimization and the stress-strain curve of the tested uniaxial concrete cylinders

Parameter	Description	Value
$E_{28}$	Young's modulus of cured shotcrete	25476 MPa [3695 ksi]
$\nu$	Poisson's ratio	0.15
$f_{c,28}$	Uniaxial compressive strength of cured shotcrete	40.4 MPa [5.865 ksi]
$f_{t,28}$	Uniaxial tensile strength of cured shotcrete	4.0 MPa [.58 ksi]
$\psi$	Dilatancy angle	15
$f_{c0n}$	Normalized initially mobilized strength	0.2243
$f_{cfn}$	Normalized failure strength (compression)	0.01
$\epsilon_{p_{cp}}$	Uniaxial plastic failure strain	0.001
$G_{c,28}$	Compressive fracture energy of cured shotcrete	69.14 kN/m [0.3948 kip/in]
$f_{tun}$	Ratio of residual vs. peak tensile strength	0.15
$G_{t,28}$	Tensile fracture energy of cured shotcrete	0.0099 kN/m [0.000057 kip/in]
$a$	Increase of $\epsilon_{p_{cp}}$ with increase of the confining stresses	18



$\phi_{max}$	Maximum friction angle	45 deg
$\gamma_{fc}$	Safety factor for compressive strength	1
$\gamma_{ft}$	Safety factor for tensile strength	1

---

Detailed reinforcement cannot be modeled in the concrete volume element model. Therefore, it was modeled by giving the characteristics of the reinforcement to a beam element. The beam element was assigned a linearly elastic- perfectly plastic material model. The steel reinforcement was assumed to behave linearly up to yield strength and then perfectly plastic thereafter. The Young's modulus of the steel reinforcement was taken as 29000 ksi and the yield strength was taken as 60 ksi.

#### **7.4. Modeling the simulated rock**

Rock was simulated experimentally with high strength concrete. The simulated rock was assigned a concrete material model in PLAXIS. The concrete model was calibrated to the uniaxial compression testing of the concrete cylinders collected at the time of the socket concrete pouring and tested at the day of the shaft lateral testing. Parameter optimization was carried out in a similar manner to the optimization for shaft concrete model parameters mentioned in Section 1.2.1. Table 7-3 shows the input parameter values for the optimized concrete model used to simulate the rock-socket concrete.

Table 7-3 Proposed values for socket concrete modeling based on the parametric optimization and the stress-strain curve of the tested uniaxial concrete cylinders

Parameter	Description	Value
$E_{28}$	Young's modulus of cured shotcrete	25455 MPa [3692 ksi]
$\nu$	Poisson's ratio	0.15
$f_{c,28}$	Uniaxial compressive strength of cured shotcrete	47.16 MPa [6.84 ksi]
$f_{t,28}$	Uniaxial tensile strength of cured shotcrete	4.7 MPa [0.68 ksi]
$\psi$	Dilatancy angle	15
$f_{c0n}$	Normalized initially mobilized strength	0.2224
$f_{cfn}$	Normalized failure strength (compression)	0.01
$\epsilon_{p_{cp}}$	Uniaxial plastic failure strain	0.001
$G_{c,28}$	Compressive fracture energy of cured shotcrete	68.84 kN/m [0.3931 kip/in]
$f_{tun}$	Ratio of residual vs. peak tensile strength	0.15
$G_{t,28}$	Tensile fracture energy of cured shotcrete	0.0099 kN/m [0.000057 kip/in]
$a$	Increase of $\epsilon_{p_{cp}}$ with increase of the confining stresses	17.8
$\phi_{max}$	Maximum friction angle	45 deg
$\gamma_{fc}$	Safety factor for compressive strength	1

## 7.5. Modeling the sand

Numerous constitutive models have been developed and implemented in PLAXIS that can capture small strain and large strain soil behavior. The more complex the constitutive model is, the more it requires detailed input parameters. Collecting reliable field measurements is a challenging task and involves much judgment. In this study, extensive field testing and laboratory testing were performed to evaluate the sand layer performance in the field. The sand layer was pluviated uniformly and a moderately low relative density of only 25% was obtained. Because the sand layer was kept relatively loose and its influence on the shaft behavior was not significant, the Mohr-Coulomb constitutive model was appropriate to be adopted for this study. In contrast, the shaft behavior is mainly influenced by the shaft-rock interaction and the structural performance of the shaft. The sand friction angle ( $\phi$ ) and stiffness (E) were evaluated based on direct shear testing, cone penetration testing (CPT) correlations, and flat dilatometer testing (DMT) correlations. Since sand is highly nonlinear material, with both strength and stiffness contingent on stress and strain levels, the field data collected using different means of testing and correlations varied as discussed in Chapter 3. Table 7-4 shows a summary of the sand layer parameters found through field and laboratory testing. In order to accurately calibrate the soil model, an inverse analysis technique was followed. Initial pilot numerical models were developed, and the sand input parameters were optimized to minimize the difference between the experimental shaft response and the numerically computed response.

Table 7-4 Field and laboratory testing collected data summery

Parameter	Method	Value
Friction angle ( $\phi$ )	Direct shear	38.4 deg
	CPT correlation by Robertson and Campanella (1983)	39.3 deg
	CPT correlation by Kulhawy and Mayne (1990)	34.1 deg
	DMT correlation by Marchetti (1997)	34.9 deg
Young's Modulus (E)	CPT correlation by Robertson, PK (2009)	7.44 Mpa [1.08 ksi]
	CPT - Hooke's Law using $V_{s(CPT)}$	24.6 Mpa [3.57 ksi]
	DMT correlation by Marchetti (1997)	2.4 Mpa [0.35 ksi]
	SCPT- Hooke's Law using $V_{s(SCPT)}$	186 Mpa [27 ksi]
Shear wave velocity ( $V_s$ )	CPT correlation by Robertson, PK (2009)	80 m/s [262.5 ft/s]
	SCPT	220 m/s [721.8 ft/m]

## 7.6. Modeling soil-structure interface

Simulating the interaction between a structure and soil can be done by either assuming the structure and the soil are fixed together, and therefore no relative displacement is allowed, or by introducing an interface element between the soil and the structure. By using an interface element, node pairs are created at the interface of the structure and the soil, with one node belonging to the structure and the other node belonging to the soil. These interface elements in PLAXIS are given a virtual thickness and use a strength/stiffness reduction factor ( $R_{inter}$ ), which is applied to the soil adjacent to the interface. The strength/stiffness parameters are by default taken from the material set of the adjacent soil cluster. However, the parameters could be appointed directly from a material set that allows for direct control of the strength properties without changing the properties of the soil cluster. In this study, the reduction factor ( $R_{inter}$ ) method was used to create the interface between the shaft and the sand. The interface between the shaft and the simulated rock was directly assigned a material data set to allow control over the input parameters without changing the properties of the shaft or the simulated rock.

### **7.7. Finite element mesh and boundary condition**

The three-dimensional model consisted of volume continuums, embedded beams elements, and interface elements. The shaft, sand, and simulated rock were assigned soil continuum elements, and soil continuum elements were meshed into 10-node tetrahedral elements. Three-node line elements were assigned to the embedded beams, which are compatible with the 3-node edges of the soil element. The soil-structure interface was composed of 12-node elements, with each element consisting of pairs of nodes (pair of 6-node elements), and compatible with the 6-node triangular side of the 10-node volumetric tetrahedron element.

Although interface elements are given a finite thickness in the model, in the finite element formulation the coordinates of each node pair are identical, confirming that the distance between the two nodes of a node pair is zero. Each node has three translational degrees of freedom, which allows differential displacement between the node pairs (slipping and gapping). Figure 7-3 shows schematically the elements considered in the finite element simulation of this study.

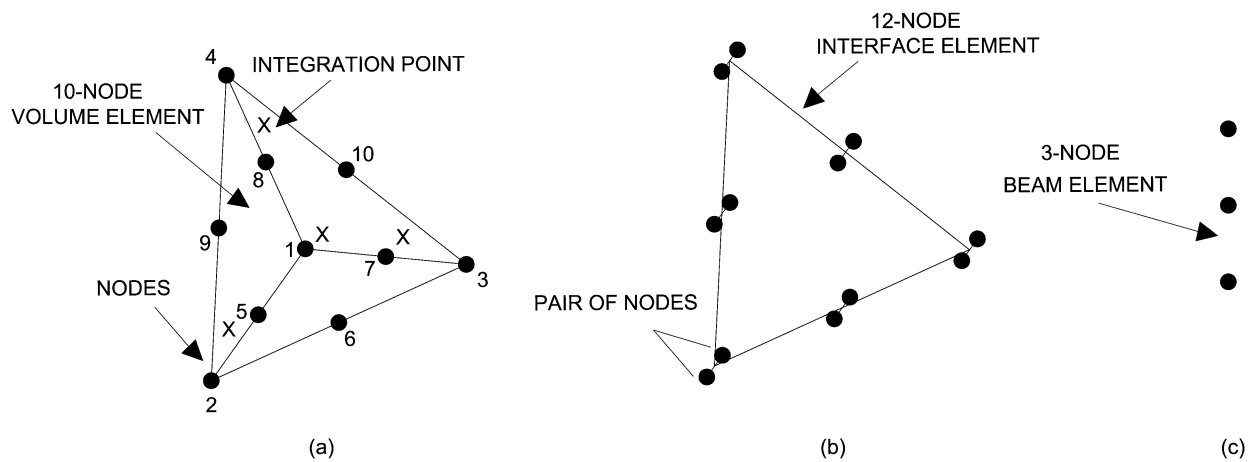


Figure 7-3 (a) Local numbering and positioning of nodes (•) and the integration points (x) of a 10-node tetrahedral element; (b) The 12-node interface element; (c) the 3-node beam element

The standard boundary conditions in PLAXIS 3D are modeled in a way that the sides of the model are restrained horizontally, and the bottom surface is restrained in all directions. Therefore, preliminary models were needed to eliminate the influence of the boundary conditions. The preliminary models were used to identify the extent of the failure zone and to decide on the soil layer horizontal extension. From the preliminary modeling of the shaft under applied shaft head lateral displacement of 10 inches, the lateral boundaries of the soil

domain were selected to be 6 m x 6 m [20 ft x 20 ft], giving a margin of 1.5 m [5 ft] extension past the observed developed zone of plastic strain as shown in Figure 7-4.

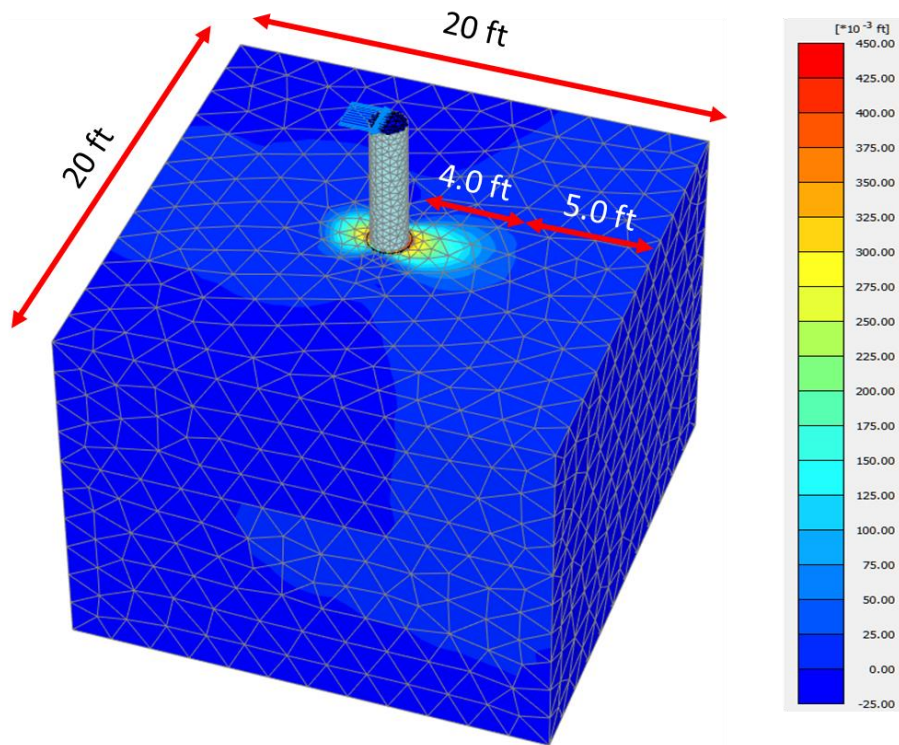


Figure 7-4 Deformation of the soil layer surrounding the shaft (failure zone) at shaft head  
maximum displacement of 25.4 cm [10 in]

## 7.8. Model calibration and validation

Finite element analysis results are strongly dependent on the model input parameters and the constitutive models used to resemble the problem. The input parameters are often uncertain and are based on field and laboratory results that are dependent on the experience and judgment of the engineers carrying out the tests. Thus, model validation and refinement

are necessary to make engineering predictions with quantified confidence. The layout of the validation process followed in this study is shown in Figure 7-5.

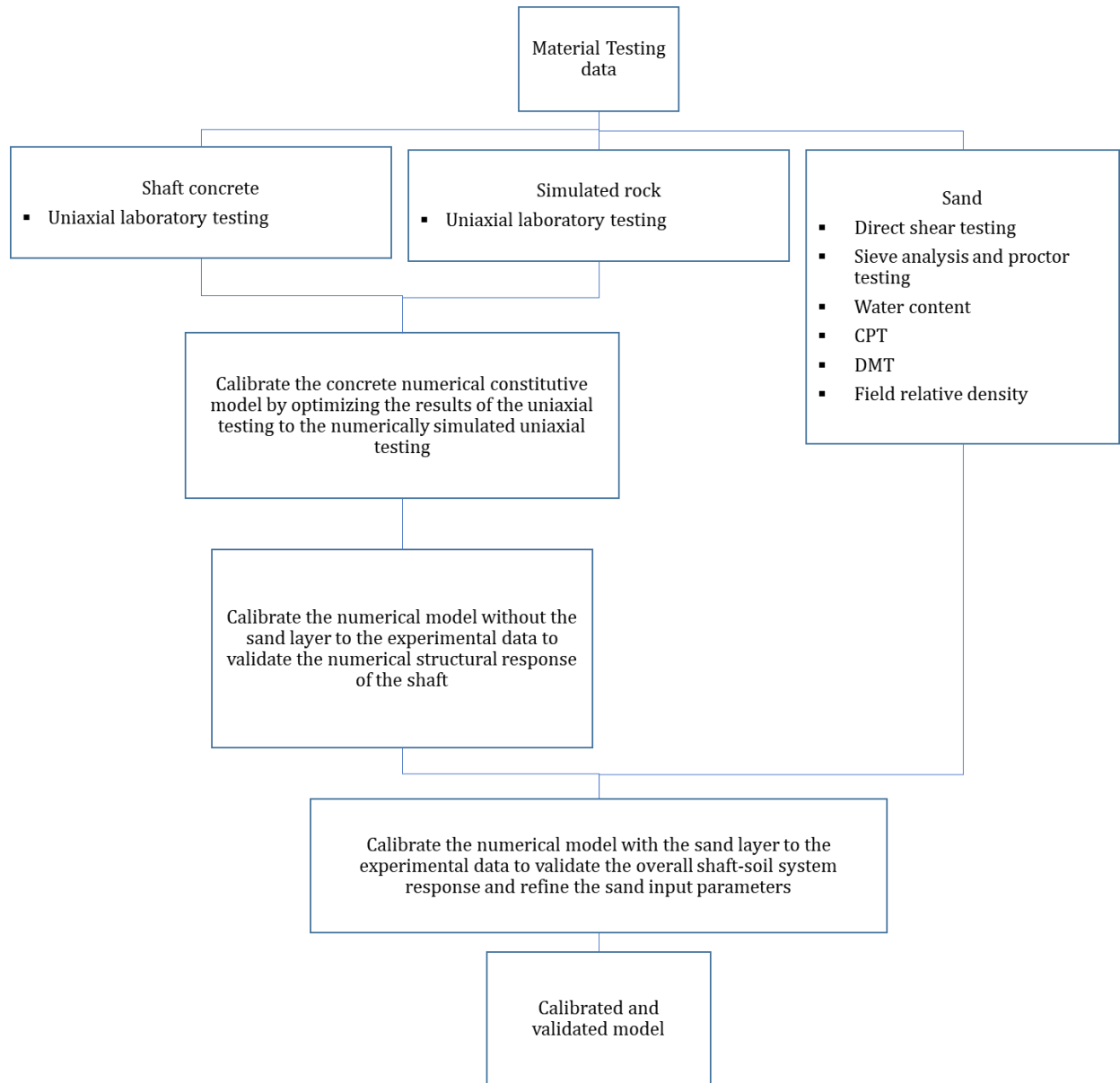


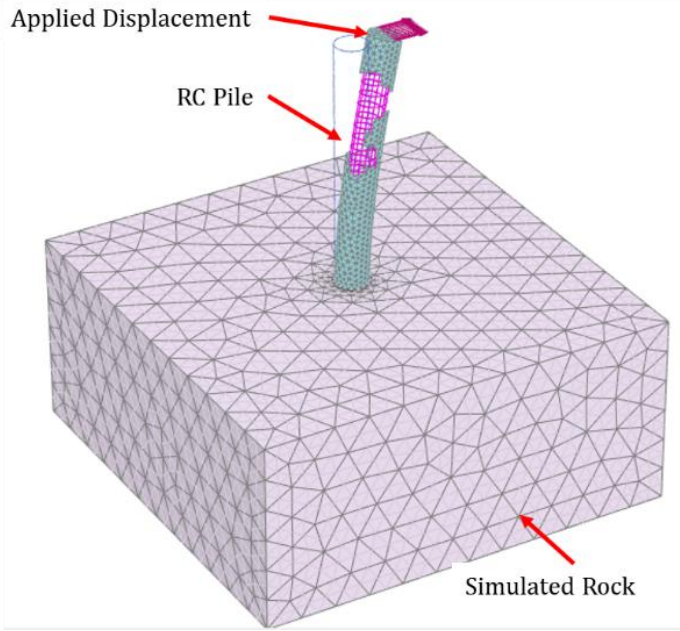
Figure 7-5 Layout of the calibration and validation process

The shaft embedded in the rock-socket was tested under small non-destructive applied lateral displacement levels prior to adding the sand layer in order to assess the shaft linear structural response. The data collected were used in calibrating the preliminary numerical model without the sand. The numerical model input parameters and constitutive model used



are shown in Table 7-5. The experimental moment curvature was evaluated based on the strain data collected from pairs of strain gages located on the two extreme tension/compression (opposite) sides of the shaft. In a similar manner the axial strain was extracted from the numerical model as shown in Figure 7-6. The shaft head applied load could then be translated into moment at any section along the shaft height and above the rock socket, assuming the shaft to behave like a cantilever beam. The experimental and the numerical moment- curvature relationship was evaluated at 6 inches above the rock-socket. The simulated results are in a good agreement with the observed experimental results as shown in Figure 7-7 and Figure 7-8.

Table 7-5 Model inputs for the shaft structural calibration without the sand layer

Configuration	Specimen 1 without sand layer		
	Element	Material model	Parameters
Rock layer	Soil layer	Concrete model	Table 7-3
Sand layer	Deactivated	--	--
Shaft	Volume	Concrete model	Table 7-2
Interface	Virtual layer	Parameters from adjacent soil cluster	$R_{int} = 1$
Reinforcement	Embedded beam	Elasto-plastic	$E = 199948 \text{ MPa}$ [ $29000 \text{ ksi}$ ] $F_y = 413.7 \text{ MPa}$ [ $60 \text{ ksi}$ ]
Applied displacement	Line displacement	--	Cyclic up to 0.05 in
Model			

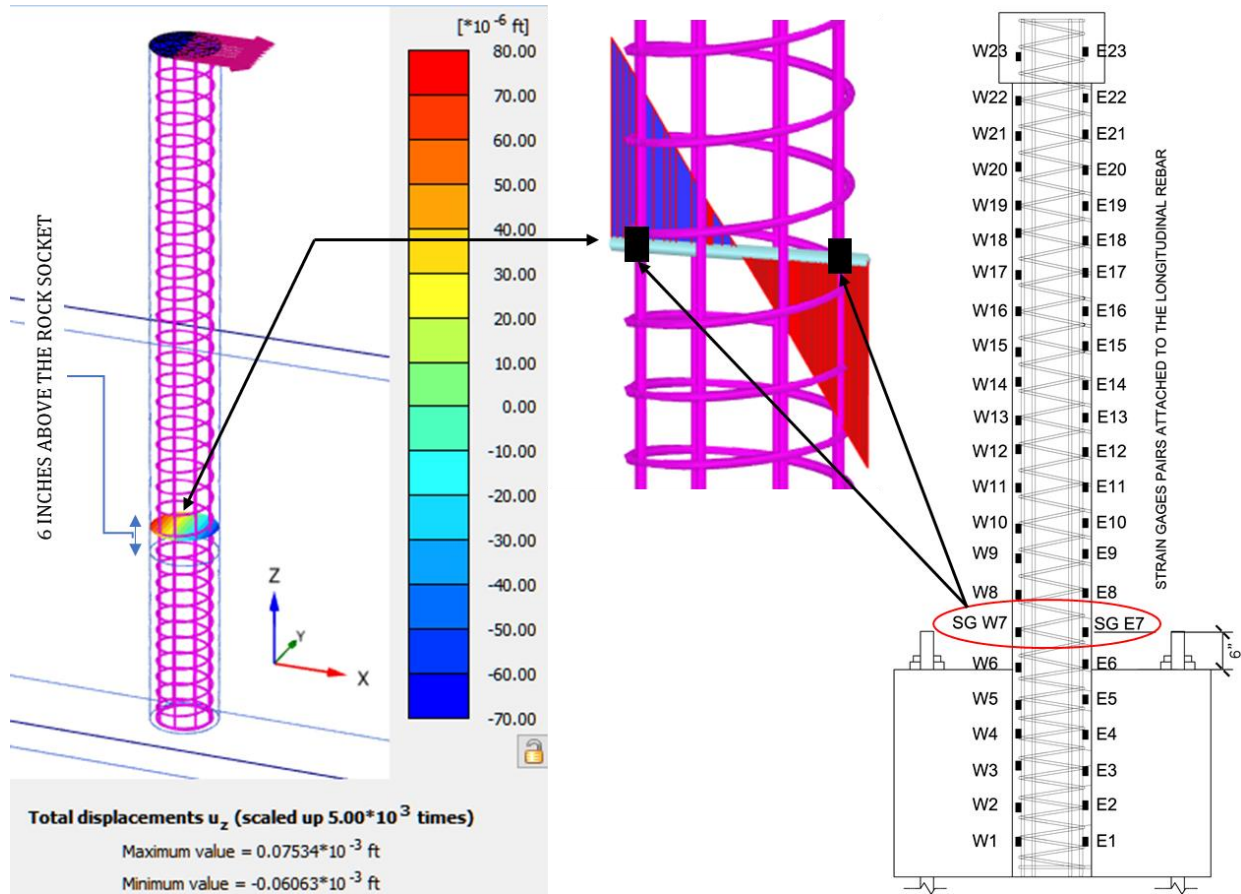


Figure 7-6 Moment – curvature extraction from the numerical model and experimental data

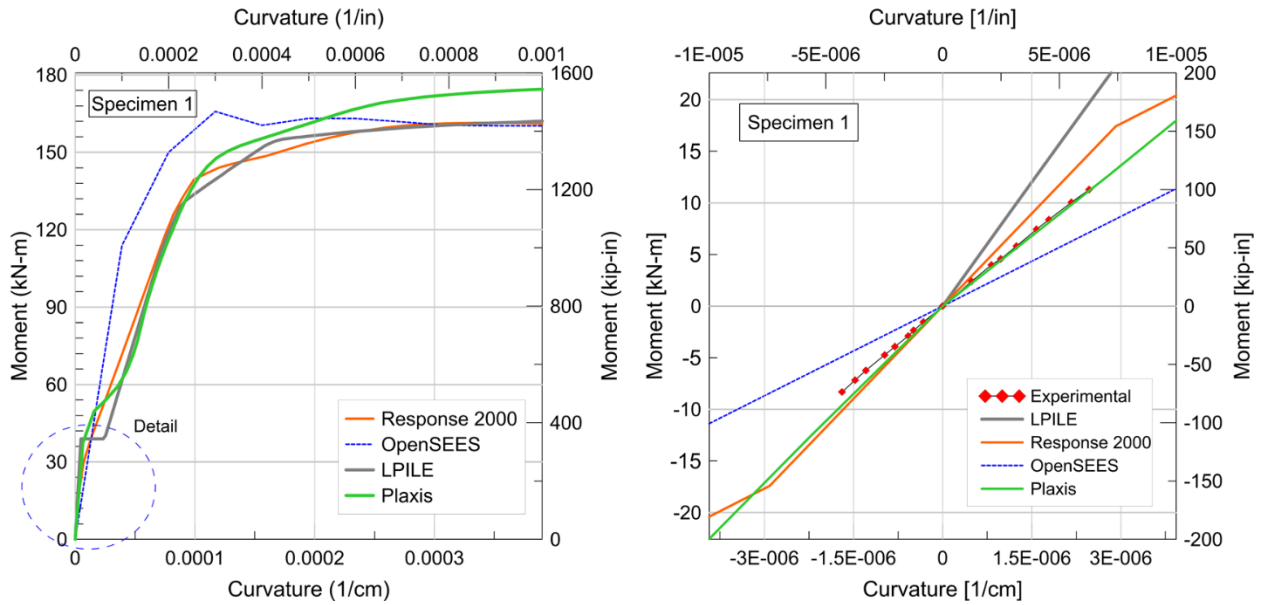


Figure 7-7 Experimental versus numerical moment – curvature relationship comparisons of Specimen 1 without sand

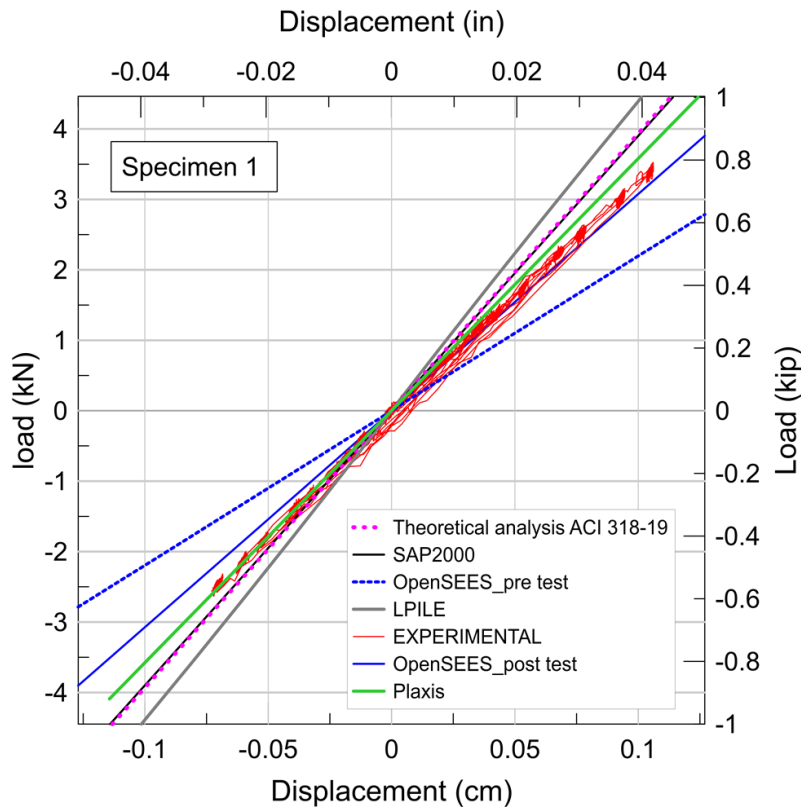
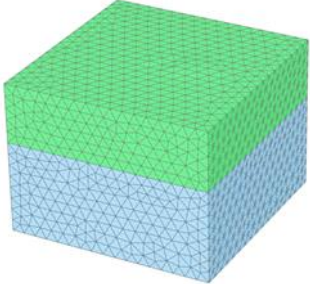
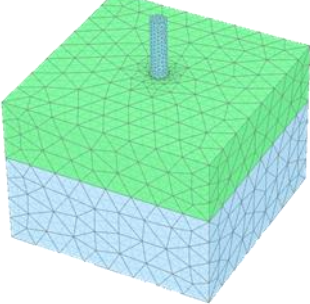
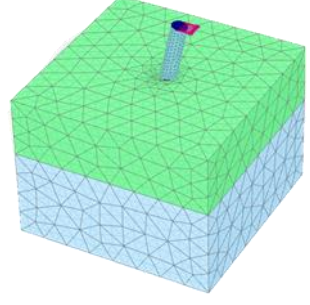


Figure 7-8 Load-displacement curve comparisons between the experimental data

The sand layer was activated in the finite element model and was assigned a Mohr-Coulomb material model. A Mohr-Coulomb model requires a lesser number of input parameters than other advanced models. The input parameters required for modeling consists of cohesion, angle of internal friction, Young's modulus, and Poisson's ratio. The input parameters for the iterative models were the same inputs used in the calibration test without sand, as shown in Table 7-5. Now, however, the sand layer was activated and assigned a Mohr-Coulomb model. In Mohr-Coulomb failure criteria, the internal friction angle of cohesionless soil is the only deriving parameter that draws the failure envelope. Failure occurs when the mobilized shear stress at any plane becomes equal to the shear strength of soil, which in return is a function of the friction angle. The friction angle measured and correlated to different field and laboratory testing varies and is shown in Table 7-4 above. The measured friction angle of 38.4 deg from direct shear testing was adopted for this simulation. The FEA model was calibrated by iteratively changing input values of the sand's Young's modulus until the simulated output values match the observed data (i.e., experimental response). Differing Young's moduli found through correlations from the in-situ testing shown in Table 7-4 above were used, and the finite element model's load-displacement response was compared with the experimental response in order to optimize the selection of the most appropriate value for the in-situ sand's modulus. The sand's cohesion, Poisson's ratio, dilatancy angle, and field density were taken as 0 MPa [ksi], 0.3, 8 deg, and 1478.5 kg/m<sup>3</sup> [92.3 pcf] respectively. The numerical analysis involved three stages, including the initial stage, phase 1, and phase 2. Detailed descriptions of each stage is shown in Table 7-6. To capture the change of the sand's modulus over depth instead of using an average value for the sand's modulus, a linear fit to the Young's modulus correlated data points was used as shown in Figure 7-9. An initial

modulus of 2.8 MPa [0.41 ksi] that linearly increased with depth by 5 MPa/m [0.22 ksi/ft] was used to account for the change of the sand's modulus. Figure 7-10 shows the comparative results of the numerical models' load-displacement response for Specimen 1 with the experimental response. It was found that the model that used an average modulus value to represent the sand behavior showed better agreement with the experimental data than the model that assumed a linear modulus change over depth. It could be seen that the model response that used the sand's average modulus (found through correlation to the CPT data) over depth showed the best agreement to the experimental response.

Table 7-6 Model staged construction phases sequences

Stages	Elements	Activated	Model
Initial (Soil stratigraphy)	Rock layer	✓	
	Sand layer	✓	
	Shaft	✗	
	Interfaces	✗	
	Applied displacement	✗	
Phase 1 (RC shaft)	Rock layer	✓	
	Sand layer	✓	
	Shaft	✓	
	Interfaces	✓	
	Applied displacement	✗	
Phase 2 (loading)	Rock layer	✓	
	Sand layer	✓	
	Shaft	✓	
	Interfaces	✓	
	Applied displacement	✓	

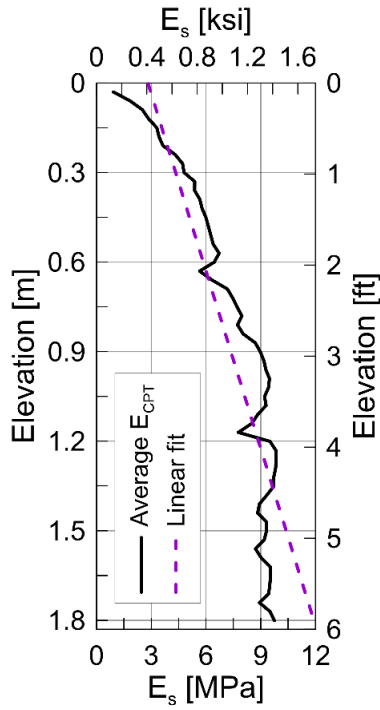


Figure 7-9 Average sand modulus profile correlated to the CPTs profiles versus the linear best fit with depth

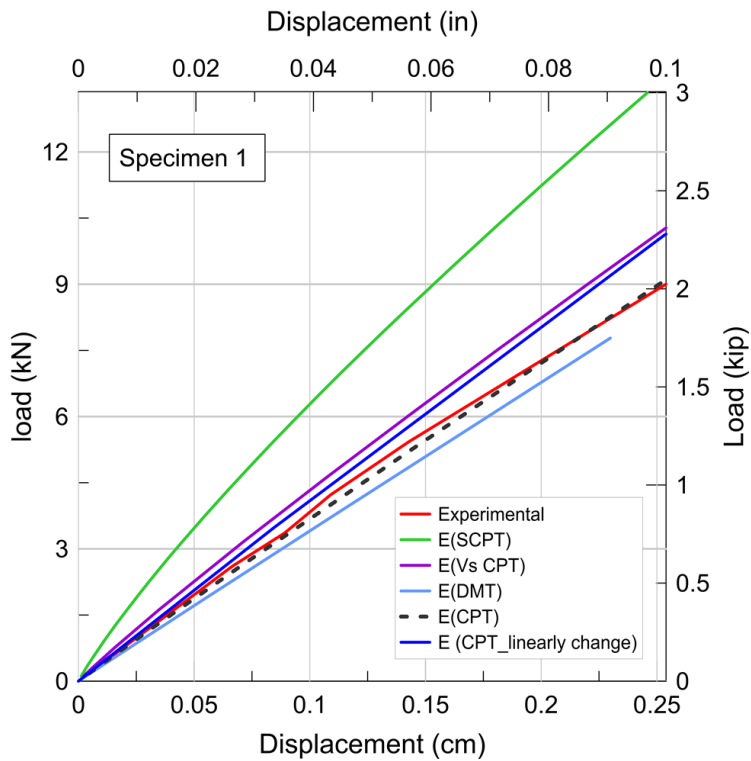


Figure 7-10 Load- displacement relationship at different sand modulus inputs



### **7.9. Shear stresses and forces extraction from the numerical model.**

Shear forces are not typically available for volume elements (shaft) in PLAXIS, therefore, further processing was needed to translate the shear stresses into forces for design purposes. Two methods were considered: (1) Introducing a very flexible (small Young's modulus) beam element to the centerline of the volume element and using its deformed shape and beam theory to derive shear and moment; (2) Integrating the stresses in the stress points along the region perpendicular to the cross-section line. The latter was adopted in this study since it is generally believed to be more accurate, and it correlated to the cross-section internal stresses directly. Figure 7-11 shows schematically the integration process followed in deriving the shear forces from the numerically calculated shear stresses. The internal state of stresses of the embedded portion of the shaft are influenced by the shaft-socket interaction. The stress distribution at the shaft-rock interface can be extracted from the interface virtual element as shown in Figure 7-12.

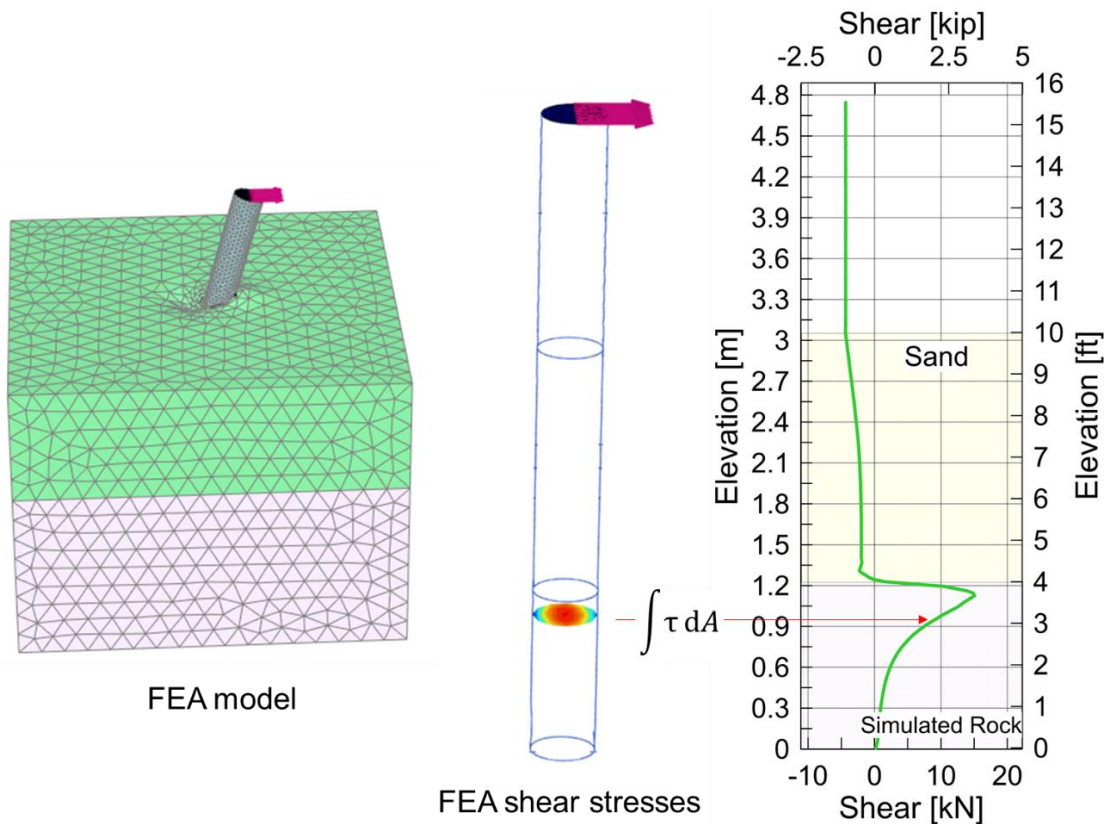


Figure 7-11 Calculation of shear force

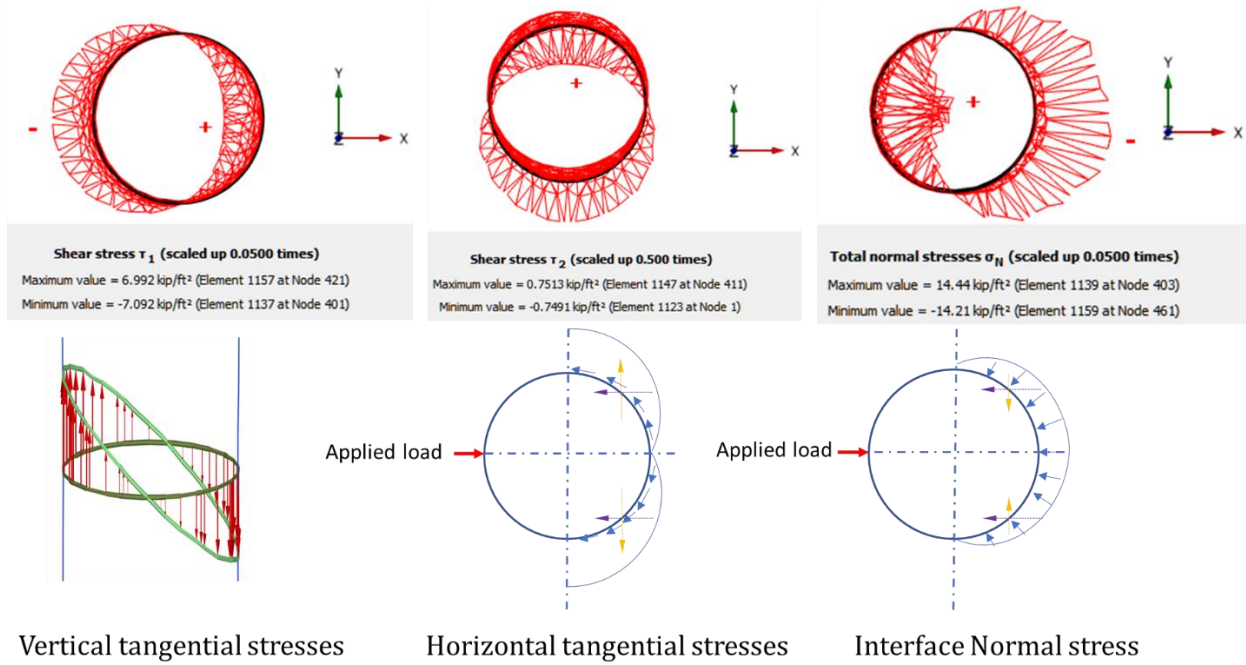


Figure 7-12 Distribution of shaft-rock interface stresses

## 7.10. Shaft internal shear stresses investigation

The state of stresses developed at the shaft-rock interface define the shaft's horizontal shear stresses. For instance, if the side interface resistance (vertical and horizontal tangential stresses) and the tip resistance are ignored, the shaft is expected to mobilize the lateral shear and moment to the rock through horizontal shear only (normal stresses). This assumption is very conservative and tends to develop unprecedented amplified-shear stresses. In contrast, assuming a rigid connection/interface between the shaft and the rock accounts for the ultimate contribution of the side interface tangential resistance and tends to develop the least horizontal shear stresses as shown schematically in Figure 7-13.

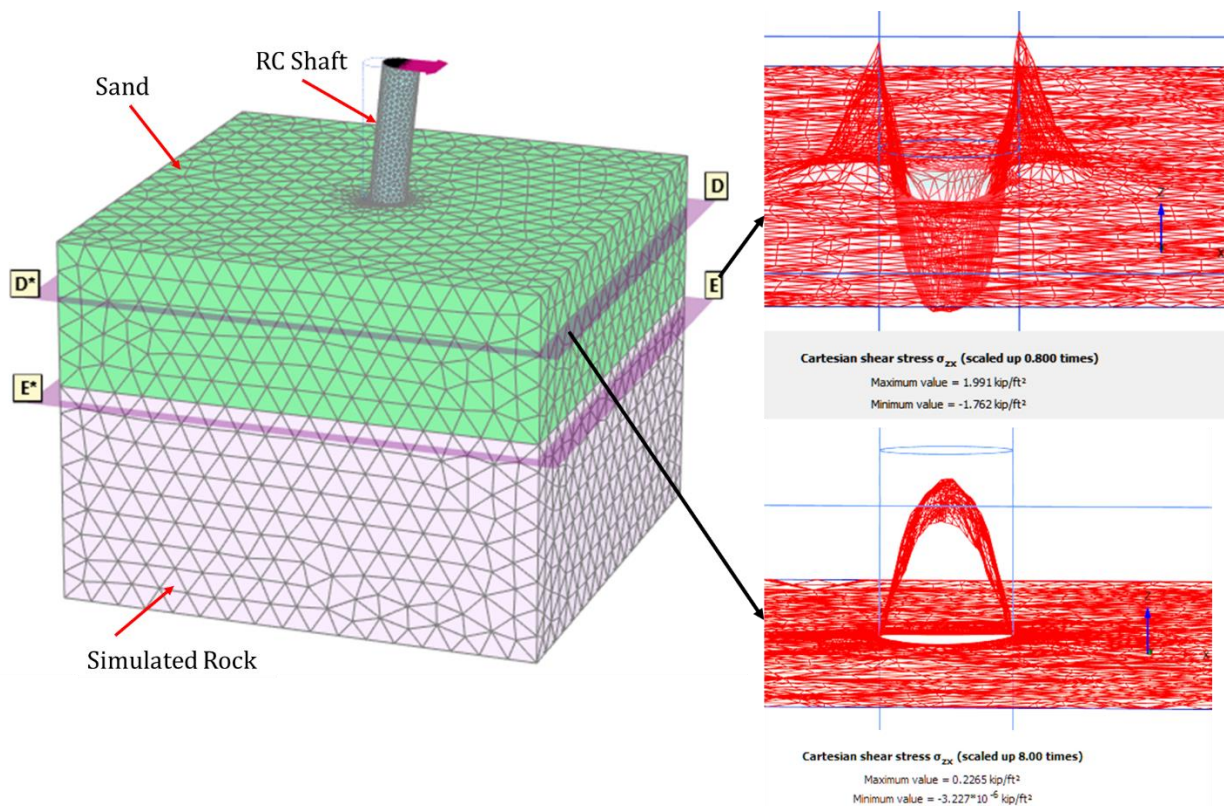


Figure 7-13 Shear stress distribution of the shaft cross-section inside the socket assuming rigid interface connection versus outside the socket

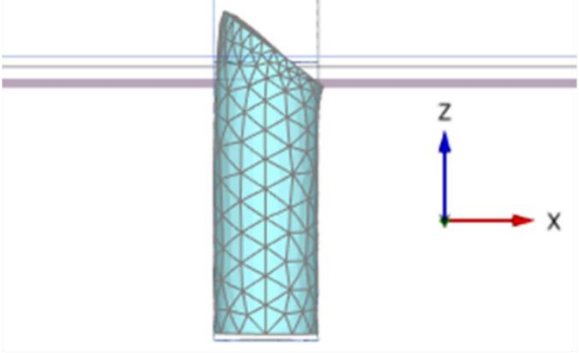
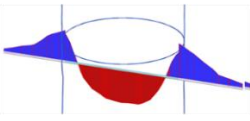
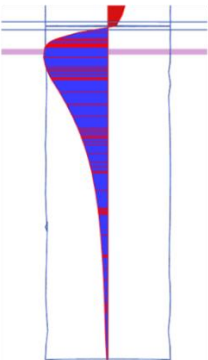
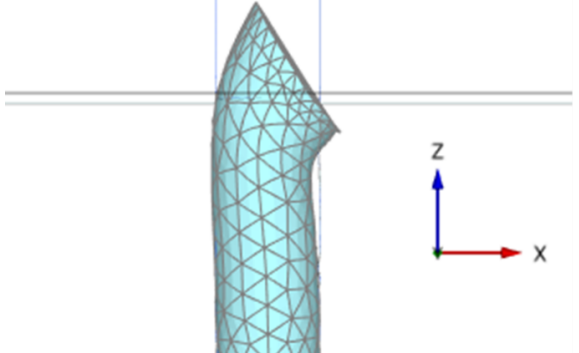
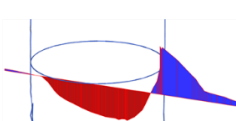
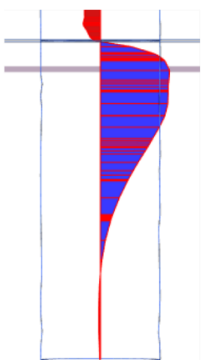
To further investigate the influence of the shaft-rock interface's tangential resistance on the shaft horizontal shear stresses, a parametric study was conducted. In the interface parametric study, the shaft-rock interface element was assigned a Mohr-Coulomb material model, at which the limiting states of stress are described by means of the friction angle,  $\phi$ , cohesion,  $c$ , Young's modulus,  $E$ , and the dilatancy angle,  $\psi$ . It was also appropriate to establish the shaft-rock interface parametric study without the sand layer in order to eliminate the uncertainties introduced by the sand layer response, and to rely exclusively on the load-transfer mechanism between the shaft and the rock. Furthermore, having a soil layer above the rock would only decrease the shear demands at the soil-rock interface. The interface shear friction is directly proportional to the normal forces acting on the interface, through a friction coefficient ( $\mu$ ) which is taken as  $\tan(\phi)$ . Cohesion,  $c$ , input values were assumed to capture the effects of cohesion and the interface interlock.

#### **7.10.1. Shaft-rock interface cohesion influence on the shaft response**

A load of 4.44 kN [1.0 kip] was applied at the shaft head and the shaft response was evaluated at zero cohesion and also at an assumed cohesion value of 0.5 MPa [0.075 ksi]. The latter value was adopted from AASHTO 2020 for concrete placed against a clean concrete surface, free of laitance, and not intentionally roughened. The model input and results are shown in Table 7-7. It can be seen that the interface cohesion had decreased the shaft deformations in comparison to the zero cohesion case. This can be attributed to the fact that the interface cohesion not only improves the friction on the compression side of the shaft (the passive side) but also introduces a tensile resistance to the tension side of the shaft (the active side). Both sides gained resistance, consequently limiting the shaft rotation. The

results also show that the shear demands tend to decrease when taking the interface cohesion into consideration.

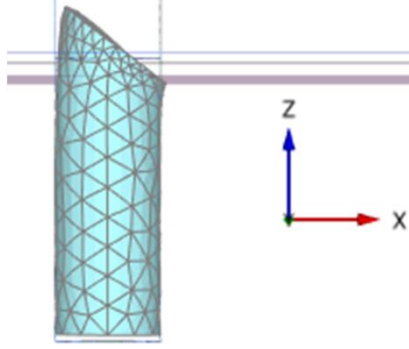
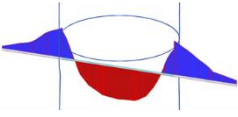
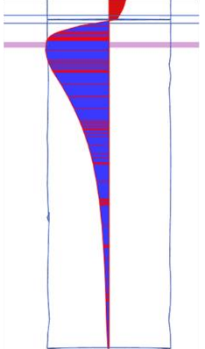
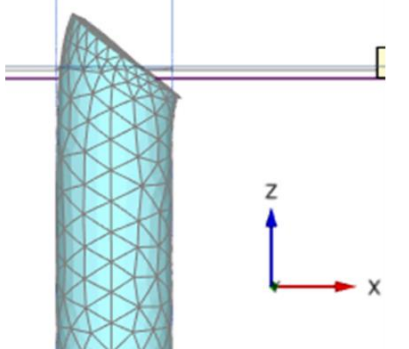
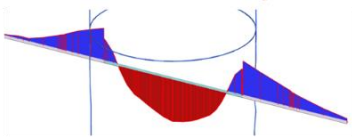
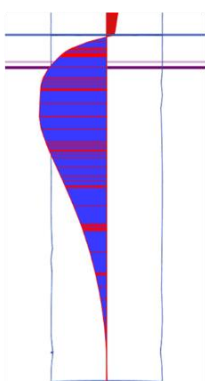
Table 7-7 Shaft internal shear stresses response to different interface cohesion input

MODEL 1	MODEL 2
Cohesion, $c = 0.5 \text{ MPa}$ [0.075 ksi]	Cohesion, $c = 0.0 \text{ MPa}$ [0.0 ksi]
Friction angle, $\phi=45 \text{ deg}$ & $\mu=1$	Friction angle, $\phi=45 \text{ deg}$ & $\mu=1$
dilatancy angle, $\psi=0.0 \text{ deg}$	dilatancy angle $\psi=0.0 \text{ deg}$
Young's modulus, $E = 25462 \text{ MPa}$ [3693 ksi]	Young's modulus, $E = 25462 \text{ MPa}$ [3693 ksi]
 <p><b>Deformed mesh <math> u </math> (scaled up <math>20.0 \cdot 10^3</math> times)</b>  Maximum value = <math>4.059 \cdot 10^{-3} \text{ ft}</math> (at Node 1216)</p>  <p><b>Cartesian shear stress <math>\sigma_{zx}</math> (scaled up 0.100 times)</b>  Maximum value = <math>4.690 \text{ kip/ft}^2</math>  Minimum value = <math>-4.358 \text{ kip/ft}^2</math></p>  <p><b>Shear forces <math>Q_{13}</math> (scaled up 0.200 times)</b>  Maximum value = <math>3.864 \text{ kip}</math>  Minimum value = <math>-1.034 \text{ kip}</math></p>	 <p><b>Deformed mesh <math> u </math> (scaled up <math>20.0 \cdot 10^3</math> times)</b>  Maximum value = <math>4.384 \cdot 10^{-3} \text{ ft}</math> (at Node 1216)</p>  <p><b>Cartesian shear stress <math>\sigma_{zx}</math> (scaled up 0.100 times)</b>  Maximum value = <math>5.640 \text{ kip/ft}^2</math>  Minimum value = <math>-3.727 \text{ kip/ft}^2</math></p>  <p><b>Shear forces <math>Q_{13}</math> (scaled up 0.200 times)</b>  Maximum value = <math>4.335 \text{ kip}</math>  Minimum value = <math>-1.034 \text{ kip}</math></p>

### **7.10.2. Shaft-rock interface friction coefficient influence on the shaft response**

A load of 4.44 kN [1.0 kip] was applied at the shaft head and the shaft response was evaluated at zero friction and at a friction coefficient of 1, which corresponds to a friction angle of 45 deg. The model inputs and results are shown in table 7-8, showing that increasing the interface friction decreases the shear demands.

Table 7-8 Shaft internal shear stresses response to different friction coefficient input

MODEL 1	MODEL 2
Cohesion, $c = 0.075$ ksi	Cohesion, $c = 0.075$ ksi
Friction angle, $\phi=45$ deg & $\mu=1$	Friction angle, $\phi=0.001$ deg & $\mu=0.0$
dilatancy angle, $\psi=0.0$ deg	dilatancy angle $\psi=0.0$ deg
Young's modulus, $E = 25462$ MPa [3693ksi]	Young's modulus, $E = 25462$ MPa [3693 ksi]
 <p><b>Deformed mesh <math> u </math> (scaled up <math>20.0 \times 10^3</math> times)</b>  Maximum value = <math>4.059 \times 10^{-3}</math> ft (at Node 1216)</p>  <p><b>Cartesian shear stress <math>\sigma_{zx}</math> (scaled up 0.100 times)</b>  Maximum value = 4.690 kip/ft<sup>2</sup>  Minimum value = -4.358 kip/ft<sup>2</sup></p>  <p><b>Shear forces <math>Q_{13}</math> (scaled up 0.200 times)</b>  Maximum value = 3.864 kip  Minimum value = -1.034 kip</p>	 <p><b>Deformed mesh <math> u </math> (scaled up <math>20.0 \times 10^3</math> times)</b>  Maximum value = <math>4.079 \times 10^{-3}</math> ft (at Node 1216)</p>  <p><b>Cartesian shear stress <math>\sigma_{zx}</math> (scaled up 0.100 times)</b>  Maximum value = 3.458 kip/ft<sup>2</sup>  Minimum value = -4.204 kip/ft<sup>2</sup></p>  <p><b>Shear forces <math>Q_{13}</math> (scaled up 0.200 times)</b>  Maximum value = 4.538 kip  Minimum value = -1.034 kip</p>



### 7.10.3. Rock-shaft relative elastic modulus influence on the shaft response

The effect of the relative elastic modulus between the shaft and the rock was studied. The rock modulus ranged between 0.5 to 4 times the shaft modulus. Other parameters were kept constant:  $E_{\text{shaft}} = 27579 \text{ MPa}$  [4000 ksi],  $\nu = 0.15$ ,  $c = 0.5 \text{ MPa}$  [0.075 ksi], and  $\phi = 45 \text{ deg}$  ( $\mu = 1$ ). Moment and shear profiles are shown in Figure 7-14. The results indicate that increasing the rock-shaft relative modulus ( $E_{\text{rock}}/E_{\text{shaft}}$ ) decreases the shear demands. Through investigating the axial deformation that the shaft experienced inside the rock-socket, it could be seen that the stiffer the rock was, the smaller the axial deformations were (see Figure 7-14). It was also found that the ‘plane sections remain plane’ assumption (Bernoulli beam theory) may not be valid for the behavior of the shaft inside the rock socket.

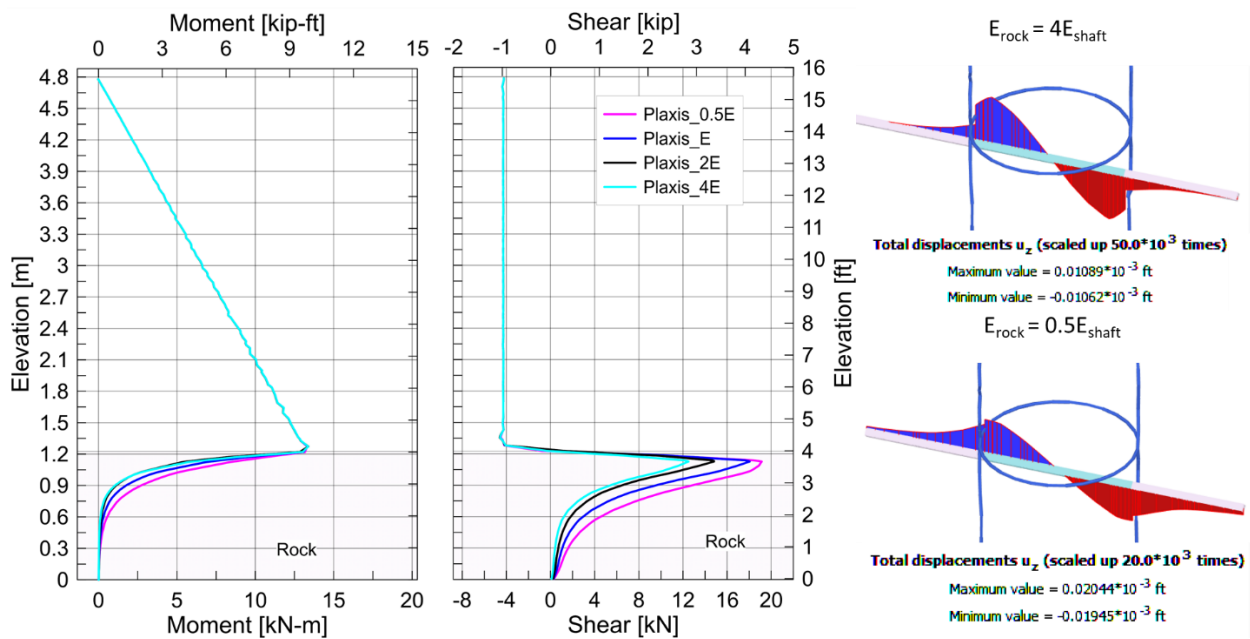


Figure 7-14 Moment and shear profile of the shaft at different shaft-rock relative linear moduli, and the corresponding cross-sectional axial deformation

#### **7.10.4. Experimental shear demands in comparison to numerically generated demands**

Experimental shaft shear demands are usually mathematically derived from strain gages and/or inclinometer data. This process is challenging and not necessarily accurate since it involves differentiation and integration, and the error in the measured data accumulates. Therefore, the embedded tetrahedra were believed to be the most direct measurement to the internal three-dimensional strains. Shear stresses calculated from the tetrahedra data collected from the shaft cross-section at maximum shear (see Figure 7-15) was compared to the shear stresses found numerically as shown in Figure 7-16. It can be seen that the numerical shaft cross-sectional shear stresses are in good agreement with the experimental shaft cross-sectional shear stresses. It was also found that both the numerical and the experimental shear stresses at the maximum shear location inside the rock-socket were dramatically less than those found by the p-y method using the weak rock model by Reese (1978). The experimental moment profile established based on the longitudinal strain gage data and the calibrated moment curvature relationship were generally in good agreement with the numerical results. Conversely, the moment profile of the embedded portion of the shaft did not agree well with the LPILE (p-y method) results as shown in Figure 7-17. The moment at the soil-rock interface was transferred to the rock over a longer depth both experimentally and numerically, in comparison to the p-y method.

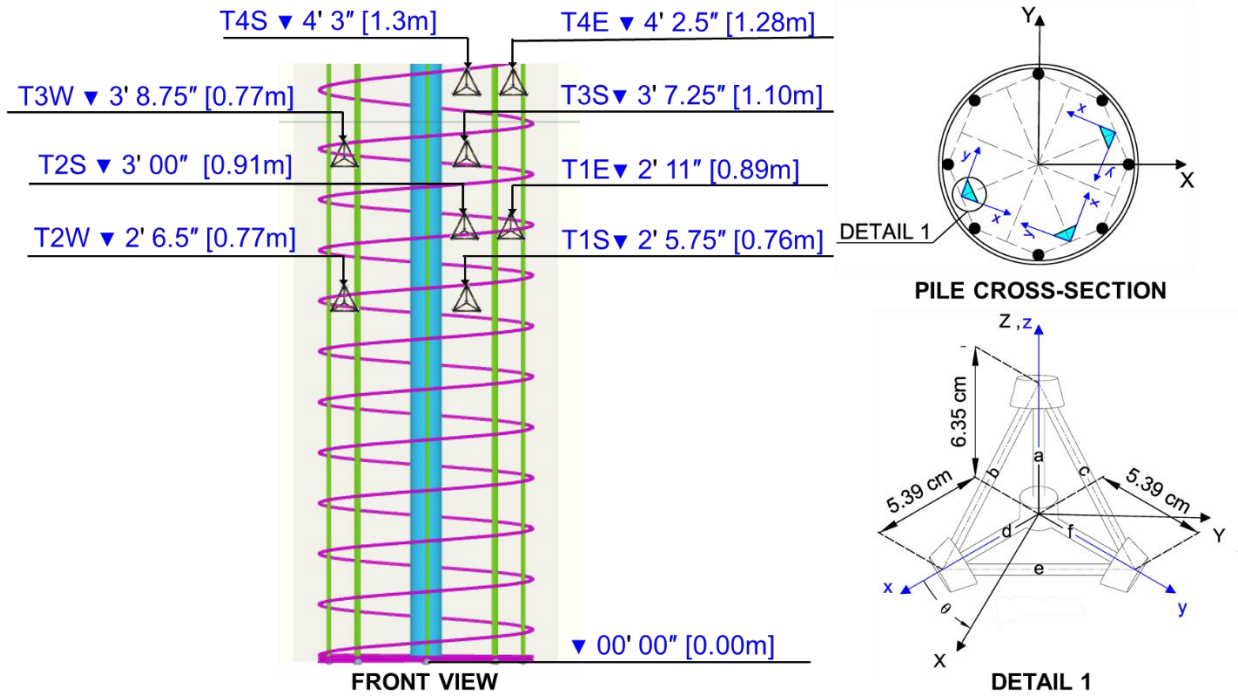


Figure 7-15 Embedded tetrahedra locations and orientation to the shaft global axis

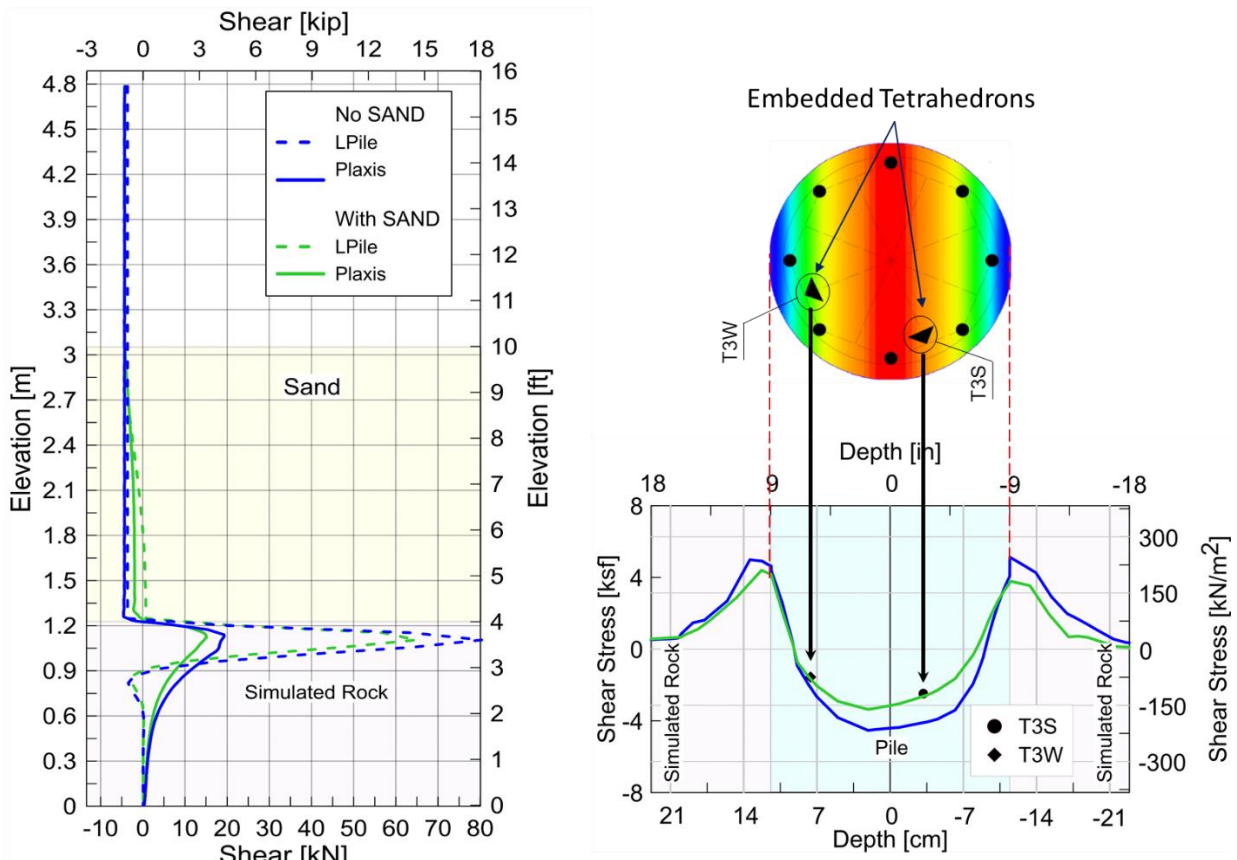


Figure 7-16 Experimental shaft cross-sectional shear stresses versus shear stresses found numerically

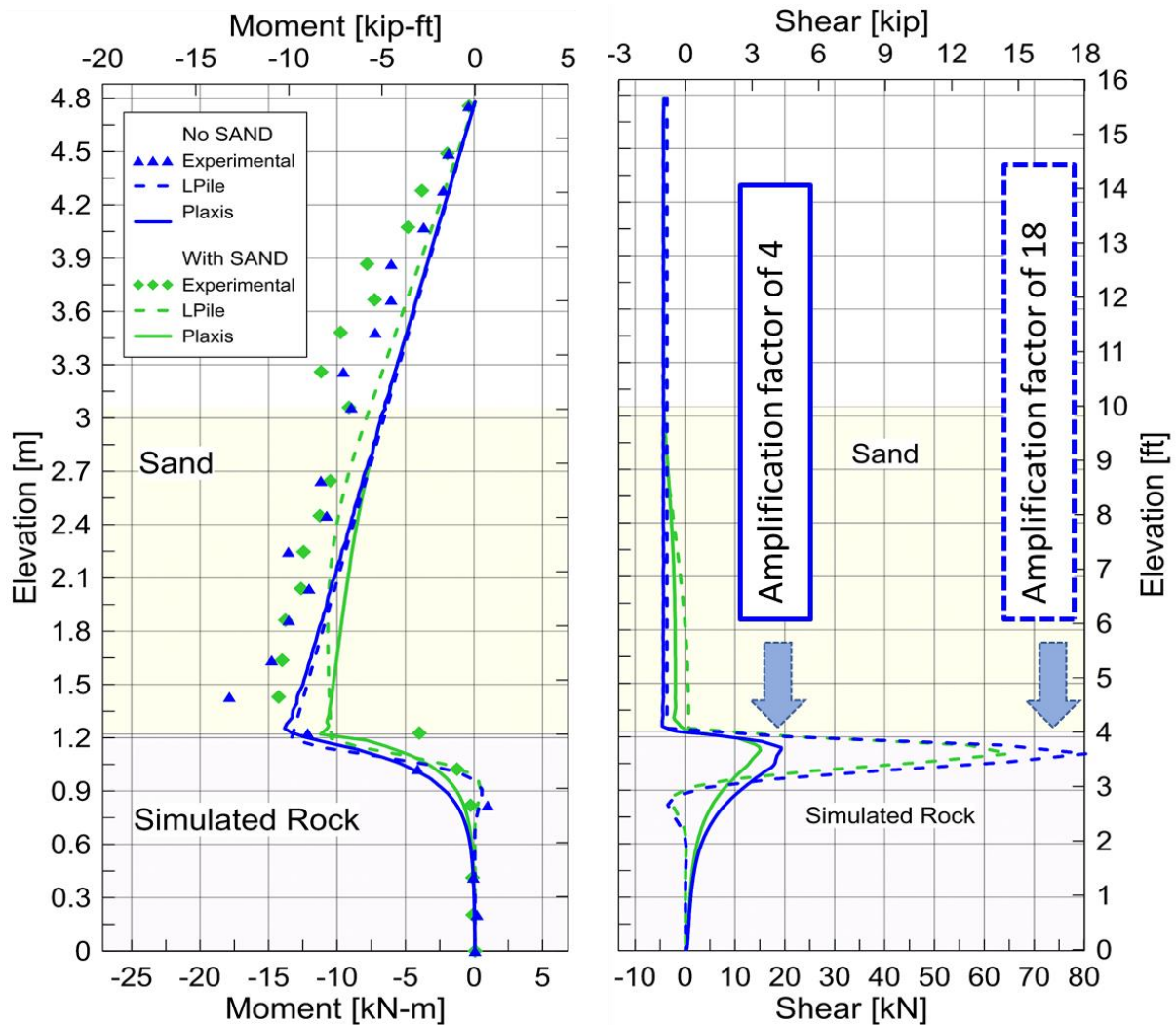


Figure 7-17 Moment and shear profile comparisons between experimental, LPILE (p-y method), and numerical simulation of Specimen 1 with and without the sand layer

### 7.11. Conclusion

The three-dimensional numerical simulation was established by means of the three-dimensional finite-element approach of PLAXIS 3D. Initially, the available material constitutive models were investigated and calibrated to the in-situ data. Different elements to simulate the shaft, soil, and the interface behavior were examined. Lastly, the FEA response was calibrated to the experimental shaft response. The calibrated models were

used to gain insight into the shaft's internal field of stresses and to develop a better understanding of the load transfer mechanism. The shaft-rock interface behavior was believed to be a key factor that influences the field of the stresses in the embedded portion of the shaft. Therefore, an interface parametric study was established to further investigate the matter. Based on the numerical results, the following conclusions can be drawn:

- 1- Numerical simulations were conducted to evaluate the capabilities and limitations of modeling each component of the numerical model (i.e., shaft, rock, and soil). It was found that modeling the shaft as a volume element rather than an embedded beam element was necessary to evaluate the cracking process and to incorporate the non-linear behavior of concrete under lateral loads.
- 2- Since the field data collected for sands using different means of testing and correlations varied significantly, the soil model was calibrated using an inverse analysis technique. Numerical simulations suggested that this technique was effective to optimize the sand model parameters in order to minimize the difference between the experimental shaft response and the numerically computed response.
- 3- Zero-thickness interface elements used to model the mechanical behavior of the interface of the socket (between the shaft and the rock) was found effective to realistically model interface discontinuities.
- 4- Numerical simulations were conducted to evaluate the lateral extents of the numerical model. It was found that a lateral distance of 10 times the shaft diameter and 18 times the maximum lateral displacement, as measured from the center of the shaft, was required to minimize the influence of the boundary conditions.

- 5- Calculating the shaft shear force through integration of shear stresses along the region perpendicular to the cross-section of the shaft provided a numerically direct measurement of the shear demand.
- 6- The state of stresses developed at the shaft-rock interface influenced the shaft horizontal shear stresses. It was found that if the side interface resistance (vertical and horizontal tangential stresses) and the tip resistance were ignored, the shaft was expected to mobilize lateral shear and moment to the rock through horizontal shear only (normal stresses), which resulted in high shear stresses. In contrast, it was found that assuming a rigid connection/interface between the shaft and rock accounted for the ultimate contribution of the side interface tangential resistance and tended to develop low horizontal shear stresses.
- 7- It was found that shaft deformations decrease with increasing adhesion, and that shear demands tend to decrease with increasing adhesion. This can be attributed to the fact that adhesion not only improves the interface shear resistance on the compression side of the shaft (the passive side), but also introduces tensile resistance to the tension side of the shaft (the active side). Both gained resistances limit shaft rotation.
- 8- The results indicate that shear demands decreased with increasing interface friction.
- 9- The results indicate that shear demands decreased with increasing rock-shaft relative modulus ( $E_{\text{rock}}/E_{\text{shaft}}$ ). It was found that the axial deformation that a shaft experienced inside the rock-socket decreased with increasing the relative modulus.
- 10- It was also found that the 'plane sections remain plane' assumption (Bernoulli beam theory) may not be valid for the behavior of the shaft inside the rock socket. Primarily

because the deformed shape of the shaft cross-section is restricted at the circumference from displacement as the cross-section rotates.

11-Numerical predictions of shear stress could be validated against instrumentation data obtained from the tetrahedron strain-gauge carrier.

12-It was concluded that shear stresses at the maximum shear location inside the rock-socket (obtained both numerically and experimentally) were less than those estimated by the p-y method using the “weak rock” model by Reese (1978).

13-The moment at the soil-rock interface was distributed to the rock over a longer depth experimentally and numerically in comparison to the p-y method.



## Chapter 8

### **Summary and Conclusions**

This dissertation documents a comprehensive study conducted to evaluate the behavior of shafts socketed in rock under reverse cyclic lateral loading. Specifically, the study aimed at assessing the shear force amplification on the shaft at the soil-rock interface. The study involved a comprehensive experimental study on full-scale shafts constructed at the University of California, Irvine soil-pit testing facility. The test shafts were constructed with different transverse reinforcement design intended to bound the amplitude of the predicted amplified shear demand, with a particular emphasis on performance of shafts with shear resistance less than the predicted demand and below the code minimum. State-of-the-art instrumentation and monitoring program was implemented to capture the behavior of the test shafts during loading. As part of the instrumentation program, a new sensor was developed that aimed at measuring concrete internal strains in three dimensions. The sensor comprises of 6 strain gauges mounted on a tetrahedral skeleton, which was tested and calibrated in separate experimental setups to validate its efficacy in accurately measuring the concrete internal strains. Furthermore, the tested shafts were retested again after increasing the overburden in which they were contained by increasing the thickness of the soil above the rock. This retesting facilitated evaluating the mechanical response of the distressed shafts upon increasing the overburden. Finally, a three-dimensional, finite-element numerical model was developed to simulate the behavior of shafts socketed in rock under lateral loads. The numerical model was validated by comparing the predicted mechanical response against that obtained from the full-scale experiments. The main findings of each of component of this dissertation are presented in the following sections.

## **8.1. Experimental study findings**

### **8.1.1. Testing of the shaft specimens**

Pile specimens were loaded to complete structural failure and examined after test completion. No damage (*i.e.*, cracking) and no lateral shaft deformations were observed inside the rock socket. However, predominantly flexural cracking was observed along the shafts within 0.6 m [2 ft] above the rock socket. This elevation corresponds to a depth of three shaft diameters below ground surface, which is the typical location for plastic hinges of flexible shafts. The differently reinforced shaft specimens would be expected to fail in different failure modes according to their transverse reinforcement ratios and the predicted shear amplification using the  $p$ - $y$  method. The experimental specimen behavior showed that the analytically predicted shear dominated failure did not occur. These preliminary observations could be of future benefit to the construction industry as bulky transverse reinforcement could be minimized and potential issues such as restrictions of concrete flow resulting in defective concrete due to closely spaced transverse reinforcement could be reduced. This study is limited to one configuration (one rock layer underlying one soil layer) and one shaft geometry with varying shear reinforcement ratios. However, the extensive physical measurements collected from the variety of reliable sensor instrumentation allow for advanced parametric studies using a validated numerical model established on the test results. Additional structural limitations such as the lack of axial shaft loading and the investigation of its effect on the structural behavior of the shaft has limited impact on the result of this experiment and can be accounted for numerically. Since the soil materials was placed in very loose densities, its contribution to the overall lateral shaft-soil resistance is

limited. A strict structural model of the horizontally loaded shaft (without soil) provides very close response behavior to that observed in the experimental studies conducted by the authors. This is expected from a structural point of view. However, in common geotechnical design, soil is not omitted in the foundation model and leads to analytical response predictions as addressed in this study. The experimental observations highlight the importance of numerical assumptions and their consequences on construction performance.

### **8.1.2. Retesting of the shaft specimens**

Following initial testing of pile specimens to complete structural failure, the soil stratigraphy was modified by raising the overburden materials to strategically shift the initially developed plastic hinge to a higher elevation and to provide additional confinement around the shaft specimens during retesting. The retesting experimental results suggested that adding a 1.2 m [4ft] thick soil layer was able to recover the initial stiffness of the failed shafts by 100% for Specimen 2 and by 60% for Specimen 3. The lateral reinforcement ratio substantially influenced the shaft ability to restore the initial shaft stiffness but had less contribution to recovering the ultimate shaft capacity. The proposed increase of the soil stratigraphy raised the ultimate shaft capacity of Specimens 2 and 3 by 80% and 70%, respectively. The ductility and energy dissipation of the retested shafts improved greatly as a result of extending/relocating the pre-existing plastic hinge rather than introducing repairs to the plastic hinge region. Despite the different transverse reinforcement ratios, Specimens 2 and 3 reached the same level of ductility during Phase 2 testing, which can be attributed to the confinement provided by the increase in sand surcharge. Findings of this experimental study suggest that modifications to the soil stratigraphy around the shaft upon

partial or full loss of structural shaft integrity could provide a temporary solution for post-earthquake retrofit and temporary increase or recovery of shaft-soil capacity.

## **8.2. The implementation of the newly developed sensor summary**

Three-dimensional embeddable sensor named iTET was designed, developed, and evaluated. The use of 3D printed temporary molds during the sensors construction enhanced the quality of the iTETs and eliminated the geometrical errors. The iTET sensors were to be embedded into materials to measure, in-situ, all nine components of strain. The iTET measured data quality was investigated by testing them in a known strain field. The measured data were compared with the numerically generated data for validation. The agreement with the numerically generated data validated the applicability of using the iTET sensors to extract the internal shear strain in concrete. Following independent sensor validation, the sensors were used in the full-scale shaft experiments to measure three-dimensional strains, which was then facilitated calibrating the finite-element numerical models.

## **8.3. The numerical study summary**

The calibrated finite-element numerical models were used to further investigate the shaft internal field of stresses and to develop a better understanding of the load transfer mechanism. It was concluded that the shaft-rock interface behavior is a key factor that influences the field of stresses in the embedded portion of the shaft. The shaft was modeled as a volume instead of volume-less structural element, which allowed for evaluation of the cracking process and incorporate the non-linear behavior of concrete under lateral loads. The lateral extents of the model were taken as 10 times the shaft diameter and 18 times the

maximum lateral displacement, as measured from the center of the shaft, which was found to minimize the influence of the boundary condition.

To evaluate the shear forces from the numerical model predictions, stresses were integrated along the region perpendicular to the cross-section of the shaft. The state of stresses developed at the shaft-rock interface was found to influence the shaft horizontal shear stresses. If the side interface resistance (vertical and horizontal tangential stresses) and the tip resistance are ignored, the shaft is expected to mobilize the lateral shear and moment to the rock through horizontal shear only (normal stresses), which results in high shear stresses. In contrast, it was found that assuming a rigid connection/interface between the shaft and the rock accounts for the ultimate contribution of the side interface tangential resistance and tends to develop low horizontal shear stresses. It was also found that the plane sections remain plane assumption (Bernoulli beam theory) may not be valid for the behavior of the shaft inside the rock socket. This is because the deformed shape of the shaft cross-section is restricted at the circumference from displacement as the cross-section rotates.

Upon varying the interface shear strength parameters, it was found that shaft deformations decrease with increasing adhesion, and that shear demands tend to decrease with increasing adhesion. This could be attributed to the fact that adhesion not only improves the interface shear resistance on the compression side of the shaft (the passive side), but also introduces tensile resistance to the tension side of the shaft (the active side). Both gained resistances limit shaft rotation. Moreover, the results indicate that shear demands decrease with increasing interface friction. The results also indicate that shear demands decrease with increasing rock-shaft relative modulus (ratio of rock Young's modulus to shaft Young's

modulus). It was found that the axial deformation that a shaft experiences inside the rock-socket decreases with increasing the relative modulus.

Finally, it was concluded that shear stresses at the maximum shear location inside the rock-socket (obtained both numerically and experimentally) were dramatically less than those estimated by the p-y method using the “weak rock” model by Reese (1978). The moment at the soil-rock interface was distributed to the rock over a longer depth experimentally and numerically in comparison to the p-y method.

## Chapter 9

### 9.1. References

- American Association of State Highway and Transportation Officials, AASHTO (2017) AASHTO LRFD 8th Bridge Design Specifications. Washington, D.C.
- American Concrete Institute, 2019. Building Code Requirements for Structural Concrete (ACI 318-19) and Commentary (ACI 318R-19)
- American Society of Civil Engineers (ASCE). (2017). "Seismic evaluation and retrofit of existing buildings", ASCE/SEI 41-17, Reston, VA.  
*and Geoenvironmental Engineering, ASCE, 135(1), 26–36.*
- Arduino, A., Chen, L. and McGann, C. (2018). Estimation of Shear Demands on Rock-Socketed Drilled Shafts subjected to Lateral Loading. PEER Report Nr. 2018/06, retrieved from [https://peer.berkeley.edu/sites/default/files/2018\\_06\\_arduino\\_final.pdf](https://peer.berkeley.edu/sites/default/files/2018_06_arduino_final.pdf)
- Ashour, M., Norris, G., Bowman, S. Beeston, H. Pilling, P. and Shamsabadi, A. (2001). "Modeling shaft lateral response in weathered rock", Proceedings, 36th Annual Symposium on Engineering Geology and Geotechnical Engineering, Eds Luke, Jacobson & Werle, University of Nevada, Las Vegas, March 28-30, 2001.
- ASTM C31 / C31M-18. (2018). "Standard Practice for Making and Curing Concrete Test Specimens in the Field", ASTM International, West Conshohocken, PA, [www.astm.org](http://www.astm.org)
- ASTM D1557-12e1. (2012) "Standard Test Methods for Laboratory Compaction Characteristics of Soil Using Modified Effort (56,000 ft-lbf/ft<sup>3</sup> (2,700 kN-m/m<sup>3</sup>))". ASTM International, West Conshohocken, PA, [www.astm.org](http://www.astm.org)
- ASTM D3080 / D3080M-11. (2011). "Standard Test Method for Direct Shear Test of Soils Under Consolidated Drained Conditions". ASTM International, West Conshohocken, PA, [www.astm.org](http://www.astm.org).
- ASTM D5778-12. (2012). "Standard Test Method for Electronic Friction Cone and Piezocone Penetration Testing of Soils". ASTM International, West Conshohocken, PA, [www.astm.org](http://www.astm.org).
- ASTM D5778-20. (2020), Standard Test Method for Electronic Friction Cone and Piezocone Penetration Testing of Soils, ASTM International, West Conshohocken, PA, 2020, [www.astm.org](http://www.astm.org)
- ASTM D6635-15. (2015). "Standard Test Method for Performing the Flat Plate Dilatometer". ASTM International, West Conshohocken, PA, [www.astm.org](http://www.astm.org).

- Baker, W. E., & Dove, R. C. (1963). Construction and evaluation of a three-dimensional strain rosette. *J Experimental Mechanics*, 3(9), 201-206.
- Bentz, E.C. (2000). "Sectional Analysis of Reinforced Concrete Members," PhD Thesis, Department of Civil Engineering, University of Toronto, 310 pp
- Brasier, R. I., & Dove, R. C. (1961). Use of electrical-resistance strain elements in three-dimensional stress analysis. *Experimental Mechanics*, 1(6), 186-191.
- Brinkgreve, R., Zampich, L., & Ragi Manoj, N. (2019). PLAXIS CONNECT Edition V20. Plaxis bv, Bentley Systems, incorporated. Printed in the Netherlands.
- Brown, D. A., Turner, J. P., Castelli, R. J., & Americas, P. B. (2010). Drilled shafts: Construction procedures and LRFD design methods (No. FHWA-NHI-10-016). United States. Federal Highway Administration.
- Brown, D., & Shie, C.-F. (1990). Three Dimensional Finite Element Model of Laterally Loaded Shafts. *Computers & Geotechnics* 10, 59-79
- Caltrans, F. (2015). Bridge design practice, 4th edition. California Department of Transportation, Sacramento, CA.
- Carter, J.P. and Kulhawy, F.H. (1992). "Analysis of laterally loaded shafts in rock". *ASCE Journal of Geotechnical Engineering*, Vol. 118, No. 6, pp.270ff.
- Choi, J., Kim, M., & Brandenberg, S. (2015). Cyclic p-y Plasticity Model Applied to Shaft Foundations in Sand. *J. Geotech. Geoenviron. Eng.*, 141(5).
- D C, Prager W (1952). " Soil mechanics and plastic analysis or limit design". *Journal of applied Mathematics*, Drucker 10, 157-165
- Dykeman, P. and Valsangkar, A.J. (1996). "Model studies of socketed caissons in soft rock". *Canadian Geotechnical Journal* 33: 747-759
- Ensoft,Inc (2018) – LPLIE User’s Manual. A Program to Analyze Deep Foundations Under Lateral Loading. Austin, Texas.
- Ensoft,Inc (2018) – LPLIE User’s Manual. A Program to Analyze Deep Foundations Under Lateral Loading. Austin, Texas.
- Frantzen, J. and Stratten, F.W. (1987). P-y curve data for laterally loaded shafts in shale and sandstone. Report No. FHWA-KS-82-2
- Gabr, M., Borden, R., Cho, K., Clark, S., and Nixon, J. (2002). "P-y Curves for Laterally Loaded Drilled Shafts Embedded in Weathered Rock", Technical Report, North Carolina Department of Transportation, Raleigh, North Carolina



- Guo, F. and Lehane, B.M. (2016). "Lateral response of shafts in weak calcareous sandstone". *Can. Geotech.Journal*, 53: 1424–1434 dx.doi.org/10.1139/cgj-2015-0600
- Jamiolkowski, M., LoPresti, D.C.F. and Manassero, M. 2001. "Evaluation of relative density and shear strength of sands from cone penetration test and flat dilatometer test", *Soil Behavior and Soft Ground Construction (GSP 119)*, ASCE, Reston, Virginia: 201- 238.
- Khosravifar, A. and Zafir, Z. (2019). "Modified strong rock p-y curves for rock socketed shaft shafts". *Deep Foundations Journal*, Vol 13 (1), DOI 10.1080/19375247.2019.1595994
- Kim, D., Choo, Y.W., Kwank, K. (2015). "Comparison of lateral behavior of rock-soketed large-diameter offshore mom shafts in sand with different relative densities", *International Journal of Offshore and Polar Engineering*, Vol. 25(2), 156-160
- Kulhawy, F.H., and Mayne, P.H., 1990. *Manual on estimating soil properties*
- Leung, C.F. and Chow, Y.K. (2000). "Performance of laterally loaded socketed shafts". *Proceedings of the ISRM International Symposium, Melbourne, Australia, November 2000.*
- Liang, R., Yang, K., and Nusairat, J. (2009). "P-y criterion for rock mass". *Journal of Geotechnical and Geoenvironmental Engineering*, 135(1):26-36, DOI: 10.1061/\_ASCE\_1090-0241\_2009\_135:1\_26\_
- Liang, R., Yang, K., and Nusairat, J. (2009). "p-y criterion for rock mass." *Journal of Geotechnical*
- Little, E. G. (1982). Effects of self-heating when using a continuous bridge voltage for strain gauging epoxy models. *Strain*, 18, 131-134.
- Mander, J. B., Priestley, M. J., & Park, R. (1988). „Theoretical stress-strain model for confined concrete." *ASCE Journal of Structural Engineering*, 114(8), 1804-1826.
- Marchetti S., (1997). "The flat dilatometer: Design applications." 3rd Geotechnical Engineering Conf., Keynote lecture, Cairo Univ., Cairo, Egypt, 421–448.
- Marchetti, S. 1980. *In Situ Tests by Flat Dilatometer*. ASCE Jnl GED, Vol. 106, No. 3: 299-321.
- McClelland, B., & Focht, J. (1958). Soil Modulus for Laterally Loaded Shafts. *Transactions of the ASCE*, 123(2954), 1049-1086.
- McKenna, F., Fenves, G. L., Scott, M. H., and Jeremic, B. (2000). *OpenSees Version 2.3.2*
- Moore, L., & Barrett, J. (2010). A miniature 3d stress measurement module for in-situ stress analysis of heterogeneous system in package devices. 2010 Prognostics & System Health Management Conference. Macau.
- O'Neill, M. W., & Murchison, J. M. (1983). "An evaluation of p-y relationships in sands." A Report to American Petroleum Institute, PRAC 82-41-1. University of Houston.

- Parsons, R.L., Willems, I., Pierson, M.C., Han, J. (2010). "Lateral capacity of rock sockets in limestone under cyclic and repeated loading" Report No. K-Tran: KU-09-06
- Ramakrishna K., Karthigeyan, S., and Rajagopal, K. (2004). "Behavior of Rock Socketed Short
- Reese, L. (1997). "Analysis of laterally loaded shafts in weak rock". ASCE Journal of Geotechnical and Geoenvironmental Engineering, Vol. 123, No. 11
- Reese, L.C., "Analysis of Laterally Loaded Shafts in Weak Rock," Journal of Geotechnical and Geoenvironmental Engineering, Vol. 123, No. 11, 1997, pp. 1010–1017.
- Robertson, PK (2009). Interpretation of cone penetration tests – a unified approach, Canadian Geotech. J., 46(11):1337–1355.
- Rojas-Gonzalez, L. F., Margules, P. A., and DiGioia, A. M. Jr. (1993). "Summaries of full-scale rock-socketed foundation tests." Rep. ; RP1493-7, Electric Power Research Institute (EPRI), Palo Alto, Calif.
- Rossetto, S., Bray, A., & Levi, R. (1975). Three-dimensional strain rosettes: Pattern selection and performance evaluation. J Experimental Mechanics, 15(10), 375-381.
- Schädlich, B., & Schweiger, H. (2014a). A new constitutive model for shotcrete. In M. Hicks, R. Brinkgreve, & A. Rohe, Numerical Methods in Geotechnical Engineering (pp. 103-108). London: Taylor & Francis Group.
- Schädlich, B., & Schweiger, H. (2014b). Internal report shotcrete model: Implementation validation and application of the shotcrete model. Delft: Plaxis.
- Schütz, R., Potts, D. M., & Zdravkovic, L. (2011). Advanced constitutive modelling of shotcrete: Model formulation and calibration. Computers and Geotechnics, 38(6), 834-845.
- Seed, H. B., & Reese, L. C. (1957). The Action of Soft Clay along Friction Shafts. Transactions, ASCE, 122.
- Serdengecti, S., Hendrickson, J. A., & Skjelbreia, L. (1962). Strain-gage technique for measuring internal strains in artificial solids. J Experimental Mechanics, 2(5), 129-136.
- Slowik, V., Schlattner, E., & Klint, T. (1998). Fibre Bragg grating sensors in concrete technology. Leipzig Annual Civil Engineering Report, 109-120.
- Witasse, R. (2016). On the Use of the ShotCrete UDSM for Modelling Concrete. Delft: Plaxis bv.
- Yang, K., & Liang, R. (2006). "Numerical solution for laterally loaded shafts in a two-layer soil profile". Journal of Geotechnical and Geoenvironmental Engineering, 132(11), 1436-1443.
- Yuan, S., Zhang, K., Liu, Z., & Li, J. (2014). Numerical tests on laterally loaded drilled shafts in socketed rock. Advanced Materials Research Vols. 919-921, 706-709